

# **Structure and dynamics of thin colloidal films**

by

©Payam Bagheri

A thesis submitted to the School of Graduate Studies in partial fulfillment of the requirements for the degree of

**Master of Science**

**Department of Physics and Physical Oceanography**

Memorial University of Newfoundland

**May 2016**

St. John's

Newfoundland

# Abstract

This thesis begins by studying the thickness of evaporative spin coated colloidal crystals and demonstrates the variation of the thickness as a function of suspension concentration and spin rate. Particularly, the films are thicker with higher suspension concentration and lower spin rate. This study also provides evidence for the reproducibility of spin coating in terms of the thickness of the resulting colloidal films. These colloidal films, as well as the ones obtained from various other methods such as convective assembly and dip coating, usually possess a crystalline structure. Due to the lack of a comprehensive method for characterization of order in colloidal structures, a procedure is developed for such a characterization in terms of local and longer range translational and orientational order. Translational measures turn out to be adequate for characterizing small deviations from perfect order, while orientational measures are more informative for polycrystalline and highly disordered crystals. Finally, to obtain an understanding of the relationship between dynamics and structure, the dynamics of colloids in a quasi-2D suspension as a function of packing fraction is studied. The tools that are used are mean square displacement (MSD) and the self part of the van Hove function. The slow down of dynamics is observed as the packing fraction increases, accompanied with the emergence of 6-fold symmetry within the system. The dynamics turns out to be non-Gaussian at early times and Gaussian at later times for packing fractions below 0.6. Above this packing fraction, the dynamics

is non-Gaussian at all times. Also the diffusion coefficient is calculated from MSD and the van Hove function. It goes down as the packing fraction is increased.

# Acknowledgements

I would like to express my deepest appreciation and gratitude to my supervisors Dr. Anand Yethiraj and Dr. Kristin M. Poduska for their support, guidance, and patience. They both spent incredible amounts of time at each stage of my progress towards this thesis. Moreover, I learned valuable lessons from both of them in conducting an organized research. I am particularly grateful to them for teaching me how to work with various laboratory equipments. I would like to thank Dr. Maynard Clouter for teaching me to use the metal vapor deposition device, and letting me use it in his lab. Also I am grateful to Dr. Erika Merschrod of department of chemistry for allowing me to use the micropatterning device in her lab. As well, I thank Dr. Ivan Saika-Voivod for helpful theoretical discussions. I am also grateful to Dr. Ahmad Almudallal for helpful discussions, support and contributions to my work.

And finally I want to express my high appreciation to my wife, without whose tireless patience and constant support this achievement would have been out of reach.

# Table of Contents

<b>Abstract</b>	<b>ii</b>
<b>Acknowledgments</b>	<b>iv</b>
<b>Table of Contents</b>	<b>v</b>
<b>List of Tables</b>	<b>vi</b>
<b>List of Figures</b>	<b>vii</b>
<b>List of Abbreviations</b>	<b>viii</b>
<b>List of Symbols</b>	<b>x</b>
<b>1 Introduction</b>	<b>1</b>
1.1 Colloids and self assembly . . . . .	1
1.2 Spin coating . . . . .	3
1.2.1 What is spin coating? . . . . .	3
1.2.2 The advantages and drawbacks of spin coating . . . . .	4
1.2.3 The role of spin coating in this project . . . . .	4
1.3 Measuring the thickness of colloidal films . . . . .	5
1.4 Assessing order in colloidal crystals . . . . .	5

1.5	Dynamics of quasi-2D colloidal systems . . . . .	6
1.6	Scope of this thesis . . . . .	7
<b>2</b>	<b>Evaporative spin coated colloidal crystals</b>	<b>8</b>
2.1	Introduction . . . . .	8
2.2	Background . . . . .	9
2.2.1	Emergence of symmetries and their relevance to thickness . . .	10
2.2.2	Thickness control . . . . .	14
2.3	Experimental methods . . . . .	15
2.3.1	Making the spin coated colloidal film . . . . .	16
2.3.2	Atomic force microscopy . . . . .	17
2.4	Controlling the thickness of spin coated colloidal crystals . . . . .	21
2.4.1	Reproducibility and the effect of washing the substrates . . . .	23
2.4.2	Dependence on suspension concentration . . . . .	25
2.4.3	Dependence on the spin rate . . . . .	25
2.4.4	Effect of suspension volume . . . . .	27
2.4.5	Producing films of definite thickness . . . . .	29
2.5	Conclusion . . . . .	33
<b>3</b>	<b>Quantitative metrics for assessing positional and orientational order in colloidal crystals</b>	<b>34</b>
3.1	Introduction . . . . .	35
3.2	Methods . . . . .	37
3.2.1	Structural quantification . . . . .	37
3.2.2	Computer-generated 2D lattices . . . . .	42
3.2.3	2D images of colloidal crystals . . . . .	43
3.3	Results and Discussion . . . . .	48

3.3.1	Orientational order correlates with positional order . . . . .	48
3.3.2	Intermediate-range correlations versus local orientational order	51
3.4	Conclusion . . . . .	56
<b>4</b>	<b>Dynamics of quasi-2D colloidal suspensions</b>	<b>60</b>
4.1	Background . . . . .	60
4.2	Theory . . . . .	62
4.2.1	Diffusion and subdiffusion . . . . .	62
4.2.2	The self part of the van Hove function . . . . .	64
4.3	Experimental methods . . . . .	65
4.4	Results . . . . .	68
4.4.1	Dynamics and structure . . . . .	68
4.4.2	The van Hove function . . . . .	76
4.4.3	Gaussian vs. non-Gaussian dynamics . . . . .	79
4.5	Future work . . . . .	83
4.6	Conclusion . . . . .	84
<b>5</b>	<b>Conclusion</b>	<b>86</b>
<b>A</b>	<b>van Hove function for selected examples</b>	<b>90</b>
A.0.1	The examples . . . . .	92
A.0.2	Discussion on the initial peak of the $G_s(r, t)$ . . . . .	100
	<b>Bibliography</b>	<b>103</b>

# List of Tables

2.1	Spin coating conditions for the my experiments. . . . .	22
2.2	Conditions for producing films of definite thickness. . . . .	30
3.1	Summary of structure metrics. . . . .	37
3.2	A complete set of metrics calculated for images of colloidal crystals. .	45
4.1	List of the samples made for the dynamics study. . . . .	66

# List of Figures

2.1	Large scale structure of a spin coated colloidal crystal. . . . .	11
2.2	Laser diffraction for determining the structure of a spin coated colloidal crystal. . . . .	13
2.3	4-fold and 6-fold arrangement of spherical particles in 2D. . . . .	14
2.4	Using AFM profile to obtain the film thickness. . . . .	19
2.5	Examples of AFM micrographs of monolayer and multilayer spin coated colloidal film. . . . .	20
2.6	Reproducibility of spin coated colloidal films. . . . .	24
2.7	Film thickness vs. suspension concentration in spin coating. . . . .	26
2.8	Film thickness vs. spin rate in spin coating. . . . .	28
2.9	The effect of volume of the suspension on film thickness in spin coating.	29
2.10	Films of various thicknesses with spin coating. . . . .	31
2.11	AFM micrograph of colloidal sub-monolayer. . . . .	32
3.1	Exponential vs. power-law fit for $g(r)$ . . . . .	40
3.2	Triangulation of an imperfect 4-fold lattice . . . . .	42
3.3	Local order parameter vs. $\alpha$ . . . . .	49
3.4	Representative images of colloidal crystals produced by different methods.	52
3.5	Representative orientational correlation functions $g_s(r)$ . . . . .	54
3.6	$\langle \Psi_s \rangle$ and $\Delta_s$ vs. $f_s$ . . . . .	58

4.1	Examples of 2D colloidal samples. . . . .	69
4.2	$\log(W(t))$ vs. $\log(t)$ for the selected examples. . . . .	70
4.3	$\gamma$ vs. $\phi$ , and symmetry fractions vs. $\phi$ . . . . .	72
4.4	$\gamma$ vs. Disordered fraction. . . . .	74
4.5	$\langle \Psi_6 \rangle$ vs. $\phi$ . . . . .	76
4.6	Example of the issues in the van Hove function. . . . .	77
4.7	Summary of the van Hove function calculations. . . . .	81
4.8	Time range for non-Gaussian and Gaussian behavior. . . . .	82
4.9	Diffusion coefficient vs. $\phi$ . . . . .	83
A.1	$\gamma$ vs. $\phi$ , and symmetry fractions vs. $\phi$ . . . . .	91
A.2	$\ln(G_s(r, t))$ for example 1, and the D values obtained from it. . . . .	92
A.3	$\ln(G_s(r, t))$ for example 2, and the D values obtained from it. . . . .	93
A.4	$\ln(G_s(r, t))$ for example 3, and the D values obtained from it. . . . .	94
A.5	$\ln(G_s(r, t))$ for example 4, and the D values obtained from it. . . . .	95
A.6	$\ln(G_s(r, t))$ for example 5, and the D values obtained from it. . . . .	96
A.7	$\ln(G_s(r, t))$ for example 6, and the D values obtained from it. . . . .	97
A.8	$\ln(G_s(r, t))$ for example 7. . . . .	98
A.9	$\ln(G_s(r, t))$ for example 8. . . . .	99
A.10	A typical frame and the z-project of the movie. less than 10% of the particles are stuck. . . . .	100
A.11	(Top) $(2\pi r)G_s(r, t)$ for $t = 225.5$ s of point 1 in the appendix. (Mid- dle) The $\ln(G_s(r, t))$ . (Bottom) The area under the $(2\pi r)G_s(r, t)$ as a function of $r$ . . . . .	101
A.12	A typical frame and the z-project of the movie. less than 10% of the particles are stuck. . . . .	102

A.13 (Top)  $(2\pi r)G_s(r, t)$  for  $t = 175.5$  s of point 3 in the appendix. (Middle) The  $\ln(G_s(r, t))$ . (Bottom) The area under the  $(2\pi r)G_s(r, t)$  as a function of  $r$ . . . . . 103

# List of Abbreviations

2D	Two-dimensional
3D	Three-dimensional
AFM	Atomic force microscope (microscopy)
CCD	Charge-coupled device
CFM	Confocal fluorescent microscopy
CG	Computer generated
EG	Ethylene glycol
ETPTA	Ethoxylated trimethylolpropane triacrylate
FITC	Fluorescein isothiocyanate
IDL	Interactive data language
MEK	Methyl ethyl ketone
MPK	Methyl propyl ketone
MSD	Mean square displacement
PMMA	Poly(methyl methacrylate)
RPM	Revolutions per minute
SEM	Scanning electron microscope (microscopy)
SERS	Surface Enhanced Raman Spectroscopy
UV	Ultra-violet

# List of Symbols

$\alpha$	Lindemann parameter for positional disorder
$\gamma$	Slope of $\log(W(t))$ vs. $\log(t)$
$\Delta_s$	Approximate domain size ( $s=4$ or $6$ )
$\xi_s$	Positional correlation length within a single domain ( $s=4$ or $6$ )
$\rho_{SiO_2}$	Density of $SiO_2$ colloids
$\sigma$	Most probable inter-particle distance
$\tau$	Characteristic time in colloidal dynamics
$\phi$	Packing (area) fraction
$\Phi_s$	Suspension concentration in %
$\Psi_s$	Local bond order parameter ( $s=4$ or $6$ )
$a$	Scaling factor in the $G_s(r, t)$ fit function
$D$	Diffusion coefficient
$f_4, f_6, f_{dis}$	4-fold, 6-fold, and disordered fraction
$g(r)$	Pair correlation function
$g_s(r)$	Orientational correlation function ( $s=8$ or $6$ )
$G_s(r, t)$	The self part of the van Hove function
$m_{SiO_2}$	Mass of $SiO_2$ powder
$r_0$	Shift factor in the $G_s(r, t)$ fit function

$V_{solc}$  Volume of solvent

$W(t)$  The mean square displacement function

# Chapter 1

## Introduction

### 1.1 Colloids and self assembly

Colloid is a term that describes particles of a few nanometers to a few micrometers in size, which can be dispersed homogeneously in a continuous medium to form a dispersion. A colloidal dispersion can be composed of tiny gas bubbles in liquid (foam), liquid droplets in liquid (emulsion), solid or liquid particles in gas (aerosol), and solid particles in liquid (suspension) [1]. Examples of colloidal dispersions from everyday life are milk (emulsion of milk fat in water), blood (suspension of blood globules in blood plasma) and smoke (aerosol of solid smoke particles in air). In colloidal physics, common colloidal particles for making colloidal suspensions are silica ( $\text{SiO}_2$ ) [2,3], polystyrene [4], and PMMA (Poly(methyl methacrylate)) [5] particles. Typically, the colloidal particles in a dispersion are subject to Brownian motion [6], which means that they are in a constant random motion which is the result of constant bombardment by the molecules of the dispersion medium.

A phenomenon that is usually associated with colloidal systems is self assembly. What this means is that, in the course of their agglomeration, colloids tend to form

ordered structures, at a scale many orders of magnitude larger than the size of the colloids. Various symmetries arise, depending on the shape of the particles and the interactions between them, to minimize the free energy of the system. In other words, macroscopic order is not imposed upon the system from outside, but happens spontaneously, through the internal dynamics of the system. In fact it is possible to modify the interactions between colloidal particles in many different ways to obtain more complex structures than the ones obtainable from spherical particles with isotropic interactions [7, 8].

Colloidal crystals obtained *via* self-assembly processes have been considered as templates for producing periodic structures for different applications like photonics [9–11], quantum dot lasing [12], and sensing [13]. The advantage of self-assembly over methods like micropatterning is that it is generally cheaper and does not usually need high-tech instruments, and in some cases it can be faster [2].

A generic drawback of colloidal self assembly methods is that usually the resulting structures contain all kinds of defects, like stacking faults, dislocations and polycrystallinity. However, this is not necessarily undesirable. In fact, even amorphous colloidal structures are interesting, for example, due to their possible applications in producing uniform and “angle-independent structural color” [14] and color pigments [15]. A common definition for an amorphous structure is a structure without long range positional and orientational correlations<sup>1</sup>. But due to the general tendency of colloidal particles to self assemble and form crystalline structures, even obtaining an amorphous colloidal structure needs some control to prevent crystallization, for example, by using particles of different sizes together [14, 16].

Between the extremes of perfect colloidal crystals and amorphous colloidal struc-

---

<sup>1</sup>With regard to structural colors, if there is long range order in the arrangement of colloidal particles, Bragg planes can be defined in the structure and interference of light reflected from Bragg planes results in observation of different wavelengths in different viewing angles, so for angle independent structural color we need an amorphous structure.

tures, there are poorly crystalline and polycrystalline structures. A polycrystalline structure is one that is composed of many crystalline domains with different relative orientations. These are the kind of structures that are commonly obtained from a method like spin coating. But even these structures are not without application. For example, it has been shown [17] that a polycrystalline colloidal structure can be used as a template for producing a porous structure, which can then be used to assemble gold nano-particles in an array. This in turn can be used as a substrate for Surface Enhanced Raman Spectroscopy (SERS). A structured substrate is shown to greatly improve the SERS signal intensity.

## **1.2 Spin coating**

In all of my projects I have worked with a method called spin coating to produce colloidal films. What follows is a general description of this method, its advantages and shortcomings, and its role in this thesis.

### **1.2.1 What is spin coating?**

Spin coating is simply the use of centrifugal force to spread a fluid over a rotating substrate. This method is widely used to obtain uniform layers of polymers and colloidal films on various types of substrates [2, 4, 18, 19]. Due to the fact that this process happens on a typically fast rotating substrate (ranging from a few hundred rpm to thousands of rpm), it is a non-equilibrium process and the dynamics involved can be very complicated [20–22]. Spin coating is done by a device called a spin coater, which provides control over spin rate, the ramp-up acceleration to the desired spin rate, and spinning time.

## 1.2.2 The advantages and drawbacks of spin coating

Spin coating is a fast and robust method for producing films (and particularly, colloidal crystals) with reproducible thickness. The resulting colloidal films are crack free and free from instabilities that are observed in some other methods like vertical deposition. However, the resulting colloidal crystals in this method are very far from perfect single crystals. In fact, they are inherently polycrystalline at the macroscopic scale due to the lack of translational symmetry in their overall structure, although there exists overall orientational correlation [3]. Also as it will be shown in this thesis they are usually polycrystalline even at the microscopic scales. As well, it is shown [23, 24] that the colloidal films obtained by spin coating are thicker at the center relative to the edges.

## 1.2.3 The role of spin coating in this project

In this project spin coating is used to study film thickness, crystalline structure, as well as dynamics of quasi-2D colloidal suspensions.

First, in Chapter 2, colloidal films are produced for the purpose of studying the dependence of their thickness on spin coating conditions, namely spin rate and suspension concentration. Next, in Chapter 3, colloidal films are produced for the purpose of studying their crystalline structure. Finally, in Chapter 4, spin coating is utilized as a simple and fast method for producing wet colloidal films, with ethylene glycol as solvent, for studying the dynamics of quasi-2D colloidal suspensions as a function of particle packing fraction.

### 1.3 Measuring the thickness of colloidal films

The first part of my project was to demonstrate control over the thickness of spin coated colloidal films. This was done following the work done by others: Jiang *et al.* showed controllable use of spin coating for producing colloidal crystals with a non-volatile solvent [2]. Mihi *et. al.* produced colloidal crystals with a slowly evaporating solvent mixture [4]. And Giuliani *et al.* [23] studied the thinning rate during spin coating of a colloidal suspension with MEK (methyl ethyl ketone) as solvent, which evaporates much more quickly.

The goals of my work were to demonstrate the reproducibility of the spin coating process with highly evaporative solvents like MEK and MPK (methyl propyl ketone), and to study in more detail the thickness of the resulting film as a function of spin coating parameters. Also I was interested in finding detailed spin coating conditions for producing colloidal films of various thicknesses, with particular interest in monolayer.

### 1.4 Assessing order in colloidal crystals

During the study of the film thicknesses (Chapter 2), I obtained several atomic force micrographs of my spin coated colloidal crystals, which naturally raised the question of the quality of crystalline order in them. Therefore, it was decided to perform a quantitative characterization of the order in colloidal crystals.

What is common in the literature is a visual inspection of microscopy images [25–28]. Also, there are reciprocal space methods, such as Fourier transformation of optical images [2, 29]. Some recent studies have presented more quantitative assessments in real space [29, 30]. However a comprehensive procedure for assessing order in different respects (local, long-range, translational, and orientational) was lacking. So as the

next goal I set out to come up with such a procedure for the assessment of order of the top layer of colloidal crystals, not only made by spin coating, but made by any other methods. To this end, I studied a large number of images of colloidal crystals made by various methods, which I collected from the literature, in addition to the AFM images of my spin coated colloidal crystals. I calculated bond order parameter (from which symmetry fractions were calculated), positional disorder, pair correlation function (from which positional correlation length was calculated), and orientational correlation function (from which domain size was calculated) for more than 70 images produced by 8 techniques. This work is published [31].

## 1.5 Dynamics of quasi-2D colloidal systems

Chapters 2 and 3 deal with the study of dried colloidal films in terms of thickness and their crystalline structure. Thereafter, my focus shifted to the dynamics of colloids in a film, in order to obtain an understanding of the relationship between dynamics and structure. Spin coating was used to produce quasi-two-dimensional colloidal suspensions for this purpose.

There has been a long standing interest in the dynamics and phase transitions of 2D systems [32–35]. In my work I look at the mean square displacement (MSD) of colloids in a 2D suspension as a function of packing (area) fraction to see how dynamics changes with packing fraction. Also the self part of the van Hove function is calculated to identify the behavior as Gaussian or non-Gaussian at different packing fractions as a function of time. As well, symmetry fractions are used to correlate dynamics with structure.

## 1.6 Scope of this thesis

In this work, I started by measuring the thickness of colloidal films made by spin coating. Afterwards, analytical tools were used to quantify the structure of colloidal crystals made with various methods, including spin coating. Finally, I studied the dynamics of quasi-2D colloidal suspensions.

Chapter 2 presents the results of the analysis of the thickness of colloidal crystals made by spin coating as a function of spin rate and suspension concentration. Also conditions for producing films of definite number of layers are provided.

Chapter 3 presents the analysis of the structure of the top layer of colloidal crystals, in terms of local and long range orientational and translational order.

Chapter 4 presents the results of the study of the dynamics of quasi-2D colloidal suspension as a function of their packing fraction, and the relationship between dynamics and structure.

Chapter 5 is the conclusion chapter which presents an overview of the projects in connection with each other and their goals. The results of each project are then summarized.

# Chapter 2

## Evaporative spin coated colloidal crystals

### 2.1 Introduction

In this chapter, after a review of the highlights of the literature on spin coating of colloidal suspensions, the experimental work for producing colloidal films is presented. The objectives are to demonstrate the reproducibility of spin coating for producing colloidal films of certain thickness, and to demonstrate the control over the thickness through controlling spin coating parameters, such as suspension concentration and spin rate. Having control over the thickness of colloidal films is important for different applications. Particularly, it is useful to know how to make a monolayer, because a monolayer colloidal crystal can have special applications, e.g., as a diffraction grating or a patterning mask [36,37]. As well, in other potential applications where thicker colloidal films can be used as a 3D template (like photonic applications [9–11,38],) knowing the thickness of the film can be relevant.

What was missing in the literature was an experimental demonstration of thick-

ness reproducibility. Therefore, as my first objective, following the work of Giuliani *et al.* [23], I demonstrated reproducible control over the thickness of spin coated colloidal films produced with volatile solvents by changing spin rate and suspension concentration. Conditions for producing different thicknesses, including monolayers, are also presented.

The experimental thickness results presented in this chapter (Section 2.4) are not published anywhere other than in this thesis. Section 2.2 presents an overall view of the different aspects of spin coating for producing colloidal films and crystals, with the main focus being on spin coating dynamics and how different symmetries arise during the process and in the final dried colloidal film. The main points of this section are included in the following review article: *Soft Matter*, 9, 2013. authored by M. Pichumani, P. Bagheri, W. González-Viñas, K. M. Poduska, and A. Yethiraj. [19]. As the second author, my contribution was to write a section on the structure and symmetries of spin coated colloidal crystals, proof reading, and implementing referee's comments. In Section 2.2 reference is made to this review paper, wherever the discussion at hand can be found in it in more detail.

## 2.2 Background

Spin coating is a method that uses the centrifugal force produced by a rotating substrate to spread the suspension over the substrate [2, 19]. For spin coating of colloidal suspensions, we can use two types of solvents:

- Volatile solvents: Examples are ethanol, MEK (Methyl Ethyl Ketone), or MPK (Methyl Propyl Ketone), which evaporate very fast (in a few seconds or even less than a second) during spin coating, or a mixture like distilled water, ethanol and ethylene glycol [4], or even pure ethylene glycol, which give the experimenter

minutes before evaporating. The resulting film is dry at the end of spin coating. In this case, since the solvent has evaporated, the colloidal thin film that is obtained is a self-supporting structure of colloidal particles.

- Non-volatile solvents: These solvents do not evaporate during spin coating and the resulting thin film is not dry. An example is ETPTA (ethoxylated trimethylolpropane triacrylate) monomers [2] which need photocuring after the spin coating is done. This means that it needs to be exposed to UV light for hardening. In this case the resulting colloidal film after hardening of the polymer contains the colloidal particles and the polymer between the particles.

A remarkable feature of spin coated colloidal films is that, in spite of the very far from equilibrium dynamics of the process, the resulting structure is reproducible in terms of thickness, and contains local and global symmetries.

### **2.2.1 Emergence of symmetries and their relevance to thickness**

There have been attempts to explain the rise of local symmetries during spin coating using approximate hydrodynamical models. Shereda *et al.* [39] showed that in spite of the complexity of the hydrodynamics of spin coating, a simple model connects the rise of crystallinity to the Peclet number. In fact, Ackerson and Pusey had shown in a seminal work [40] that a steady or oscillatory flow increases the rate of crystallization in colloidal suspensions if the Peclet number exceeds a threshold value of order unity. Shereda *et al.* showed that the same threshold value for the Peclet number works in the same way in the much more complex process of spin coating (see the review paper [19] for more details on the Shereda *et al.* model).

In spin coating with volatile solvents, the process consists of an initial stage where

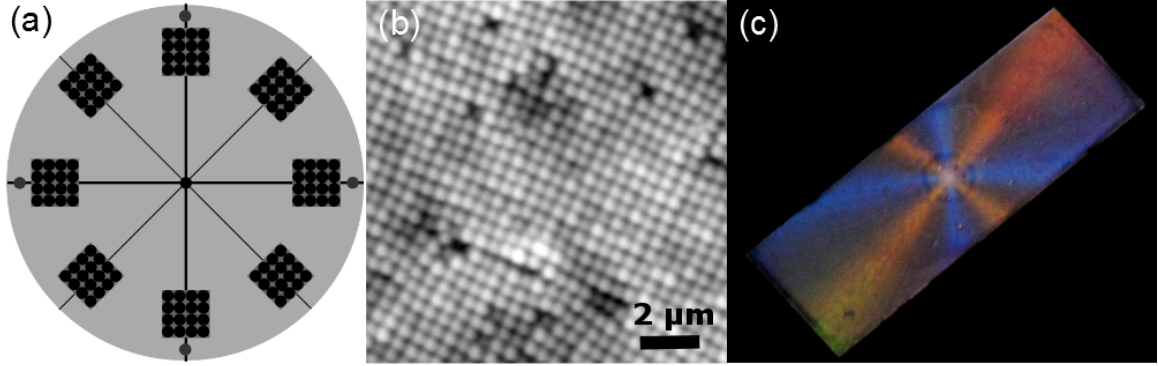


Figure 2.1: (a) Schematics of the relative orientation of local patches in a spin coated colloidal poly-crystal. (b) An atomic force micrograph of a spin coated colloidal crystal. A lighter gray means higher height. In this example each patch has a 4-fold local symmetry. (c) local 4-fold structure and their relative global orientational correlation give rise to colored arms which is an example of structural colors. This sample is  $2.5\text{ cm} \times 7.5\text{ cm}$ .

the flow of the solvent is dominant and the shear stress provided by it is the ordering factor. The second stage is when the evaporation dominates and the capillary forces between the particles re-arrange the particles to their final dry structure.

Giuliani *et al.* [23] studied the dynamics of evaporative spin coating in detail by video imaging and observed some symmetry transitions for the first time. They observed that during the first stage (when the hydrodynamics dominates) a 6-fold symmetry arises in the rotating colloidal suspension due to the shear stress provided by spinning and then there is a transition from 6-fold to 4-fold symmetry. Then, immediately before entering the evaporation dominated stage, symmetry is lost in the system and afterwards the circular drying front propagates radially towards the center and rearranges the particles into their final structure which shows either 4-fold or 6-fold symmetry (see [19] for more details on Giuliani *et al.* study).

The appearance of 4-fold or 6-fold symmetry in the final dried film depends on the rotation rate and concentration of the initial suspension [3,4,19,41], although the symmetries and their transitions are the same before the start of the evaporation and

do not depend on the rotation rate or concentration. The final structure, either 4-fold or 6-fold, is believed to have an fcc structure in three dimensions. In fact, when the top layer shows 6-fold symmetry, the (111) plane of the fcc structure is parallel to the substrate and when it shows 4-fold symmetry, the (100) plane is parallel to the substrate. Experiments show that the evaporation front starts from the periphery and moves inward and gives rise to these symmetries for the colloidal film [23], but it is not yet completely understood how these different orientations result from different spin coating parameters (see [19] for more detailed discussion about symmetries in spin coated colloidal films). The assumption of a three-dimensional fcc structure for spin coated colloidal crystals should be considered with caution, because it has been shown (*via* confocal imaging) by Vermolen [41] that the bottom layer of the spin coated colloidal film is not as ordered as the top layer. The global structure of a spin coated colloidal crystal was shown to be inherently polycrystalline [3]. This is illustrated in Fig. 2.1. Fig. 2.2 illustrates the use of laser diffraction to reveal the local symmetry and overall structure of spin coated colloidal crystals.

In spite of the possible imperfections of the supposed fcc structure for a spin coated colloidal crystal, its thickness depends on whether it is the (100) plane that is parallel to the substrate (which gives rise to the 4-fold symmetry for the top layer) or it is the (111) plane (which results in 6-fold symmetry for the top layer). Fig. 2.3 compares a 6-fold compact arrangement with a 4-fold compact arrangement for spherical particles. It is clearly seen that when the particles are in 4-fold order, there is more space between them, and therefore the next layer can interpenetrate deeper among the previous layer. Specifically, if the diameter of the colloids is  $D$ , in the 4-fold case each layer adds  $\frac{\sqrt{2}}{2}D$  to the thickness, and in the 6-fold case it adds  $\sqrt{\frac{2}{3}}D$ . So the resulting thickness of the spin coated colloidal film is affected by the symmetry of the film.

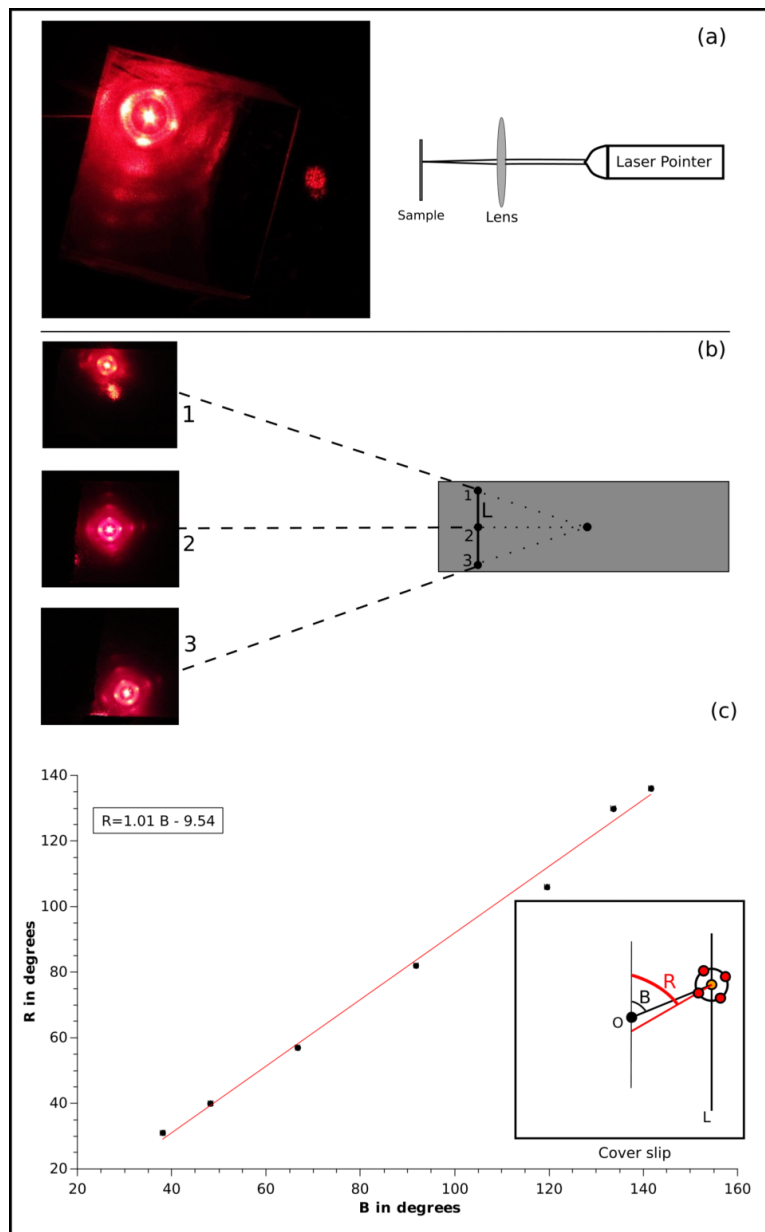


Figure 2.2: (a) Schematics of the experimental set up for laser diffraction. The diffraction pattern forms on the sample itself, and shows a 4-fold symmetry for the local structure of the colloidal film. (b) The gray rectangle is a spin coated colloidal film. By moving the laser spot along the line L, the diffraction pattern rotates. (c) We define angle B as the angle between an arbitrary line and the line connecting the center of the sample to the central laser spot, and angle R as the angle between the vertical line and the line connecting the central laser spot and one of the diffraction spots. R is a linear function of B with a slope very close to 1. This reveals the global orientational correlation of the structure of the spin coated sample.

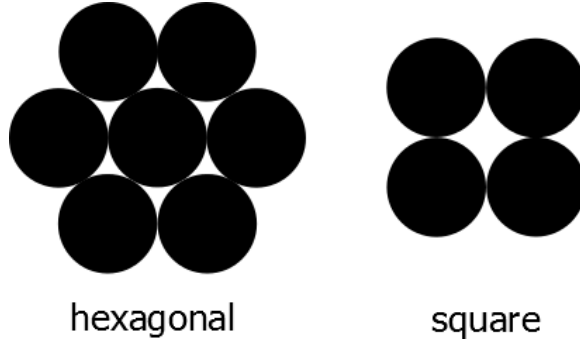


Figure 2.3: Top view of hexagonal (left) and square (right) arrangement of spheres. There is more space between the spherical particles when they are in a square arrangement. Therefore, the particles of the next layer interpenetrate deeper among the particles of the lower layer, and consequently, a square arrangement leads to a thinner film, compared to a film with the same number of hexagonally symmetric layers.

### 2.2.2 Thickness control

Theoretical and experimental work on the dynamics of spin coating and the thickness of the resulting films dates back to mid 20th century. In a seminal work, Emslie *et al.* [20] theoretically studied the thinning rate of a viscous fluid during spin coating. In a following work, Meyerhofer [21] worked out the theory of the dependence of the final thickness of a spin coated photoresist on solution concentration and spin rate by taking evaporation into account. Later on, Rehg *et al.* [22] presented the theory of spin coating of colloidal suspensions. They studied the thinning rate considering the suspension dynamics during the spinning, by also taking evaporation into account. They backed up their theory by experimental results.

Jiang *et al.* experimentally demonstrated the use of spin coating for producing colloidal crystals with a non-volatile solvent [2]. They also showed the control over thickness by controlling spin rate and time. Mihi *et al.* produced colloidal crystals

with a volatile solvent mixture [4], and also demonstrated thickness control as a function of spin rate. In their experiments the spinning time was between 2 to 15 minutes. Giuliani *et al.* [23] studied the details of the thinning rate during the spin coating of a colloidal suspension with MEK (methyl ethyl ketone) as solvent. In their experiments, the spinning time was typically up to a few seconds. They presented the specifics of the thickness profile of a spin coated colloidal film as a function of the distance from the center for films of various thicknesses made at different conditions.

Spin coating with very volatile solvents like MEK or MPK (methyl propyl ketone) is worth attention, because of the speed of the process for obtaining a colloidal crystalline layer.

## 2.3 Experimental methods

I use 22 mm×22 mm glass cover slips (Fisherbrand, catalog number 12-542B) as substrate for producing spin coated colloidal films. Also, the following washing procedure is used for cleaning the substrates. Section 2.4.1 shows that the cleanness of the substrates has a direct effect on the reproducibility of the spin coating process in terms of the thickness of the films.

First, each cover slip is rinsed with acetone and then with ethanol. In the next step, they are ultrasonicated (Branson 8510 sonicator) in a dilute NaOH solution (NaOH pellets: ACP chemicals, catalog number S-3700) with pH of 9 to 10 in plastic tubes with the caps closed, for about 30 minutes. The cover slips, as well as the insides of the tubes are rinsed with distilled water, and then each cover slip is ultrasonicated in distilled water for another 30 minutes in the tubes. Afterwards, the cover slips are taken out of the tubes and rinsed with distilled water, and then dried with nitrogen. These cover slips are glued (using Norland UV sealant 91, catalog number 9104) to

glass microscope slides (Technologist Choice, catalog number LAB-033 (7101)) to provide support. For observing the contact angle of water on the surfaces, a droplet of a few microliters is used. The droplet spreads over the surface, such that the top surface of the spread water is nearly flat. Water spreads well enough on both washed and unwashed substrates, and so they are both hydrophilic enough for doing spin coating.

### 2.3.1 Making the spin coated colloidal film

The mass of silica colloids needed for a target concentration  $\Phi_s$  is calculated as follows:

$$m_{SiO_2} = \rho_{SiO_2} \frac{\Phi_s V_{solv}}{1 - \Phi_s} \quad (2.1)$$

where  $\rho_{SiO_2}$  is the density of SiO<sub>2</sub> colloids (1.8 g/cm<sup>3</sup>),  $\Phi_s$  is their concentration in the suspension, and  $V_{solv}$  is the volume of the solvent. All suspension concentrations reported in this chapter are particle volume percentages. The silica particles used in this work are purchased from Angstromsphere (catalog number SIOP050-01). They are claimed to have a diameter standard deviation of  $\sim 5\%$ .

The monodispersity of the particles (that is, the particles being of the same size) is quite crucial here if one wants to make a colloidal crystal. In fact, it has been shown that the concentration of various kinds of defects will increase with increasing polydispersity [42].

Once its mass is measured, I heat the silica powder in the oven (at 200 °C) for three hours to dry it. This is necessary, because the surface of the silica particles absorbs water molecules, and this causes the particles to stick together. The heating temperature is low enough that the particles do not get sintered together. After heating, the glass vial is immediately capped and sealed to prevent the powder from

being exposed to the moisture in the outside air. Once the vial cools down, I add the solvent and cap it immediately. In my experiments, I used MEK (methyl ethyl ketone, Sigma Aldrich, catalog number 360473) or MPK (methyl propyl ketone, Sigma Aldrich, catalog number 87032604) as solvent.

To obtain a homogeneous suspension with colloids well dispersed (not clumped together), I ultrasonicate the suspension for at least three hours. If the size of the particles is comparable to the wavelength range of visible light, upon obtaining a monodisperse suspension, diffraction of visible light from the particles in the suspension creates iridescence, and therefore when such iridescent colors are visible near the edge of the meniscus of the suspension, it is considered ready for spin coating.

The spin coater used in this work is a Laurell Technologies spin coater (model no. WS-400B-6NPP/LITE). For spin coating, typically a volume of 30 to 40  $\mu\text{l}$  of the suspension is picked with a micropipette and is discharged in one shot on the rotating substrate. The suspension spreads on the substrate *via* rotation. With MEK or MPK, the evaporation occurs within a fraction of a second up to a seconds, for spin rates from 1000 rpm to 7000 rpm.

### **2.3.2 Atomic force microscopy**

Contact mode atomic force microscopy (AFM) is used for two different purposes in this work: film thickness measurements (*via* strip scans) and imaging of the structure of the top layer. The AFM used is an Asylum Research MFP-3D AFM, with the Asylum Research MFP-3D software which runs within WaveMetrics Igor Pro. I used gold coated n-type silicon AFM tips for imaging (MikroMasch, catalog number CSC37,  $k = 0.8 \text{ N/m}$ ). However, I observed that these tips can displace the particles on the surface of the colloidal films. This makes thickness measurements less accurate and the imaging of the arrangement of the particles close to impossible. To overcome this

problem, I found that spin coating a layer of Poly(methyl methacrylate) (PMMA) on top of the spin coated colloidal film fixes the particles in their positions. I use 50  $\mu\text{l}$  of the PMMA solution (MicroChem, 495PMMA A2; 2% in anisole) and spin coat at 5000 rpm. This produces a PMMA layer of thickness  $\sim 30$  nm when spin coated on pure glass. This thickness is negligible compared to the uncertainties in the thickness of the spin coated colloidal crystals.

- **Strip scans:** I use a metal razor to make a radial scratch from the center of the spin coated colloidal film to the edge. The scratch tears the film down to the glass substrate. It is better for the razor to be rather dull so that the resulting scratch takes a slight width on the glass surface. The height information is obtained from an AFM scan across the scratch. Such a height profile is shown in Fig. 2.4. The left side of the profile shows the glass substrate surface and the right side is the top of the colloidal film. The peak at the edge of the colloidal film is a build-up of particles, due to the act of scratching the film, so I ignore it in my thickness measurement. The average height of the glass substrate is measured as the average height between points  $a$  and  $b$  (in Fig. 2.4). The uncertainty will be the standard deviation of the mean of the data between these points. A similar height and uncertainty is obtained for the top of the colloidal films from the data points between  $c$  and  $d$ . The film thickness is the difference of these height values, and the corresponding uncertainty is the sum of the individual uncertainties. In the case of the example shown in Fig. 2.4, the height is  $1.07 \pm 0.01 \mu\text{m}$ .

For thickness measurement, I take strip scans with a width to height ratio of 4:1 at 128 points and lines. The physical size of the scanned region is  $90 \mu\text{m} \times 22.5 \mu\text{m}$  and the image size is  $1419 \times 351$  pixels, which amounts to nearly 7 pixels per particle (with a diameter of  $0.460 \mu\text{m}$ ). At this resolution, individual

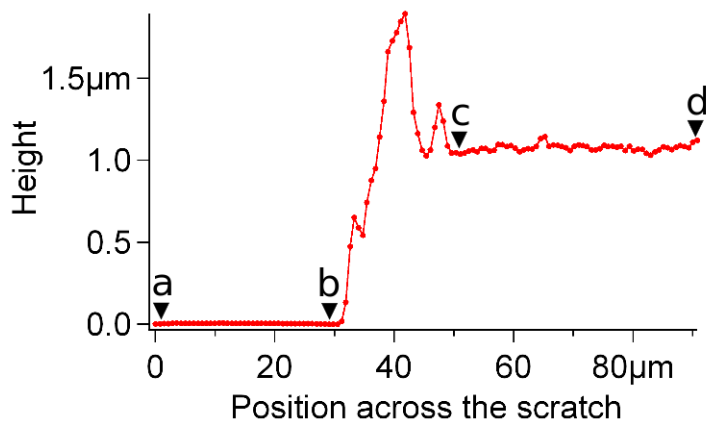


Figure 2.4: The height profile across a scratch made on a colloidal film, obtained by AFM imaging. The height of the glass side (left) is measured as the average height between *a* and *b*, and the height of the colloidal film is the average height between *c* and *d*. The thickness is equal to the difference of these heights.

particles are not resolved, but this does not affect the height measurement which is the main goal here. This choice of resolution helps the imaging to be done faster. Taking a  $90 \times 22.5 \mu\text{m}$  image takes only two or three minutes, while at a resolution where individual particles are resolved, the imaging could take over 10 minutes.

- **Square scans:** With our AFM, the largest possible scan size is  $90 \mu\text{m} \times 90 \mu\text{m}$ . I perform square scans with a width to height ratio of 1:1 at 512 points & lines. The physical size of the scanned region is  $60 \mu\text{m} \times 60 \mu\text{m}$  and the image size is  $1384 \times 1384$  pixels, which amounts to nearly 23 pixels per point and line. At this resolution each particle (with a diameter of  $0.460 \mu\text{m}$ ) is around 12 pixels in diameter, and each imaging takes around 30 minutes. Fig. 2.5 shows two examples (a monolayer and a multilayer) of square AFM images of spin coated colloidal films.

In both of the above cases (high resolution and low resolution scans) a PMMA layer was spin coated on the colloidal films to facilitate the AFM imaging.

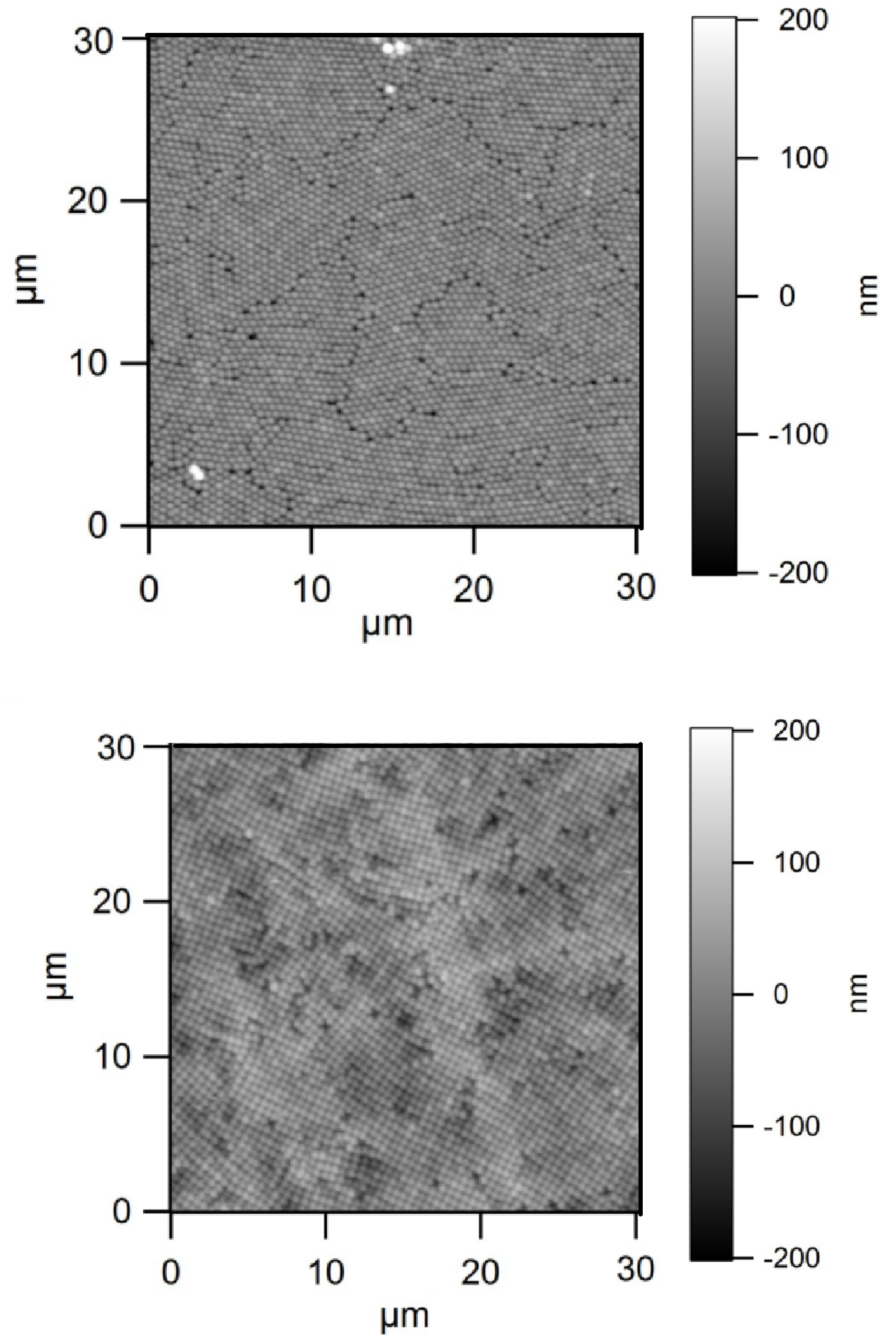


Figure 2.5: Examples of square AFM micrographs of **(top)** a monolayer (made with  $\Phi_s = 10\%$  suspension of 460 nm silica colloids in MEK at 3600 rpm), and **(bottom)** a multilayer spin coated colloidal film (made with  $\Phi_s = 20\%$  suspension of 460 nm silica colloids in MEK at 2000 rpm). The resolution is 512 point & lines. In the multilayer sample, slight thickness variations show up as variations in grayness.

## 2.4 Controlling the thickness of spin coated colloidal crystals

I investigated the relation between colloidal film thickness and the following spin coating parameters:

- Suspension concentration
- Spin rate
- Suspension volume

Table 2.1 shows a table which summarizes the spin coating conditions at which spin coated colloidal films were made. Their thickness were measured along the radial direction from the center to the edge. The results presented in the following sections are based on these measurements.

<b>Solvent: MEK</b>					
	$\Phi_s=10\%$	15%	20%	30%	40%
<b>RPM=1600</b>			2		
1800			2		
2000			16	1	
2200			2		
2400			2		
2500			2		
2750		1			
3000		3	2	1	
3200			1		
3250		1	2		
3300			1		
3500			1	1	
3600	1				
3800				1	
4000			1	2	
4500		7		1	
5000		2		1	
5500		1			
<b>Solvent: MPK</b>					
	$\Phi_s=10\%$	15%	20%	30%	40%
<b>RPM=2000</b>			5		
3000	1	1	6	1	1
4000			9		
5000			14		
6000	1	1	8	1	1
7000			9		

Table 2.1: A summary of the spin coating conditions at which samples were made. The numbers represent the number of samples made at each concentration & spin rate.

### 2.4.1 Reproducibility and the effect of washing the substrates

The parameters that one can play with in spin coating for obtaining films of different thickness are suspension concentration, spin rate and the amount of suspension used [23]. In the case of spin coating with non-volatile solvents, time is also a parameter that can be controlled [4], but with evaporative solvents, it is usually not one of the controllable parameters, as long as the same solvent is used. However, one can change the solvent itself to obtain different evaporation times.

To check the reproducibility, I made two batches of samples (6 samples in each batch) under the same conditions. One batch was made on unwashed substrate, so that I can observe the effect of washing the substrates on the reproducibility of the process.

Fig. 2.6 summarizes the results of the thickness measurements for these samples. Each point on each plot is the average thickness of the samples of the corresponding batch at a certain distance from the center. Each error bar is the standard deviation of the mean value ( $\sigma/\sqrt{n-1}$ ;  $\sigma$  is the standard deviation, and  $n$  is the number of samples). The size of the error bar relative to the absolute thickness is a measure of the reproducibility of the process. The error bars obtained here (for the samples made on washed substrates) will be used for the rest of the thickness measurement data. The uncertainty in the  $r$ -positions (along the horizontal axis) in the following thickness diagrams is roughly 0.5 mm.

In Fig. 2.6 the error bars corresponding to the samples made on unwashed substrates (red squares) are significantly larger than the error bars corresponding to the samples made on washed substrates (blue squares), while the mean values for thicknesses are nearly identical. This means that washing the substrates improves the thickness reproducibility. It also gives us general confidence in the reproducibility of the spin coated colloidal layer thicknesses.

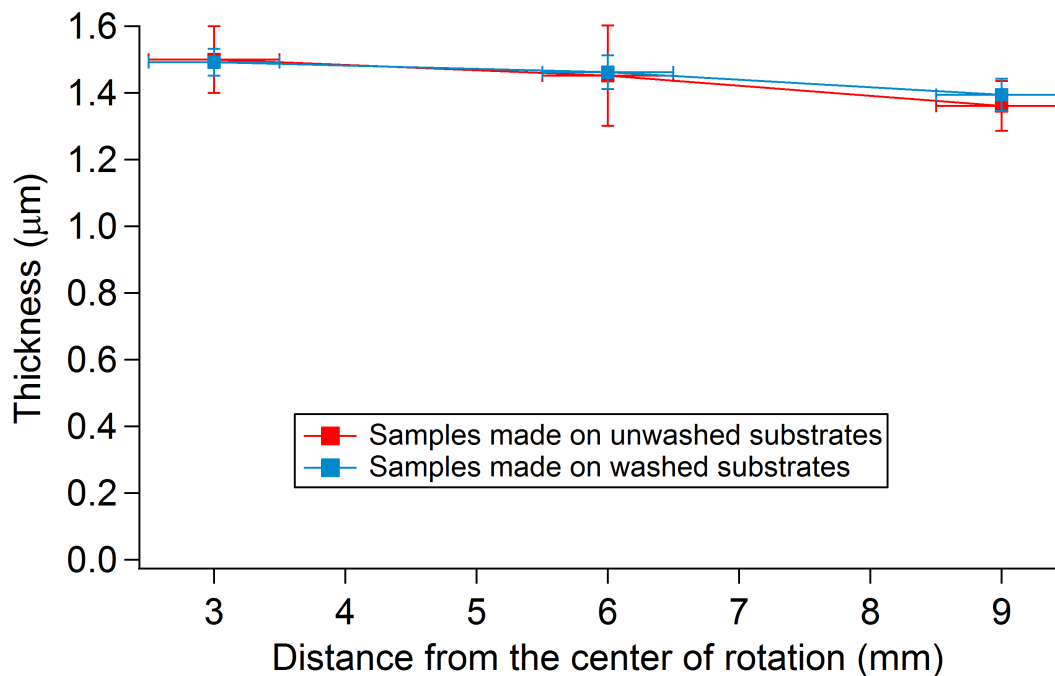


Figure 2.6: Thickness of two batches of spin coated colloidal films, made at the same conditions ( $\Phi_s = 20\%$ , spin rate=2000 rpm, with MEK as solvent), as a function of the distance from the center of the sample. One batch is made on washed substrate, and one batch on unwashed substrates. The relative size of the error bars to the absolute value of mean thickness shows that spin coating is a fairly reproducible method when the substrates are washed.

### 2.4.2 Dependence on suspension concentration

As shown in Fig. 2.7, at the same spin rate, with higher suspension concentration one obtains thicker films. This is mainly due to the fact that the viscosity of the colloidal suspension is lower at lower concentrations [43] and during the spin coating, a lower viscosity suspension tends to leave the substrate at a faster rate (due to the centrifugal force). By the time the solvent has completely evaporated, a thinner layer is left. This would be intensified by considering the fact that at a lower concentration, there is a higher volume of the solvent present in the discharged suspension, which needs more time for evaporation. Longer evaporation time generally means thinner films.

What is noticeable is that, in the case of thicker films (produced with  $\Phi_s = 30\%$  and  $\Phi_s = 40\%$ ), there is a significant difference in thickness at radii close to zero compared to larger radii, while in the case of the lower concentrations the film thickness is quite uniform. In fact, this kind of profile (thicker at the center and thinner towards the edges) is a typical feature of spin-coated colloidal films [23] that is related to the non-Newtonian nature of colloidal suspension. A Newtonian fluid becomes planar during rotation [20], but a non-Newtonian fluid will keep a non-planar shape [44] because of the lower magnitude of shear tension near the center where the centrifugal force is lower. This effect is not observed for suspensions of lower concentration ( $\Phi_s = 10\% - 20$  in Fig. 2.7) because probably the dynamics of the suspension is dominated by the properties of the solvent, which is a Newtonian fluid.

### 2.4.3 Dependence on the spin rate

Fig. 2.8 shows that for the same concentration, higher spin rates result in thinner films. As well, in the thickness profiles at 2000 rpm, 3000 rpm, and 5000 rpm the film

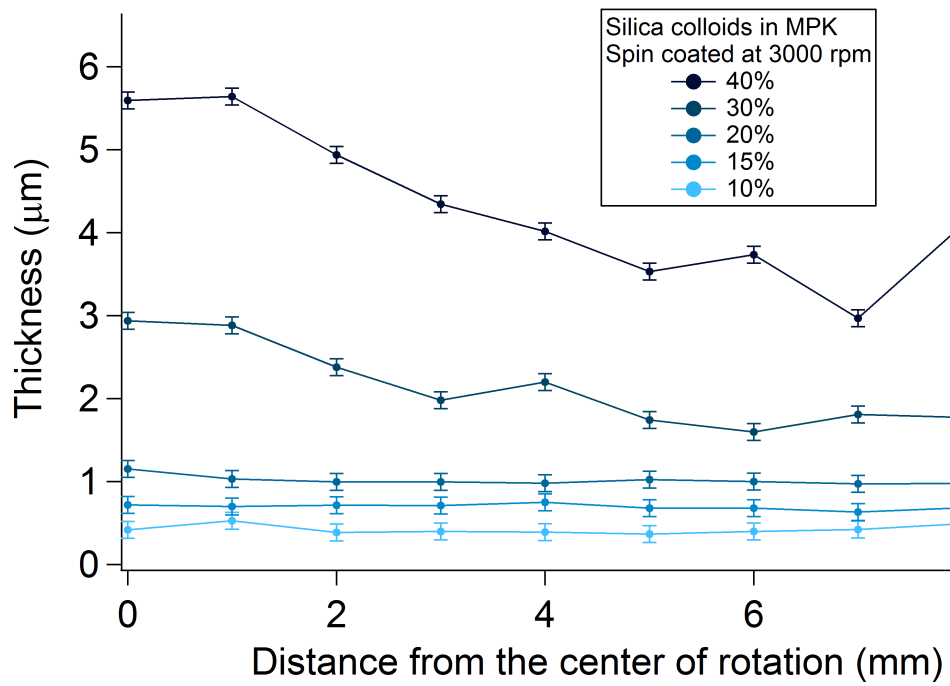


Figure 2.7: Thicker films are obtained at higher suspension concentrations. MPK (Methyl Propyl Ketone) has been used as solvent and the spin coating has been done at 3000 rpm with different concentrations  $\Phi_s = 10\%$ ,  $15\%$ ,  $20\%$ ,  $30\%$  and  $40\%$ .

generally becomes thinner further from the center of rotation.

Obtaining thinner films at higher spin rates can be explained by noting that the main factor in spreading the suspension over the substrate during the spinning is the shear stress provided by the centrifugal force. This force is greater for greater spin rates. Therefore, the radial flow rate is higher at higher spin rates. A higher flow rate results in a higher volume of the suspension to leave the substrate (before drying), and thus a thinner film.

However a noticeable feature of the thickness profiles in Fig. 2.8 is that, from 2000 rpm to 3000 rpm, there is a clear difference between the thickness profile of the films, but the difference is not so prominent for 5000 to 7000 rpm. This could be related to the fact that at these spin rates, the thickness is between that of a single-layer and a double-layer and it is hard to disrupt the film to yield a sub-monolayer film. For disrupting the film and obtaining a sub-monolayer, the centrifugal force must overcome the strong capillary force that presses the particles together during evaporation [45]. However it is still true that at 7000 rpm the thickness is less than that of 6000 and 5000 rpm.

#### **2.4.4 Effect of suspension volume**

Fig. 2.9 shows the thickness profiles of the films obtained with a relatively wide range of different suspension volumes (20  $\mu\text{l}$  to 100  $\mu\text{l}$ ) used for spin coating. What is noticeable is that thickness, especially at larger radii, is not significantly dependent on the volume. This can be explained by considering that the volume of the suspension that remain on the substrate during the spinning (before drying) is mainly determined by a balance between the centrifugal force and the adhesion of the suspension to the substrate and the excess volume will simply leave the substrate: the volume that remains on the substrate will eventually determine the thickness. However, at 3 mm

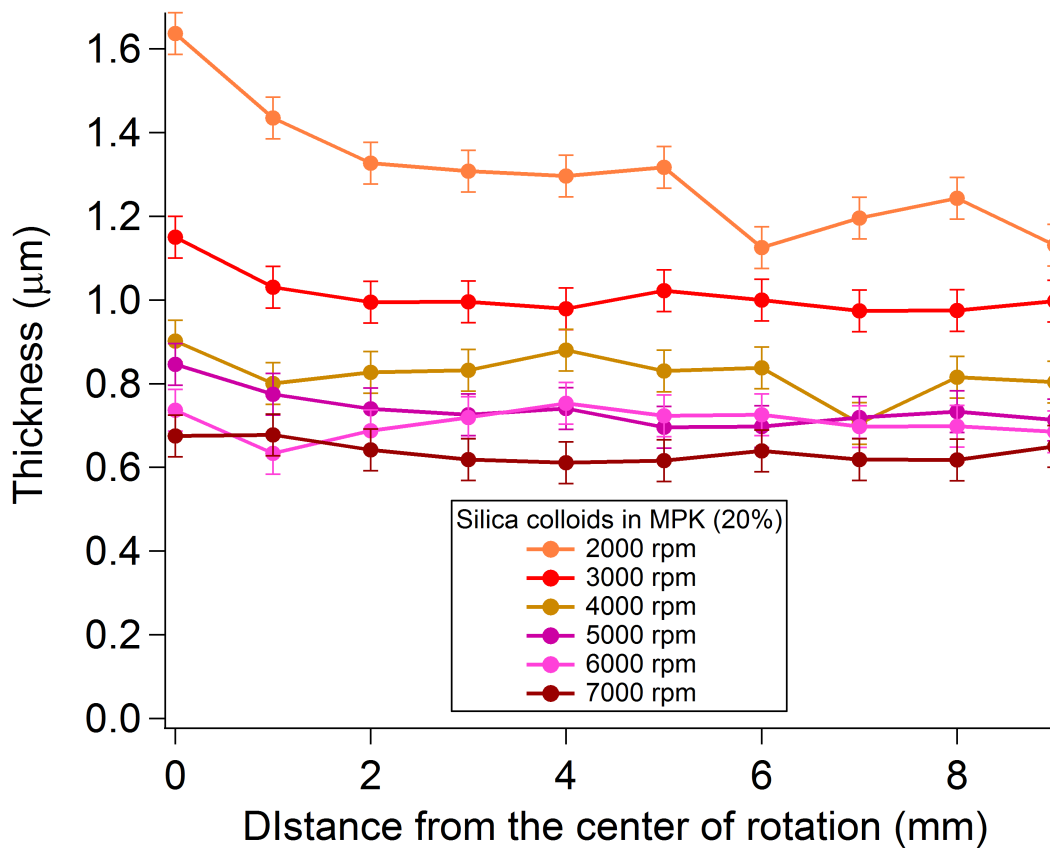


Figure 2.8: Higher spin rates yields thinner films. MPK (Methyl Propyl Ketone) used as solvent and the spin coating has been done at 2000 to 7000 rpm with  $\Phi_s = 20\%$  suspension.

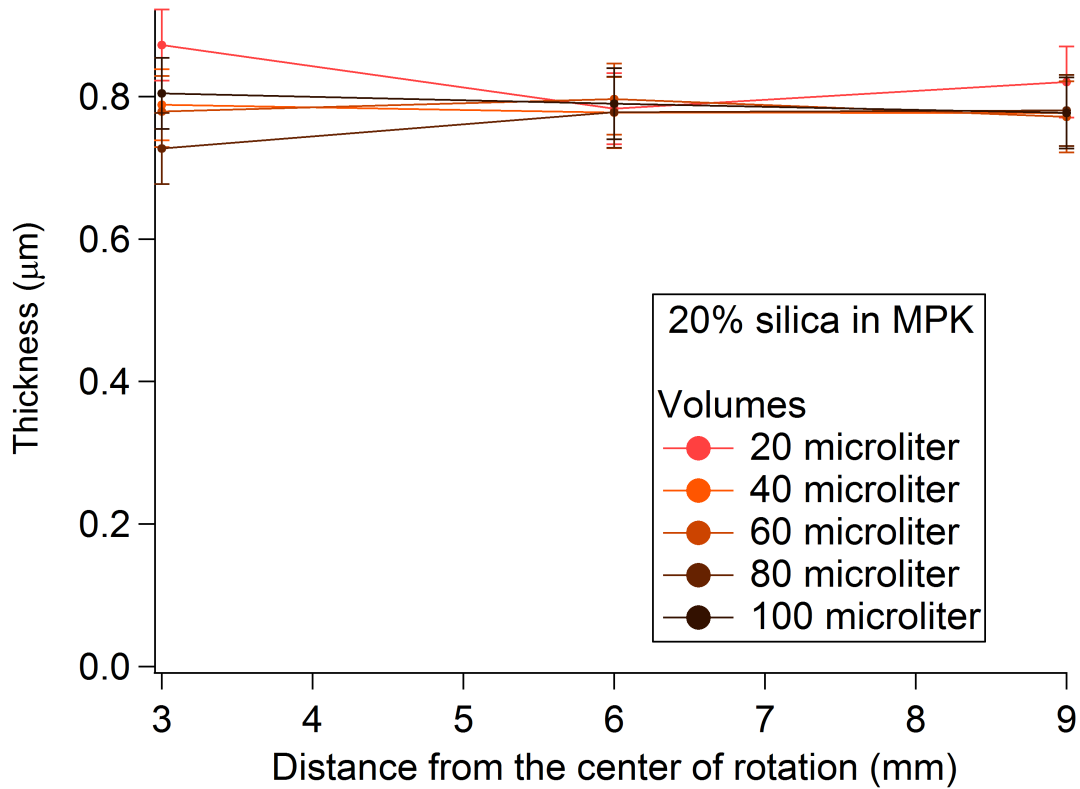


Figure 2.9: The effect of the volume of the suspension used for spin coating. Despite the wide range of volumes the change in thickness, especially in larger radii is not significant. These samples are produced at 5000 rpm with a 20% suspension.

from the center volume seems to be affecting the thickness, but the dependence on volume is not monotonic and does not show a clear trend.

### 2.4.5 Producing films of definite thickness

Having at hand a set of parameters for producing colloidal films of predefined thickness can be useful. The diagram in Fig. 2.10 summarizes the results of attempts to make films of thicknesses from a single layer up to six layers. The colloidal films produced have a thickness that is function of distance from the center of rotation, in particular for  $\Phi_s \geq 30\%$  (Fig. 2.7) or for spin rates less than 3000 rpm. Below

3000 rpm and for  $\Phi_s < 30\%$ , we are able to produce uniform films across most of the sample. Table 2.2 lists a set of parameters that led to films of each thickness: the suspension concentration, with MEK as solvent in this case, and the spin rate. For purposes of comparison, all thicknesses quoted in Table 2.2 are obtained 3 mm from the centre of rotation. Fig. 2.10 also shows the ideal thickness for 1 to 6 of layers (assuming fcc structure for the films with 4-fold symmetry for the layers) as well as the average measured thickness of the films are given. The assumption of 4-fold symmetry is based on the fact that I observed 4 iridescent arms on all of the samples reported in this plot, except for the monolayer case, which is always 6-fold symmetric. The uncertainty for the ideal thickness values in this Figure comes from the uncertainty in the diameter of the particles (which was measured to be  $0.460 \pm 0.005 \mu\text{m}$ ). The thicknesses shown in the diagram nearly agree with the ideal values at the shortest radii, though consistently a bit lower, which can be attributed to the possible non-compact arrangement of particles. Indirect evidence for the existence of non-compactness in multilayer spin coated colloidal films is the fact that there is a height non-uniformity observable in the AFM images of the top layers of such films. See Fig. 2.5(bottom) as an example.

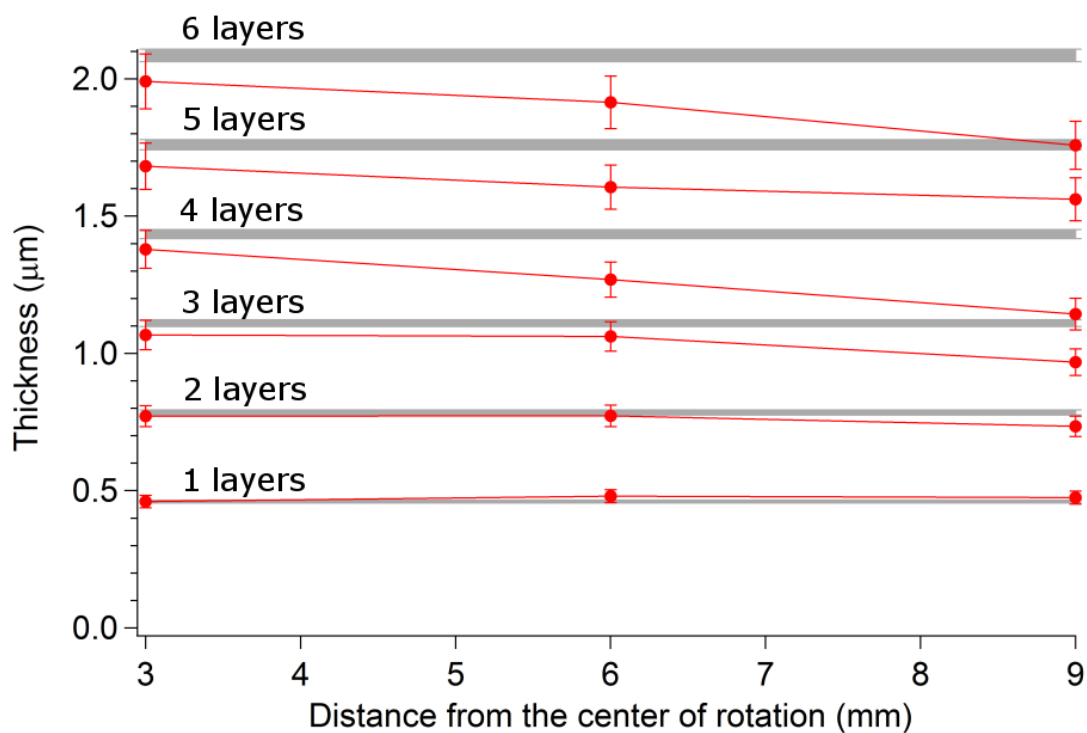


Figure 2.10: Films with thicknesses from mono-layer to six layers. The gray lines are the thicknesses for ideal fcc arrangement. The widths of these lines represent their uncertainties, coming from the uncertainty in the particle size. The red plots are the thicknesses for spin coated films with closest thickness to ideal values. The corresponding set of preparation parameters are indicated in Table 2.2.

Number of layers	$\Phi_s$	Spin rate
1	10%	3600 rpm
2	15%	4500 rpm
3	15%	3000 rpm
4	20%	3200 rpm
5	20%	2000 rpm
6	20%	1600 rpm

Table 2.2: Conditions that led to films with integer-layer thicknesses at 3 mm distance from the center of rotation. The solvent is MEK in all cases.

Another possibility is to make a sub-monolayer film. This is a non-compact single layer covering of the substrate and typically is obtained at low concentrations of the suspension ( $\Phi_s = 10\%$  or less) and high enough rotation rate. Fig. 2.11 shows an AFM image of a sub-monolayer film which was obtained with a  $\Phi_s = 5\%$  suspension at the spin rate of 3000 rpm.

## 2.5 Conclusion

In this chapter, I demonstrated control over the thickness of spin coated colloidal films produced with suspensions of  $0.460 \mu m$  silica colloids in volatile solvents of MEK and MPK. This is a faster process compared to spin coating with non-volatile solvents [2] or less volatile solvents [4]. My data shows the general reproducibility of the spin coating thickness when substrates are washed properly.

Higher suspension concentrations generally produce thicker films, with greater difference between the thickness at the center compared to the edges in the films made with higher concentration suspensions. As well, at higher spinning rates the

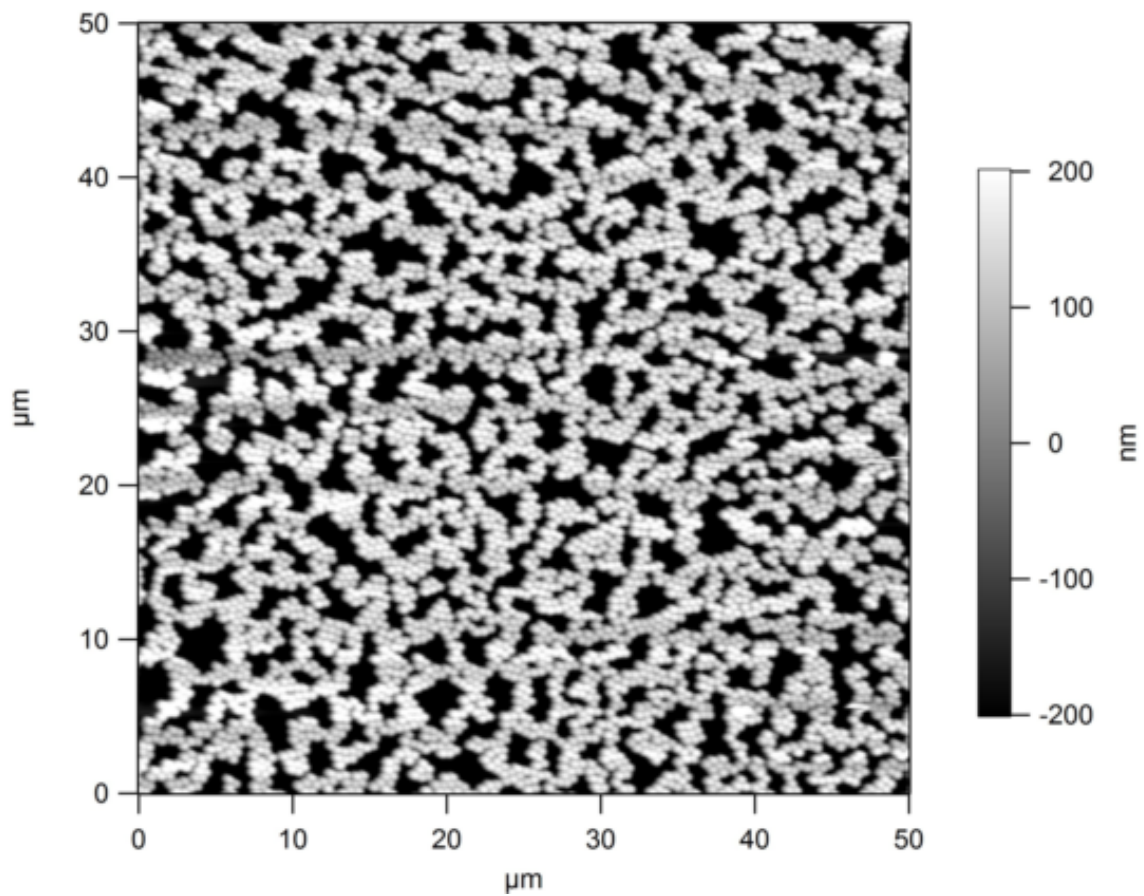


Figure 2.11: Atomic force micrograph of a colloidal submonolayer film. The black regions are the glass substrate. This sample is made with 5% suspension at 3000 rpm.

obtained film is thinner, although the differences becomes less drastic as we go to the highest spin rates. Thickness is not dependent on the volume of the suspension used for spin coating. Finally, examples of specific spin rates and suspension concentrations (with MEK as solvent) are included as future guides for producing films of thicknesses from a monolayer up to six layers.

## Chapter 3

# Quantitative metrics for assessing positional and orientational order in colloidal crystals

Reprinted (adapted) with permission from Langmuir, 2015, 31 (30), pp 8251–8259. Copyright 2015 American Chemical Society. P. Bagheri performed the analysis and the wrote the initial draft of the manuscript, and implemented subsequent revisions. A. Almudallal provided 2D simulated colloidal structures, to be compared with our data. A. Yethiraj provided comments on the drafts and contributed to the final text of the manuscript. K. M. Poduska provided comments on the drafts and contributed to the final text of the manuscript. A correction to the article has been accepted for publication. Equation 3.1 in this chapter (Equation 1 in the published paper) is affected by the correction.

# Abstract

Although there are numerous self-assembly techniques to prepare colloidal crystals, there is great variability in the methods used to characterize order and disorder in these materials. We assess different kinds of structural order from more than 70 two-dimensional microscopy images of colloidal crystals produced by many common methods including spin-coating, dip-coating, convective assembly, electrophoretic assembly, and sedimentation. Our suite of analysis methods includes measures for both positional and orientational order. The benchmarks are two-dimensional lattices that we simulated with different degrees of controlled disorder. We find that translational measures are adequate for characterizing small deviations from perfect order, while orientational measures are more informative for polycrystalline and highly disordered crystals. Our analysis presents a unified strategy for comparing structural order among different colloidal crystals, and establishes benchmarks for future studies.

## 3.1 Introduction

An important materials challenge in the last two decades has been to obtain perfect, defect-free colloidal crystals for use as photonic band-gap materials [2, 25, 46–49]. While this goal has thus far remained elusive, new applications have recently been proposed for colloidal films with lower degrees of order (such as substrates for surface-enhanced Raman spectroscopy [17]) or even amorphous structures (such as angle-independent structural color [14]). This manuscript assesses, using different measures of positional and orientational order, the crystalline quality of 2D images of colloidal crystals, thus allowing systematic comparisons, with a single toolbox, on colloidal crystals reported in the literature.

Structural comparisons of colloidal crystals have often been based on visual in-

spection of microscopy images [25–28]. Reciprocal space methods, either *via* Fourier transformation of optical images [2, 29] or *via* small-angle scattering methods, are useful in characterizing crystalline structures [50, 51]. However, spatial resolution is invaluable for studies of the kinetics of crystallization. Positional and orientational order, and correlations, are all convenient for characterizing time-independent and time-dependent processes on the same footing [3, 19, 52–54].

A few recent studies have presented more quantitative assessments in real space [29, 30]. Portal-Marco *et al.* [29] have compared colloidal structures composed of colloids with different size distributions by calculating positional and orientational correlation functions. Krejci *et al.* [30] have assessed the order in a system of nanoparticles using Voronoi tessellation, local bond-order parameter, an order parameter defined from the radial distribution function  $g(r)$ , and an anisotropy parameter which quantified orientational order. However, a detailed characterization of colloidal structures in terms of their local and overall translational and orientational order is still lacking.

In this work, we present a comprehensive comparison of structural order in colloidal crystals based on two classes of parameters: positional order and orientational order. We apply our metrics first to computer-generated structures [55, 56] to calibrate our assessments, and then to a large collection of images of colloidal crystals. This includes images from the literature for samples prepared by a wide variety of techniques [2, 4, 25–28, 38, 46–48, 57–72]. We also analyze large-area atomic force microscopy images of colloidal crystals that are new to this study.

	Local parameters
$\alpha$	Lindemann parameter for positional disorder
$\Psi_s$	local orientational bond order ( $s = 4$ or $6$ )
$\langle \Psi_s \rangle$	average local orientation bond order ( $s = 4$ or $6$ )
$f_4, f_6, f_d$	fraction of particles with 4-fold, 6-fold or disordered coordinations
$\sigma$	most probable inter-particle distance
	Long-range parameters
$\xi_s$	positional correlation length within a single domain ( $s = 4$ or $6$ )
$\Delta_s$	approx. domain size from diminishing orientational correlations ( $s = 4$ or $6$ )

Table 3.1: Summary of quantification parameters for structural order in colloidal crystals.

## 3.2 Methods

### 3.2.1 Structural quantification

The positional coordinates of the particles in each image were determined using a well established method introduced by Crocker and Grier [73]. With these particle positions, we calculate the parameters summarized in Table 3.1.

Local positional disorder is reported *via* the Lindemann parameter  $\alpha$ , defined as the standard deviation of the distribution of displacements divided by the ideal lattice spacing [74, 75]. For images from real colloidal crystals and the computer generated lattices labelled CG2, the distributions in nearest-neighbor distances were calculated over an entire image and fit with a Gaussian function to extract an effective  $\alpha$ . For computer generated lattices labelled CG1,  $\alpha$  is the input parameter used to generate a Gaussian distribution of particle displacements in these images.

Local bond orientational order, defined as

$$\Psi_s = \left| \frac{1}{N} \left[ \sum_{j=1}^N l_j e^{is\theta_j} \right] \right| / \left| \left[ \sum_{j=1}^N l_j \right] \right|, \quad (3.1)$$

is assessed in the immediate neighborhood around a single lattice point [76, 77]. Here,

$N$  is the number of the nearest neighbors at that lattice point, and  $\theta_j$  is the angle between a reference axis and the line connecting that lattice point to its  $j^{\text{th}}$  nearest neighbor. The line segment that connects the neighbors  $j - 1$  and  $j$  has the length  $l_j$ . Here we are calculating the length-weighted bond order parameter to prevent slight distortions in the lattice that result in sharp changes in  $\Psi_s$  [78].  $\Psi_s$  is calculated relative to either perfect 4-fold ( $s=4$ ) or 6-fold ( $s=6$ ) symmetry, with a value between 0 and 1, with 1 indicating perfect  $s$ -fold symmetry. We calculate  $\Psi_s$  for both  $s = 4$  and 6 for each particle and choose  $\Psi_s = 0.7$  as the minimum threshold for  $s$ -fold order. The choice of 0.7 is arbitrary but reasonable. Lower  $\Psi_s$  values are designated as disordered coordination. In very rare cases (less than 0.1%), both  $\Psi_4$  and  $\Psi_6$  are larger than the threshold value, and the order is undecidable. For easy visualization, we use color-coded images based on these assignments such that blue signifies  $\Psi_4 > 0.7$ , red indicates  $\Psi_6 > 0.7$ , and white corresponds to disordered coordination.

For each image used in this work, we report average bond orders  $\langle \Psi_s \rangle$  to quantify the average values of  $\Psi_4$  (for only particles designated as 4-fold sites) and  $\Psi_6$  (for only particles designated as 6-fold sites). Furthermore, we assess the fraction  $f_s$  ( $s = 4, 6$ , or  $d$ ) of 6-fold, 4-fold, or disordered regions, respectively, within a single image.

Next, going beyond nearest neighbor order, we assessed the positional correlations across an entire image through the radial distribution function

$$g(r) = \frac{1}{N} \left( \sum \frac{dn}{dA} \right) / \left( \frac{N}{A} \right). \quad (3.2)$$

Here,  $dn$  is the number of lattice points in a ring of inner radius  $r$  and area  $dA$ ,  $N$  is the total number of particles in the image, and  $A$  is the total area of the image. We use the position,  $r = \sigma$ , of the first maximum in  $g(r)$  as a measure of the most probable inter-particle spacing for a given image. By fitting this  $g(r)$  with a complicated function,

we extract a characteristic positional correlation length  $\xi_s$  that we report relative to the most probable inter-particle spacing  $\sigma$ .

It is well known in the literature of 2D phase transitions that an exponential decay in a radial distribution function  $g(r)$  indicates short range-order (such as for liquids), while a power law decay is consistent with quasi-long range order (such as for 2D solids) [52, 79–82]. An earlier report showed that the  $g(r)$  for a two-dimensional solid can be fitted to distinguish between exponential and power law behaviors [83]:

$$g_{\text{fit}}(r) = \left[ \frac{A}{(2\pi)^{(3/2)}} \frac{1}{\tilde{\sigma}} \sum_{i=1}^n \frac{g_{\text{id}}(x_i)}{D x_i} \exp\left(\frac{-(r - D x_i)^2}{2\tilde{\sigma}^2}\right) - 1 \right] \times L(r) + 1. \quad (3.3)$$

Here,  $L(r)$  can be either  $\exp(-r/\xi)$  for an exponential fit or  $r^{-k}$  for a power-law fit. We applied this fit to the radial distribution functions for all 69 colloidal crystal images listed in Table 3.2. An example is shown in Figure 3.1, and the details of our method follow below.

To use Equation 3.3, we constrained several parameters during fitting. The peak widths are set by  $\tilde{\sigma} = \sigma_0 \sqrt{\ln(r/r_0)}$ , where  $r_0 = 0.3D$  and  $\sigma_0$  was limited to values between 0.03 and 0.08.  $D$  is the normalized lattice spacing, which we constrained between 0.8 and 1.1. The remaining parameters were unconstrained in our fits.  $A$  is a scaling factor to adjust peak heights.  $\xi$  is the positional correlation length (for the exponential fits), and  $k$  is the exponent (for the power law fits).

The most computationally intensive part of the fit is the  $g_{\text{id}}(x_i)$  term, which gives the number of particles at a distance  $x_i$  from a point in a perfect lattice (either 6-fold or 4-fold, as appropriate). We used up to 400 terms in the summation in the fit function over a range from  $0 \leq r \leq r_{\text{max}}$ . The quality of the overall fit – especially in the first few  $g(r)$  peaks – is influenced by the value of  $r_{\text{max}}$ . For this reason, we

investigated a statistical  $\chi^2$  test, using the sum of squared errors between the true  $g(r)$  and  $g_{fit}(r)$ , as a function of the fitting range separately for each image. In general, the statistical  $\chi^2$  value grows as  $r_{max}$  increases, until it reaches a plateau. Because of this, we chose the optimal  $r_{max}$  to be where the statistical  $\chi^2$  plateaus. Beyond this range, the tail of the  $g(r)$  function overwhelms the fit at the expense of the first peaks.

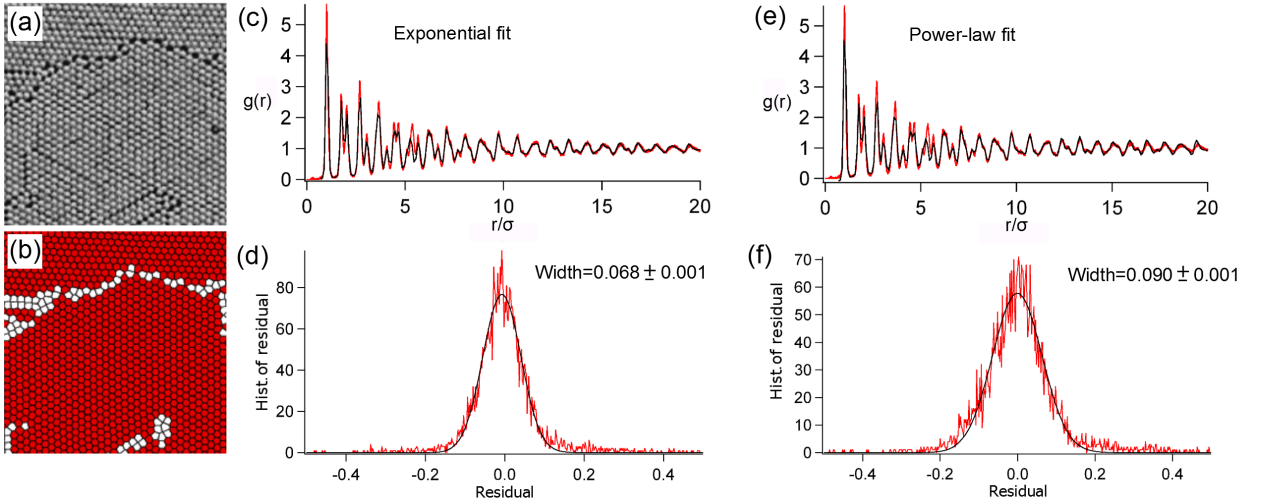


Figure 3.1: (a) A cropped SEM micrograph of a colloidal monolayer [84] and (b) its local coordination color map (red = 6-fold coordination, white = disordered coordination). The  $g(r)$  is compared with both an exponential  $g_{fit}$  (c) and power law  $g_{fit}$  (e) using histograms of the residuals for each fit (d, f). After fitting the histograms with a Gaussian form, the narrower width of the exponential fit leads us to favor it over the power-law fit.

We applied the fit in Equation 3.3 to all images listed in Table 3.2. This included images of true 2D colloidal monolayers, as well as images that showed the top of multi-layer structures (either quasi-2D or 3D). It was surprising that an exponential

fit works well for all images. Figure 3.1 compares an exponential and a power-law fit to the  $g(r)$  for a representative image of a colloidal monolayer. In this case, we favor the exponential fit over the power-law fit because of the narrower residual width. Thus, it is noteworthy that we see (liquid-like) exponential  $g(r)$  decay trends even for structures that are ostensibly crystalline.

Finally, we also assessed orientational correlations among different domains within a single image. The orientational correlation function [83],

$$g_s(r) = \left| \frac{1}{N_B} \sum_{l=1}^{N_B} \frac{1}{n_l} \sum_{k=1}^{n_l} e^{is(\theta(r_k) - \theta(r_l))} \right|, \quad (3.4)$$

is defined in terms of bonds  $l$  between particles, and the angular orientations of these bonds relative to either 4-fold symmetry ( $s = 8$ ) or 6-fold symmetry ( $s = 6$ ). In order to identify the bonds within a lattice, Delaunay triangulation is performed [85]. This process consists of connecting each lattice point to its neighbors to form triangles such that no circumcircle of any triangle contains any lattice point. The circumcircle of a triangle is the circle that contains the triangle, with its corners being on the circle. In the process of triangulation to identify bonds in a 4-fold structure (see Figure 3.2), we can sometimes encounter diagonal bonds. This can be accounted for by using  $s = 8$  for 4-fold symmetric order parameters, as was first suggested by Weiss and Grier. [86] For the remaining parameters in Equation 3.4,  $\theta(r_k)$  and  $\theta(r_l)$  are the angles between the bonds at  $r_k$  and  $r_l$ , each with respect to the same reference axis.  $n_l$  is the number of bonds at the distance  $r$  from the mid-point of the bond  $l$ , and  $N_B$  is the total number of bonds in the 2D colloidal structure. By assessing the orientational correlation function over an entire image, we use the first value of  $r$  at which the correlations disappear ( $g_s(r) \rightarrow 0$ ) to indicate a representative size for a single domain; we denote this value as  $\Delta_s$ , and give its value relative to the most

probable inter-particle spacing  $\sigma$ .

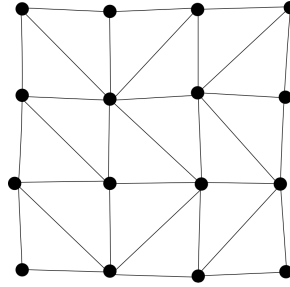


Figure 3.2: An example of the Delaunay triangulation of an imperfect 4-fold lattice.

### 3.2.2 Computer-generated 2D lattices

We used four different sets of 2D computer-generated lattices to compare with images of laboratory-produced colloidal structures. The first set of computer-generated (CG1) lattices has a predetermined degree of disorder, introduced by displacing each lattice point in a 2-dimensional crystal (with 4-fold or 6-fold symmetry) independently, such that there is a Gaussian distribution of displacements relative to their positions in the unperturbed crystal lattice.

The second set of computer-generated lattices (CG2) has disorder introduced in a more physically meaningful way, by mimicking the effect of volume exclusion that occurs with non-zero particle sizes. We used 4-fold symmetric configurations obtained from Monte Carlo simulations of a 2D system of particles subject to a square-shoulder square-well potential [55], calculated at different temperatures to generate different levels of disorder.

The third set of generated lattices (CG3) addresses the limiting case when there is no long-range positional or orientational order. These computer-generated random structures were obtained based on earlier published work. [56]

Finally, multi-domain crystals (CG4) were simulated by manually rotating a small

number of perfectly ordered lattices (CG1 with no positional displacements) to create mosaics with arbitrarily rotated domains.

### 3.2.3 2D images of colloidal crystals

We collected 40 scanning electron microscopy (SEM) and confocal fluorescence microscopy (CFM) images from the literature to span a wide range of common colloidal crystal assembly techniques: convective assembly [26–28, 38, 46, 47, 57–61], electrophoretic assembly [62–64], electrospraying [65], air-liquid interface assembly [25, 66, 67], confinement [48, 68], dip coating [69, 70], spin coating, [2, 4, 71] and sedimentation [72].

Additionally, 29 new atomic force microscopy (AFM) images were obtained from spin-coated colloidal crystals made by spin coating (2000-7000 rpm) a suspension of 0.46  $\mu\text{m}$  spherical silica particles (10–40 vol%), in methyl ethyl ketone (MEK) or methyl propyl ketone (MPK), on glass substrates as described in earlier work by some of the same authors [53]. Prior to AFM imaging (with Asylum Research MFP-3D in contact mode, with Au-coated Si cantilevers (Mikromasch CSC37/Cr-Au/50,  $k \sim 0.50$  N/m)), the spin coated colloidal crystals were coated with a thin ( $\sim 50$  nm) spin coated layer of polymethylmethacrylate (PMMA) to prevent displacement of the colloidal particles while scanning.

A comprehensive summary of the images, their sources, and our calculated parameters is given in Table 3.2. Images from the literature are named according to the paper from which they came: the last name of the first author, its publication year, the reference citation, and its figure number. In cases where images were obtained through private communication, “pc” replaces a figure number. Our own images (new to this study) use a different naming convention. For example, “10MEK40 $\mu$ 3600” signifies 10 volume percent suspension of 0.460 micron spherical silica particles in

Methyl Ethyl Ketone, using 40  $\mu\text{l}$  during spin coating at 3000 rpm. A dagger ( $\dagger$ ) after an image name indicates that the colloidal crystal is monolayer; all other samples are multilayers. This is important to note because earlier studies have demonstrated that a high degree of order in a surface layer does not guarantee a high degree of order deeper inside a colloidal crystal. [87, 88] The full size of each image is listed as  $x \times y$  in units of  $\sigma$ .

Each image has an effective Lindemann parameter  $\alpha$ . The remaining order parameter values (local orientational bond order  $\langle \Psi_s \rangle$ , symmetry fraction  $f_s$ , representative domain size  $\Delta_s$ , and positional correlation length  $\xi_s$ ) were calculated for  $s=4$ -fold and  $s=6$ -fold regions separately in each image whenever possible. Where symmetry fractions or domain sizes were too small to calculate meaningful values, table entries show “–” or “ $\times$ ”. Single-domain images are indicated with  $\Delta_s = \text{S}$ . Uncertainty magnitudes are as follows:  $\delta\alpha$  is 2 in the last decimal digit;  $\delta\Psi_s = 0.04$ ;  $\delta f_s/f_s = 0.1$  for  $f_s$  above 0.2, and  $0.1 < \delta f_s/f_s < 0.3$  for  $f_s$  below 0.2.  $\delta\Delta_s/\Delta_s = 0.05$ .  $\delta\xi_s/\xi_s = 0.05$ .

For some of the SEM and AFM images,  $g(r)$  fits were poor until we modified the aspect ratio to compensate for image distortion (drift). The  $\xi_s$  values extracted from rescaled images are noted with an asterisk (\*) in the table, based on these horizontal scaling factors: Wang(2011)pc1=0.94, Wang(2011)pc2=0.93, Wang(2011)pc3 = 0.93, Wang(2011)pc4=0.94, Wang(2011)pc5=0.92, Jiang(2004)5a=0.90, Li(2005)1b=0.88, Li(2005)1d=0.80. There were four cases for which linear rescaling was not sufficient, and these have no positional correlation length value listed.

Image source	$x \times y$	$\alpha$	$\langle \Psi_4 \rangle$	$f_4$	$\Delta_4$	$\xi_4$	$\langle \Psi_6 \rangle$	$f_6$	$\Delta_6$	$\xi_6$
<b>Convective</b>										
Wong(2003) [47], 3a	$94 \times 70$	0.038	–	–	–	–	0.96	1	S	*
Wong(2003) [47], 3c	$67 \times 49$	0.027	–	–	–	–	0.95	1	S	*
Cong(2003) [57], 4c	$29 \times 24$	0.050	0.89	0.39	S	12	0.92	0.47	S	5
Gu(2002) [59], 8	$20 \times 20$	0.020	–	–	–	–	0.98	1	S	14
Gu(2002) [59], 8	$20 \times 20$	0.025	–	–	–	–	0.99	1	S	28
Teh(2005) [60], 4a	$29 \times 22$	0.046	–	–	–	–	0.92	0.85	S	17
Kuai(2004) [27], 4b	$76 \times 62$	0.027	–	–	–	–	0.98	1	S	6
Kuai(2004) [27], 4c	$76 \times 62$	0.033	–	–	–	–	0.96	1	S	7
Kuai(2004) [27], 4d	$76 \times 62$	0.036	–	–	–	–	0.96	0.94	S	5
Kim(2005) [61], 1a†	$98 \times 60$	0.0634	–	–	–	–	0.87	0.52	S	2
Kim(2005) [61], 1c†	$98 \times 65$	0.055	–	–	–	–	0.90	0.80	S	9
Kim(2005) [61], 1d†	$98 \times 65$	0.027	–	–	–	–	0.96	0.97	S	6
Ye(2001) [38], 1b	$31 \times 27$	0.028	–	–	–	–	0.97	1	S	14
<b>Electrophoretic</b>										
Zhou(2013) [62], 6c	$81 \times 56$	0.028	0.91	0.20	S	7	0.96	0.71	S	5
Zhou(2013) [62], 6d	$36 \times 62$	0.019	–	–	–	–	0.98	1	S	10
Choi(2013) [64], 3b†	$18 \times 18$	0.020	–	–	–	–	0.98	1	S	16
<b>Electrospray</b>										
Coll(2013) [65], pc1	$47 \times 35$	0.021	–	–	–	–	0.95	0.79	19	8
Coll(2013) [65], pc2	$170 \times 83$	0.040	–	–	–	–	0.90	0.53	25	3
Coll(2013) [65], pc3	$55 \times 45$	0.026	–	–	–	–	0.98	0.97	S	7
Coll(2013) [65], pc4	$35 \times 29$	0.027	–	–	–	–	0.97	1	S	29
<b>Air-liquid</b>										
Wang(2011) [25], pc1	$19 \times 13$	0.038	–	–	–	–	0.98	1	S	12*
Wang(2011) [25], pc2	$24 \times 18$	0.034	–	–	–	–	0.97	1	S	8*
Wang(2011) [25], pc3	$21 \times 18$	0.030	–	–	–	–	0.98	1	S	21*
Wang(2011) [25], pc4	$21 \times 15$	0.043	–	–	–	–	0.97	1	S	34*
Wang(2011) [25], pc5	$24 \times 17$	0.026	–	–	–	–	0.98	1	S	6*
<b>Confining cell</b>										
Park(1998) [48], 2a	$77 \times 64$	0.023	–	–	–	–	0.97	0.96	S	12
Wang(2009) [68], 2b	$58 \times 61$	0.045	–	–	–	–	0.92	0.87	S	4
Wang(2009) [68], 2h	$52 \times 32$	0.040	–	–	–	–	0.91	0.86	S	3

Table 3.2: A complete set of parameters calculated for images used in this study. This includes: image size ( $x \times y$ ), effective Lindemann parameter ( $\alpha$ ), average local orientational bond order ( $\langle \Psi_s \rangle$ ), symmetry fraction ( $f_s$ ), representative domain size ( $\Delta_4$ ), and positional correlation length ( $\xi_s$ ). A dagger (†) denotes monolayer crystals.

<b>Image source</b>	$x \times y$	$\alpha$	$\langle \Psi_4 \rangle$	$f_4$	$\Delta_4$	$\xi_4$	$\langle \Psi_6 \rangle$	$f_6$	$\Delta_6$	$\xi_6$
<b>Dip coating</b>										
Nagao(2008) [69], 2a†	22 × 24	0.024	–	–	–	–	0.97	1	S	7
Fu(2008) [70], pc	23 × 19	0.051	–	–	–	–	0.93	1	S	*
<b>Spin coating</b>										
Mihi(2006) [4], pc1	39 × 29	0.053	0.90	0.57	32	3	0.86	0.09	3.0	×
Mihi(2006) [4], pc2	39 × 29	0.054	0.89	0.52	S	3	0.85	0.09	3.0	×
Mihi(2006) [4], pc3	39 × 29	0.048	0.87	0.35	17	5	0.90	0.30	16	3
Mihi(2006) [4], pc4	37 × 27	0.059	–	–	–	–	0.90	0.85	S	6
Jiang(2006) [71], 2b†	29 × 24	0.048	–	–	–	–	0.92	0.94	S	4
Jiang(2004) [2], 5a	87 × 55	0.039	–	–	–	–	0.94	0.93	S	13*
Cheng(2014) [84], 5b†	145 × 106	0.030	–	–	–	–	0.96	0.93	33	16
10E40μ3600 †	115 × 115	0.026	–	–	–	–	0.92	0.79	18	4
10E50μ4000 †	115 × 115	0.040	–	–	–	–	0.90	0.79	15	5
10E50μ4000 †	115 × 115	0.037	–	–	–	–	0.90	0.65	12	3
10E50μ4500 †	115 × 115	0.049	–	–	–	–	0.89	0.70	18	5
10E50μ4750 †	115 × 115	0.039	–	–	–	–	0.86	0.54	17	3
15E40μ2750	115 × 115	0.081	0.82	0.06	5.0	–	0.85	0.52	18	5
15E40μ2750	115 × 115	0.045	0.86	0.29	8.0	4	0.86	0.26	16	4
15E40μ3000	115 × 115	0.046	0.87	0.47	14	5	0.84	0.12	7.0	4
15E40μ3250	115 × 115	0.055	0.88	0.60	16	6	–	–	–	–
15E40μ4500	115 × 115	0.038	0.87	0.25	8.0	4	0.87	0.35	20	3
15E40μ5000	115 × 115	0.040	0.89	0.60	15	4	–	–	–	–
15E40μ5500	115 × 115	0.038	0.90	0.60	15	4	0.82	0.05	×	×
20E40μ2000	115 × 115	0.051	0.88	0.69	S	6	–	–	–	–
20E40μ2000	115 × 115	0.034	0.89	0.65	S	6	–	–	–	–
20E40μ2000	115 × 115	0.037	0.90	0.73	S	7	–	–	–	–
20E40μ2000	115 × 115	0.034	0.89	0.76	S	7	–	–	–	–
20E40μ3000	115 × 115	0.047	0.89	0.78	S	9	–	–	–	–
15P40μ3000	90 × 90	0.072	0.86	0.35	11	4	0.84	0.16	15	5
15P40μ5000	115 × 115	0.082	0.87	0.66	11	6	–	–	–	–
15P40μ5000	115 × 115	0.085	0.86	0.45	10	4	–	–	–	–
20P100μ2000	115 × 115	0.054	0.84	0.08	5.0	3	0.87	0.50	20	5
20P100μ5000	115 × 115	0.047	–	–	–	–	0.88	0.65	23	5
20P100μ5000	115 × 115	0.058	0.88	0.66	17	5	–	–	–	–
20P100μ5000	115 × 115	0.068	0.87	0.65	19	5	–	–	–	–
20P10μ7000	115 × 115	0.054	0.84	0.17	9.0	3	0.83	0.26	18	3
20P20μ5000	90 × 90	0.064	0.89	0.46	S	5	0.88	0.21	15	4
30P40μ3000	90 × 90	0.057	0.88	0.66	S	5	–	–	–	–
40P40μ3000	90 × 90	0.054	0.86	0.40	19	3	0.84	0.14	5.0	2
40P40μ3000	90 × 90	0.058	0.87	0.59	S	4	0.82	0.06	3.0	×

<b>Image source</b>	$x \times y$	$\alpha$	$\langle \Psi_4 \rangle$	$f_4$	$\Delta_4$	$\xi_4$	$\langle \Psi_6 \rangle$	$f_6$	$\Delta_6$	$\xi_6$
<b>Sedimentation</b>										
Li(2005) [72], 1a	$32 \times 27$	0.035	–	–	–	–	0.88	0.92	S	*
Li(2005) [72], 1b	$32 \times 27$	0.039	–	–	–	–	0.91	0.98	S	9*
Li(2005) [72], 1d	$32 \times 27$	0.027	–	–	–	–	0.89	0.96	S	11*
<b>Random (CG3)</b>										
Ferry(2011) [56], pc1	$22 \times 22$	0.31	0.82	0.09	1.5	×	0.80	0.11	2.0	×
Ferry(2011) [56], pc2	$27 \times 27$	0.28	0.81	0.07	2.0	×	0.79	0.13	3.5	×
Ferry(2011) [56], pc3	$30 \times 30$	0.23	0.82	0.07	2.0	×	0.80	0.13	1.5	×

### 3.3 Results and Discussion

We begin by examining order as obtained through local measures that depend only on the immediate (nearest-neighbour) environment. We then compare this with parameters for order related to longer-range correlations. Finally, we apply both local and longer-range characterizations to images with multiple domains.

#### 3.3.1 Orientational order correlates with positional order

We calibrated differences in local order for images of real colloidal crystals by comparing with data from computer-generated lattices (CG1, CG2, and CG3) with controlled levels of positional disorder. The first step was to assign each particle a coordination environment based on its local orientational order parameter  $\Psi_s$ .

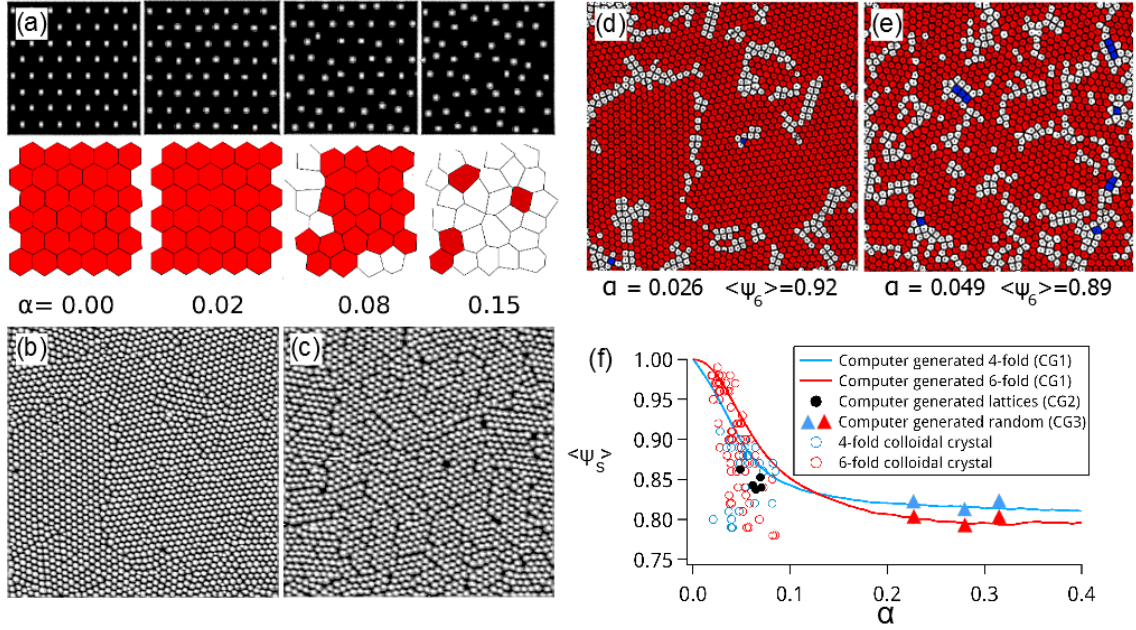


Figure 3.3: (a) Representative computer-generated lattices (CG1) and (b-e) AFM images of spin coated colloidal monolayers. Red indicates 6-fold coordination, blue 4-fold, and white disordered coordination. Effective  $\alpha$  values are noted below each color-coded image. (f) correlates the average local bond order  $\langle \Psi_s \rangle$  with values of  $\alpha$ . Trend lines for computer generated lattices (CG1), including those shown in (e), are shown as solid curves ( $s = 4(6)$  in blue (red)). Additional computer-generated images (CG2, CG3) are shown as solid black circles and solid triangles. The remaining data points, shown with open circles, are from images of real colloidal crystals.

Figure 3.3a-e shows representative examples for both computer-generated (CG1) and colloidal crystal lattices using color codes of blue for 4-fold, red for 6-fold, and white for disordered coordinations. In computer-generated random lattices (CG3), most lattice points show disordered coordination, as expected. However, in real samples, the disordered coordinations tend to coincide with point defects and domain boundaries.

Our comparisons between real and computer generated lattices show a useful correlation between average local orientational order and average local positional order. For each image, we calculated  $\langle \Psi_6 \rangle$  and  $\langle \Psi_4 \rangle$  for each symmetry separately. The measured  $\alpha$  value and  $\langle \Psi_s \rangle$  for each image are plotted in Figure 3.3f. Data for computer-generated lattices with a simple Gaussian distribution of displacements (CG1, solid curves) serve as an upper bound for  $\langle \Psi_s \rangle$  at a given  $\alpha$  value. This is true for both  $s = 4$  (blue) and  $s = 6$  (red). For images from real colloidal crystals,  $\alpha$  falls in a narrow range above 0.03 but below 0.10, consistent with the Lindemann melting criterion [74]. On the other hand, highly disordered computer-generated structures (CG3) have liquid-like values ( $\alpha \geq 0.2$ ). We note that all of the images used in this study can be considered crystalline, since they do not exhibit orientational order features (small dislocations) that are indicative of hexatic phases. [55]

We refer to all the order parameter measures discussed here as “local” because they are based on nearest-neighbour correlations. We find that the best indicator of local order for real crystals is the parameter related to orientational order,  $\langle \Psi_s \rangle$ . In both simulated and experimentally obtained images, the average bond orientational order parameter  $\langle \Psi_s \rangle$  is very high ( $0.9 < \langle \Psi_s \rangle < 1$ ) only when the positional disorder  $\alpha$  is rather small ( $0 < \alpha < 0.05$ ). The shoulder in the simulated curves ( $0.85 \approx \langle \Psi_s \rangle$ ) highlights the region below which  $\Psi_s$  is simply not very sensitive. This is especially evident in the data for the highly disordered computer-generated lattices (CG3), which are not equally random based on their different  $\alpha$  values, but have very similar  $\langle \Psi_s \rangle$  values. Thus, in all subsequent discussions, we use  $\langle \Psi_s \rangle$  as the primary local order parameter.

### 3.3.2 Intermediate-range correlations versus local orientational order

Figure 3.4 examines correlations between local order (through  $\langle\Psi_s\rangle$ ) and longer-range order (through the positional correlation length  $\xi_s$ ). Due to the large number of images in this study, we grouped the data based on different colloidal crystal production techniques in Figure 3.4: convective assembly [26–28, 38, 46, 47, 57–61], electrophoretic assembly [62–64], electrospraying [65], air-liquid interface assembly [25, 66, 67], confinement [48, 68], dip coating [69, 70], spin coating [2, 4, 71] (the majority of which are original to this work), and sedimentation [72].

Based on  $\langle\Psi_s\rangle$  (Figure 3.4i) and  $\xi_s$  data (Figure 3.4j), it is tempting to make quantitative comparisons of crystal quality among different production methods. For example, convective assembly appears to have the potential to produce crystals with the highest  $\langle\Psi_s\rangle$ . Convective assembly is also capable of producing colloidal crystals with relatively high  $\xi_s$ , with spin coating offering a competitive quality, although this technique in most cases seems to be poor in that regard. However, our sampling of data is implicitly biased since published images tend to be highest-quality areas rather than typical examples. This is why we made and measured a larger range of crystal images for one category of samples (spin coating). It is worthy of note that the best spin coated samples are comparable to the best from convective assembly methods, even though our data show that spin-coated crystals can be made with far lower degrees of positional correlation under some conditions.

Figure 3.4k shows the relation between positional correlation length  $\xi_s$  and the average local (orientational) bond order  $\langle\Psi_s\rangle$ .  $\xi_s$  is very small for  $\langle\Psi_s\rangle < 0.9$ , which is another indication that crystals with  $\langle\Psi_s\rangle \leq 0.9$  do not correlate with good crystallinity. This is a reasonable result, since good local orientational order is necessary

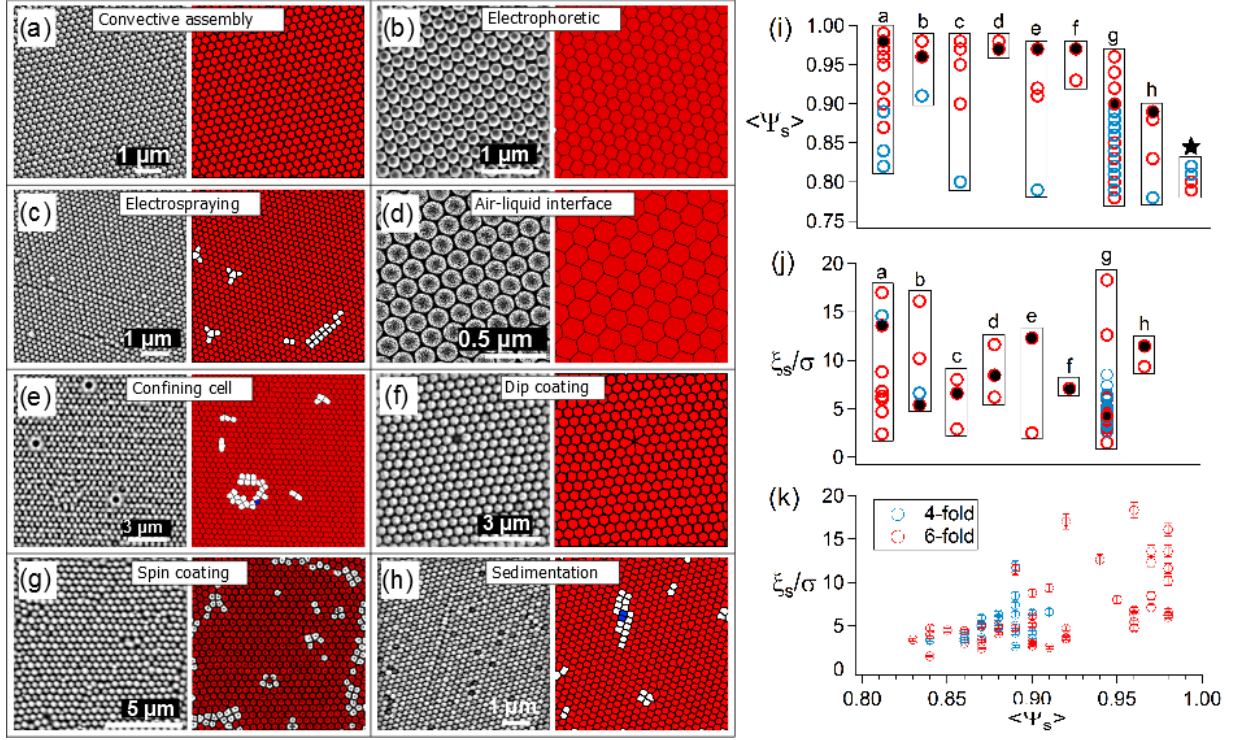


Figure 3.4: Representative images of colloidal crystals produced by (a) convective assembly [38], (b) electrophoretic assembly [62], (c) electrospinning [65], (d) air-liquid interface assembly [25], (e) confinement [48], (f) dip coating [69], (g) spin coating (new to this work), and (h) sedimentation. [72]. Comparisons of (i) average local orientational bond order  $\langle \Psi_6 \rangle$ , and (j) positional correlation length  $\xi_6$ , sorted according to production method. In (i) and (j), the black filled circles correspond to the data points for images (a)-(h). Data points marked with (\*) in (i) correspond to computer-generated random structures. [56] Panel (k) shows the correlation of  $\xi_s$  with  $\langle \Psi_s \rangle$ , including data from colloidal crystals produced by all methods.

for longer range positional correlations.

## **Distinguishing between single domains and polycrystals**

The metrics discussed thus far ( $\langle\Psi_s\rangle$ ,  $\alpha$ ,  $\xi_s$ ) work well to characterize order within a single domain. This is sufficient for many images of colloidal crystals in the literature, due perhaps to the drive to make perfect photonic-grade crystals. However, more disordered crystals are also finding uses in optical applications. [14,17] In an extreme, the average bond orientational order  $\langle\Psi_s\rangle$  is not very informative for a polycrystalline sample containing grains with different symmetry (4-fold versus 6-fold). Instead, for polycrystalline colloidal materials (as are produced routinely by spin coating [2,3]), it is helpful to identify domain sizes. As we will show, these domain sizes are consistent with practical upper limits for the intra-domain parameters  $\langle\Psi_s\rangle$  and  $\xi_s$ .

We found a new and expedient way to assess representative domain sizes based on differences in orientational order.

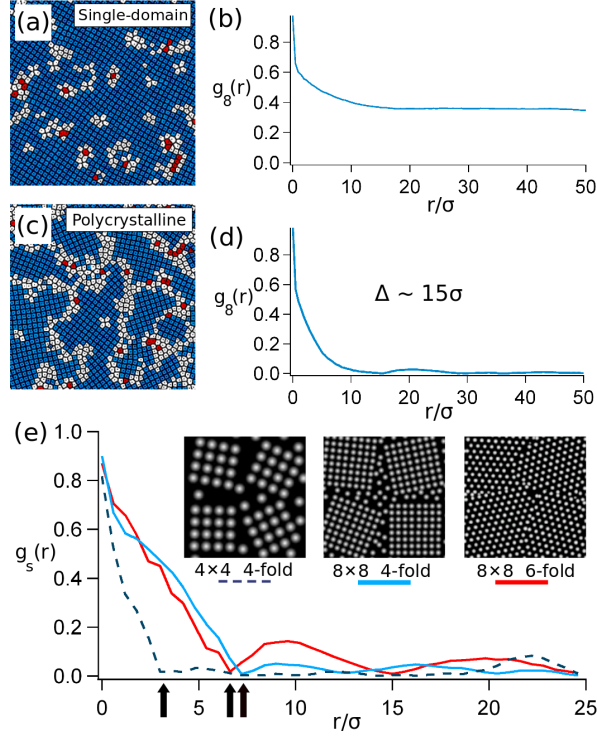


Figure 3.5: Representative orientational correlation functions  $g_s(r)$ . For a single domain (a), there is orientational correlation across the entire image, so  $g_s(r)$  never reaches zero (b). Polycrystals (c) have orientational correlations that go to zero (d) at its representative domain size ( $\Delta_s$ ). (e) Examples of computer-simulated polycrystalline lattices and their corresponding  $g_s(r)$  plots. Arrows show  $\Delta_s$  values (where  $g_s(r) \rightarrow 0$ ) for three simulated polycrystals.

Figure 3.5 shows two representative orientational correlation functions  $g_s(r)$  that have qualitatively different behaviors. When  $g_s(r)$  is calculated over a single domain, a non-zero plateau appears for large  $r$  values (Figure 3.5a,b). However,  $g_s(r)$  decays to zero when the image contains multiple domains that disrupt the orientational correlation (Figure 3.5c,d). We define  $\Delta_s$  as the normalized distance ( $r/\sigma$ ) at which the orientational correlations vanish. These  $g_s(r)$  decays are replicated in simulated polycrystalline lattices (Figure 3.5e).

A representative domain size derived from orientational correlations has two clear benefits for quantitative characterization of colloidal crystals. First, this parameter can distinguish a single domain with defects (Figure 3.5a, with ill-defined  $\Delta_s$ ) from a polycrystalline sample (Figure 3.5c, with a finite  $\Delta_s$ ). Second, the concept of a representative domain size provides a reasonable upper bound for the useful range of intra-domain characterization parameters such as  $\langle \Psi_s \rangle$  and  $\xi_s$ . Figure 3.6a-f demonstrates that higher fractions of  $s$ -fold coordination ( $f_s$ ) correlate strongly with increases in both the average orientational bond order parameter  $\langle \Psi_s \rangle$  and the representative orientational domain size  $\Delta_s$ . We note that, as demonstrated in Figure 3.6g, the orientational domain size is consistently larger than the translational correlation length for all colloidal crystals.

Finally, we address local order in polycrystals. The average bond order  $\langle \Psi_s \rangle$  increases monotonically as the corresponding fraction  $f_s$  increases (Figure 3.6e). When one symmetry dominates ( $< 0.1$  or  $> 0.9$ ), small increases in  $f_s$  lead to large increases in the average bond order. For crystals that contain a mixture of 4-fold and 6-fold regions ( $0.1 < f < 0.9$ ), there is a more modest increase in the average bond order with increasing  $f$ . These results compare well with the trends observed for computer-generated structures (solid lines in Figure 3.6e). Our analyses show that, for a given  $f_s$  value, real colloidal crystals have average bond order values that are consistently equal to or greater than those for computer-generated structures.

We emphasize that  $\langle \Psi_s \rangle$  is calculated only within regions of specific symmetry (4-fold or 6-fold) and is not averaged over the entire image. Thus, the increase in average bond order with higher fractions is a true indication that the local order improves. It is not a trivial artifact related to averaging over ordered and amorphous regions. Figure 3.6f shows a strong correlation between increasing  $f_s$  and increasing domain size  $\Delta_s$ .

### 3.4 Conclusion

Historically, a high degree of perfection was the goal for colloidal crystals for potential use in photonics. However, an increasing number of applications can take advantage of colloidal films with lower degrees of order (such as substrates for surface-enhanced Raman spectroscopy [17]), and even amorphous structures (such as angle-independent structural color [14]). In this context, we find that for 2D characterizations of crystallinity, both orientational and translational measures are useful. For very good crystals, translational measures are often adequate because good translational order implies good orientational order. However, for crystals with higher levels of disorder that lead to polycrystallinity, the orientational measures such as  $\Delta_s$  are more sensitive indicators.

Although the positional correlation lengths are larger for samples with better orientational order, it is a noisy correlation. For example, excellent orientational order ( $\langle\Psi_s\rangle = 0.96$ ) can be found in samples with either very short ( $5\sigma$ ) or very large ( $20\sigma$ )  $\xi_s$  values. Even in single-domain samples,  $\xi_s$  is often limited. Considering the spread of  $\xi_s$  and  $\langle\Psi_s\rangle$  (Figure 3.4), the disappointing conclusion is that no single method can consistently produce only good crystals. Nevertheless, we found that all real crystals have crystallinity metrics ( $\alpha$  and  $\xi_s$ ) that are far better than truly random computer-generated structures.

A useful finding is that the orientational correlation function  $g_s(r)$  is a sensitive way to detect domain size in polycrystalline samples. This orientational domain size  $\Delta_s$  shows a consistent increase as the symmetry fraction  $f_s$  increases. It is also consistently larger than the positional correlation length. Furthermore, the average local orientational order  $\langle\Psi_s\rangle$  in real samples is consistently better than values from simulated samples. This trend is nonlinear as a function of symmetry fraction, which shows once again that  $\langle\Psi_s\rangle$  is a very sensitive order parameter for nearly single-domain

samples ( $f_s = 0$  or  $1$ ), while the symmetry fraction  $f_s$  is more informative for mixed symmetry samples.

It is also interesting to note that we see good agreement with an exponential decay in the  $g(r)$  functions in our images from crystalline samples. It is well known in the literature of two-dimensional phase transitions that an exponential decay suggests short-range order (as is typical for liquids), while a power law decay implies quasi-long-range order (as is typical for 2D solids). [52, 79–82] Since the thickness of many samples in this study are not reported, it is unlikely that most published images correspond to true 2D crystals. Out-of-plane distortions are readily detected from AFM images in our spin coated colloidal crystals, but such distortions are tricky to infer from SEM images. Furthermore, previous studies have demonstrated that there can be different degrees of order among surface and inner layers of multilayer colloidal crystals. [87, 88]

From an overall perspective, the present study is valuable because it compares a large number of published images of colloidal crystals using the same assessment methods. Without this kind of a standardized approach, there are too many disparate methods of qualitative and semi-quantitative characterizations that make it hard to assess advances in controlling order in these materials. The multiple characterizations of order that we use here are relatively straightforward to calculate. In addition, the analysis code we used is available to others upon request. Looking ahead, this set of analysis tools will enable quantitative comparisons between colloidal crystals from new experiments with images of older samples.

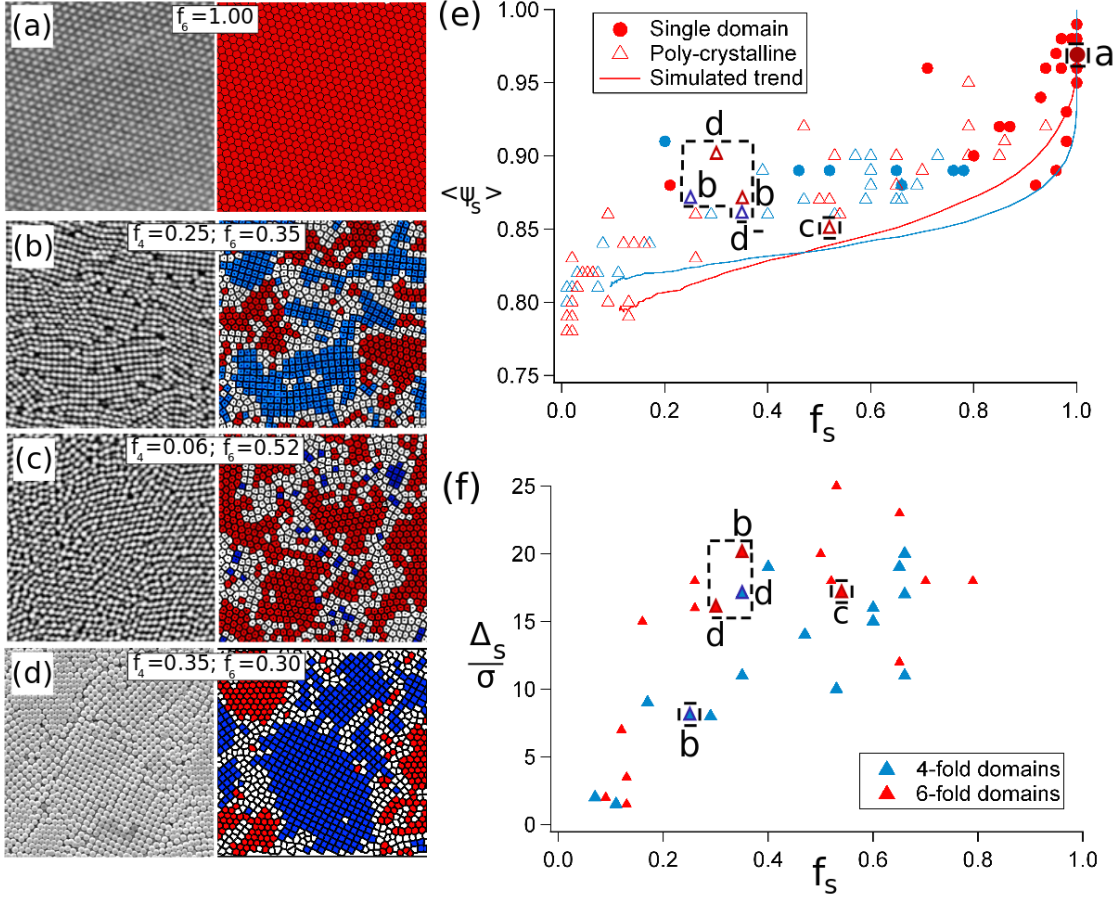


Figure 3.6: (a)-(d) Four representative images with their associated local coordination color maps. In all panels, blue (red) means 4-fold (6-fold) local coordination. (e) Average local bond order  $\langle \Psi_s \rangle$  improves with increasing symmetry fraction  $f_s$ , and is very sensitive when  $f_s \geq 0.9$ . Data points are for real colloidal crystals; trends for computer-generated structures are given by solid lines. In cases where a single domain spanned the entire image, the data points are shown as solid circles. The remaining (polycrystalline) structures are denoted with open triangles. (f)  $\Delta_s$  vs.  $f_s$  shows correlation between these parameters. The data points corresponding to the images in (a-d) are marked by "a", "b", "c", "d" in panels (e) and (f).

## Acknowledgments

We thank A. Coll, V. Ferry, Y. Fu, A. Mihi, and A.J. Wang for providing images that helped this study. We also thank I. Saika-Voivod for discussions on effective simulations of disordered colloidal crystals. A.Y. and K.M.P. thank the Natural Science and Engineering Resource Council (Canada) for funding.

# Chapter 4

## Dynamics of quasi-2D colloidal suspensions

### 4.1 Background

It is a well known fact that colloidal particles in a fluid undergo a random motion, called Brownian motion, which is the result of being constantly hit by the molecules of the fluid medium. This was first observed by Robert Brown in 1827 when he was looking at pollen grains in water under the microscope. Brownian motion was later analyzed by Einstein in 1905 to conclusively establish the corpuscular nature of materials [89]. In fact, Brownian motion is the mechanism at the core of diffusion in colloidal systems [89]. Since Einstein's seminal work, colloidal diffusion phenomena and dynamics of colloidal particles dispersed in fluid media has grown into a vast field of study of both fundamental and applied interest [90–92].

Particle dynamics in 2D or quasi-2D systems has attracted particular interest, because it has its own phase transitions and dynamical characteristics. The system is considered quasi-2D if motion in one dimension is much more limited than the

other two dimensions. The study of 2D dynamics gained impetus with theoretical investigations of a two dimensional phase transition [32] and melting [33], which were followed by computer simulations [34] and experiments [35].

In addition to phase transitions, theoretical and experimental studies of quasi-2D colloidal systems have revealed interesting phenomena like different dynamical behaviors at different time scales, string-like motion [93,94], hopping [95], dynamical heterogeneity [95,96], and cooperative motion [93,95].

In this thesis I have looked at the mean square displacement (MSD) as an indicator of dynamics. With regard to MSD calculations, Schoefield *et al.* [97] theoretically studied the asymptotic long time dynamics of quasi-2D colloidal systems and presented MSD for a wide range of packing fractions of the particles. They also predicted the ratio of long-time to short-time diffusion coefficient as a function of packing fraction. Following this work, Marcus *et al.* experimentally studied the dynamics of quasi-2D colloidal systems at low packing fractions [98]. In this work they reported the experimental verification of the  $\ln(t)/t$  time evolution of the diffusion coefficient (which was predicted theoretically before) via MSD calculations. The time range in this work was up to 300 ms (i.e. experimental time is very short in comparison with the characteristic diffusion time of seconds). Marcus *et al.* [93] looked at the dynamics of quasi-2D colloidal systems at a wide range of packing fractions, from very dilute to dense and reported a host of interesting behaviors such as string-like motion, dynamical heterogeneity, and collective motion. The time range in this work was up to around 1 second (characteristic time  $\tau \sim 1$  s). At higher packing fractions they observed slow down of dynamics at short times. In the following papers, the focus has mostly been on particular aspects of dynamical heterogeneity, glass transition, etc. Particularly, Cui *et al.* in [96] experimentally studied dynamical heterogeneity of a quasi-2D system and also reported the behavior of the MSD at different time scales,

up to 30 seconds (characteristic time  $\tau \sim 0.1$  s). However they do not demonstrate the dynamics to become more subdiffusive as the packing fraction increases. The study of quasi-2D colloidal systems has remained an active research area with focus on different aspects such as phase and glass transitions [99–102] and dynamics under periodic potentials [103, 104].

This chapter presents the results of an experimental study of dynamics of colloidal particles in a quasi-2D system as a function of the packing fraction of the particles for the time ranges from 200 to 1000 seconds (characteristic time  $\tau \sim 100$  s). My experiments provide preliminary data at a wide span of packing fractions, for a relatively wide time range. The goal is to establish a relationship between dynamics and structure, using MSD and symmetry fraction calculations, and to identify the type of dynamical behavior at different times, using the self part of the van Hove function.

## 4.2 Theory

### 4.2.1 Diffusion and subdiffusion

I have studied the dynamics of quasi-two-dimensional colloidal suspensions at different (area) packing fractions  $\phi$ , defined as

$$\phi = N(\pi r^2)/A, \tag{4.1}$$

where  $N$  is the number of particles in the area under study,  $r$  is the radius of each particle, and  $A$  is the total area of the region (e.g. the area I looked at is  $\sim 130 \mu\text{m} \times 130 \mu\text{m}$ ). Theoretically, in two dimensions  $\phi$  can range from 0 to nearly 0.91 (for hexagonal close packing).

At low values of packing fraction the dominant interaction is between colloidal

particles and solvent molecules, but as the packing fraction of the particles increases, the collisions between the colloidal particles themselves become more and more important.

At low enough packing fraction, where the interaction between the particles is negligible the mean square displacement  $W(t)$  of a typical particle in two dimensions follows standard diffusion behavior in 2D [105]:

$$W(t) = \langle (\mathbf{r}(t) - \langle \mathbf{r}(t) \rangle)^2 \rangle = 4Dt \quad (4.2)$$

The  $\langle \mathbf{r}(t) \rangle$  is subtracted to remove the effect of an overall drift. The average is an ensemble average, and in the case of a steady system an average over the time origin is implied by it as well.  $D$  is the diffusion coefficient of the particles in the solvent. So a plot of  $W(t)$  vs.  $t$  can be used to calculate the diffusion coefficient. Also, we have:

$$\log(W(t)) = \log(4D) + \log(t) \quad (4.3)$$

So a plot of  $\log(W(t))$  vs.  $\log(t)$  has a slope of one for pure diffusion. As the packing fraction increases the interactions between the particles could slow down the dynamics. One may then write  $W(t) \sim t^\gamma$ , with  $\gamma < 1$  being referred to as subdiffusive behavior. Therefore, the departure of  $\gamma$  from unity would indicate that mechanisms other than diffusion within the solvent are affecting the dynamics of the particles. In particular, at high packing fractions, caging is notable [95], which means that a particle sees the surrounding particles as a temporary cage at a shorter time scale (which results in subdiffusion). However, collective motion resulting in possible hoppings can push the particle out of its cage, and so at a longer time scale the dynamics would tend to the simple diffusive dynamics with  $\gamma$  closer to one.

### 4.2.2 The self part of the van Hove function

It is reasonable to expect the displacements of the particles over time to be affected by the interactions that the particles have with their surrounding. The self part of the van Hove correlation function (for an isotropic system) is defined as the probability of finding a particle at a distance  $r$  from its original position (at  $t = 0$ ) after time  $t$  [106]. Therefore the shape of this function will be affected by the mechanisms which affect the displacements of the particles. Particularly, the self part of the van Hove function is defined as follows:

$$G_s(r, t) = \frac{1}{N} \left\langle \sum_{i=1}^N \delta(r - |\mathbf{r}_i(t) - \mathbf{r}_i(0)|) \right\rangle. \quad (4.4)$$

The averaging  $\langle \rangle$  indicates an average over the time origin, assuming ergodicity for the system.  $N$  is the total number of particles, and the summation is over all of the particles;  $\mathbf{r}_i(t)$  is the position of a particle at time  $t$ ; and  $\delta$  is the Dirac delta function.

It is known that for a pure Brownian dynamics the  $G_s(r, t)$  takes the following Gaussian form [105]:

$$G_s(r, t) = (4\pi W(t))^{(-d/2)} \exp\left(-\frac{r^2}{4W(t)}\right) \quad (4.5)$$

with  $d$  being the dimensionality of the system.

So when  $G_s(r, t)$  is Gaussian, the function yields the MSD function  $W(t)$ , and in this regime the dynamics should be diffusive. Any deviation from the above functionality would be a sign of deviation from pure Brownian dynamics. Particularly, in the literature, the existence of an exponential tail for the  $G_s(r, t)$  has been associated with the existence of dynamical heterogeneity [107–109], which means the co-existence of

faster and slower regions within the system.

### 4.3 Experimental methods

To obtain a “wet” monolayer colloidal film, which can act as the quasi-2D colloidal system,  $2\ \mu\text{m}$  silica particles (Angstromsphere, catalog number SIOP200-01, polydispersity  $\sim 5\%$ ) are dispersed in ethylene glycol (Sigma-Aldrich, 99.8%, catalog number 324558) and spin coated on a glass substrate similar to the one described in Chapter 2. The gravitational length of the particles is  $\sim 0.1\ \mu\text{m}$ , which is roughly 20 times smaller than the size of the particles, so we may consider the system quasi 2D. Gravitational length is a measure of the gravitational (vertical) spread of the particles at a temperature  $T$ .

Unlike the experiments with evaporative solvents in Chapter 2, control of packing (area) fraction and thickness with ethylene glycol, which evaporates considerably more slowly, was poor. The reason that I used ethylene glycol was to be able to have a wet film in the end. Therefore, the final drying stage (as with the evaporative solvents) that pushes the particles together through capillary forces, and brings about the final compact film is not there. One may still expect to obtain particle packing fractions in the wet film in a predictable way, by controlling the spin coating conditions. But there is one step which brings huge uncertainty to the process, and that is adding a small droplet of ethylene glycol to the wet film after spin coating to minimize bubble formation under the cover that we put on the film (see below). In practice, putting the cover creates uncontrollable flows that pushes an unpredictable number of particles towards the edges and possibly out. Overcoming this difficulty is left as a future work. Six samples were made for the experiments described here. Table 4.1 lists the spin coating conditions used for making each sample, the substrate used in each case,

the range of packing fractions found on each sample, and the number of data points obtained from each one.

	$\Phi_s$	Spin rate	Spin time	Substrate	Range of $\phi$	# of points
1	20%	6000 rpm	30 s	Pure glass	0.03-0.40	4
2	40%	3000 rpm	30 s	Pure glass	0.04-0.69	11
3	40%	6000 rpm	30 s	Patterned ITO glass	0.08-0.53	5
4	40%	6000 rpm	30 s	Patterned ITO glass	0.12-0.22	5
5	40%	2500 rpm	30 s	Pure glass	0.20-0.41	5
6	40%	3000 rpm	30 s	Pure glass	0.63-0.78	19

Table 4.1: List of the spin coating conditions and the substrates used for producing the samples used for the colloidal dynamics study. Also listed is the range of packing fractions  $\phi$  found on each sample, and the number of data points obtained from each. ITO coated glass used was SPI, catalog number 06463B-AB. Patterning was done by Intelligent micropatterning llc ss100 system. The regions imaged for our particle dynamics study were on bare glass, where the ITO coating was removed by micropatterning.

Regions of one packing fraction (to  $\pm 5\%$ ) were typically of the order of  $200 \mu\text{m}$ . Utilizing this fact, a challenge was made into a virtue by studying, in just a handful of samples, the dependence of colloidal dynamics on the regional area fraction  $\phi$ . In fact, I obtained 49 values of  $\phi$  from just 6 samples. In dilute samples, the particle diffusion coefficient is  $\sim 0.008 \mu\text{m}^2/\text{s}$ . Using this, and a lengthscale of 200 microns, one obtains a timescale of  $\sim 1,000,000 \text{ s}$ . For the timescales probed in these experiments ( $< 1000$  seconds), I believe that the regions at different packing fractions can be treated to be at steady state.

For the purpose of video imaging of the colloids a fluorescent dye called fluorescein (Sigma-Aldrich, catalog number 32615) is dissolved in the ethylene glycol which is used as the dispersion medium for the suspension. This enables doing fluorescent microscopy to obtain higher quality images of the particles.

After spin coating, a tiny droplet ( $\sim 1 \mu\text{l}$ ) of EG with fluorescein dissolved in it, is added to the colloidal layer, and then a cover slip is placed on top of the spin

coated layer and the edges are sealed with UV glue (Norland optical adhesive, 61) to prevent evaporation. In fact, the EG droplet is added to reduce the possibility of bubble formation under the cover slip. Afterwards the cell is placed under UV lamp for 30 minutes in order for the UV glue to be cured. To prevent possible bleaching of the fluorescent dye molecules, the top cover slip is covered with a piece of aluminium foil, which of course does not cover the UV glue.

Video imaging of the particles in the cell is done with a Nikon Eclipse 80i optical microscope. An oil immersion 40X lens is used, and the mode of operation is fluorescent microscopy. The sample, which is illuminated with a blue light (FITC excitation 475-490 nm) emits a green light which passes through a filter (FITC emission 505-535 nm) and reaches the detector, which in this case is the CCD of the digital camera (sCMOS pco.edge 3.1) attached to the microscope for digital imaging. A software called CamWare controls the digital camera. In the resulting digital view, which is black and white, the solvent is bright and the particles are dark circular disks. This provides perfect image quality for the subsequent particle tracking analysis. For particle tracking, the video images are inverted in ImageJ to make the particles bright and the surrounding medium dark. The view size is typically  $800 \times 800$  pixels, corresponding to a region of interest of  $\sim 130 \mu\text{m} \times 130 \mu\text{m}$ , while each particle's diameter ( $2 \mu\text{m}$ ) is roughly 12.4 pixels. The video imaging is done at a frame rate of 1 fps or 2 fps.

During the oil immersion microscopy of the cell, I noticed that the image gradually goes out of focus. It turned out to be due to the lab's air flow system that would go on and off roughly every 20 minutes, which would affect the temperature of the environment and so the immersion oil, and causes its refractive index to change gradually with temperature, and therefore would result in losing the focus during the imaging. To fix this issue, I drew the curtains around the microscopy area, which

stabilized the temperature well enough and prevented the gradual de-focusing. None of the samples listed in Table 4.1 were affected by this temperature instability.

## 4.4 Results

As mentioned in Chapter 3, the positional coordinates of the particles are determined using the method introduced by Crocker and Grier [73], implemented in IDL (Interactive Data Language). This enables us to calculate structural parameters, such as local bond order parameter, and hence symmetry fractions. Then, procedures developed by Crocker and Grier [73] and Weeks [110] are used to calculate tracks of individual particles which can be used to calculate dynamical functions. Here I have used positional coordinates information to calculate symmetry fractions, and particle tracking to calculate  $W(t)$  and the self part of the van Hove function. In what follows, I try to establish a relationship between dynamics and structure and also to look at the type of dynamical behavior at different packing fractions and times.

### 4.4.1 Dynamics and structure

Fig. 4.1 shows eight examples of the quasi-2D colloidal structures that are studied. In what follows we see how different parameters respond to the change in packing fraction, and how they are correlated with each other. The van Hove function is calculated for the eight examples shown in Fig. 4.1 for determining the dynamical behavior of the particles at different packing fractions as a function of time.

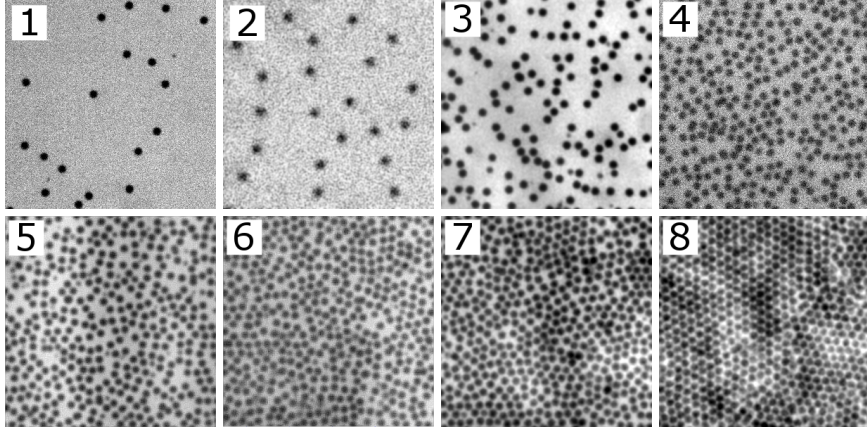


Figure 4.1: Examples of the quasi-2D colloidal structures that are studied, with packing (area) fractions  $\phi = 0.03, 0.04, 0.20, 0.40, 0.49, 0.57, 0.64,$  and  $0.78,$  for 1-8 respectively.

Figure 4.2 shows the  $\log(W(t))$  plots for the 8 samples shown in Fig. 4.1. All of the plots are shown up to  $\log(t) = 2$  (i.e. 100 s). It is seen that  $\log(W(t))$  is linear up to  $\log(t)=2$  for  $\phi$  below 0.6. Up to  $\phi=0.2$ ,  $\gamma$  (the slope of  $\log(W(t))$ ) is very close to one, which means that the dynamics is purely diffusive. At  $\phi=0.4$ ,  $\gamma$  is already significantly different from 1, which indicate that the interaction between the particles has started to take effect. As  $\phi$  increases, dynamics becomes increasingly subdiffusive. However, considering the linearity of the  $\log(W(t))$  up to  $\phi=0.64$ , the short time and the long time behavior of the system are not different. At  $\phi=0.78$ ,  $\gamma$  decreases after roughly  $t = 10$  s. In fact,  $\gamma$  tends to zero at  $t = 100$  s, which indicates trapping of the particles at long times.

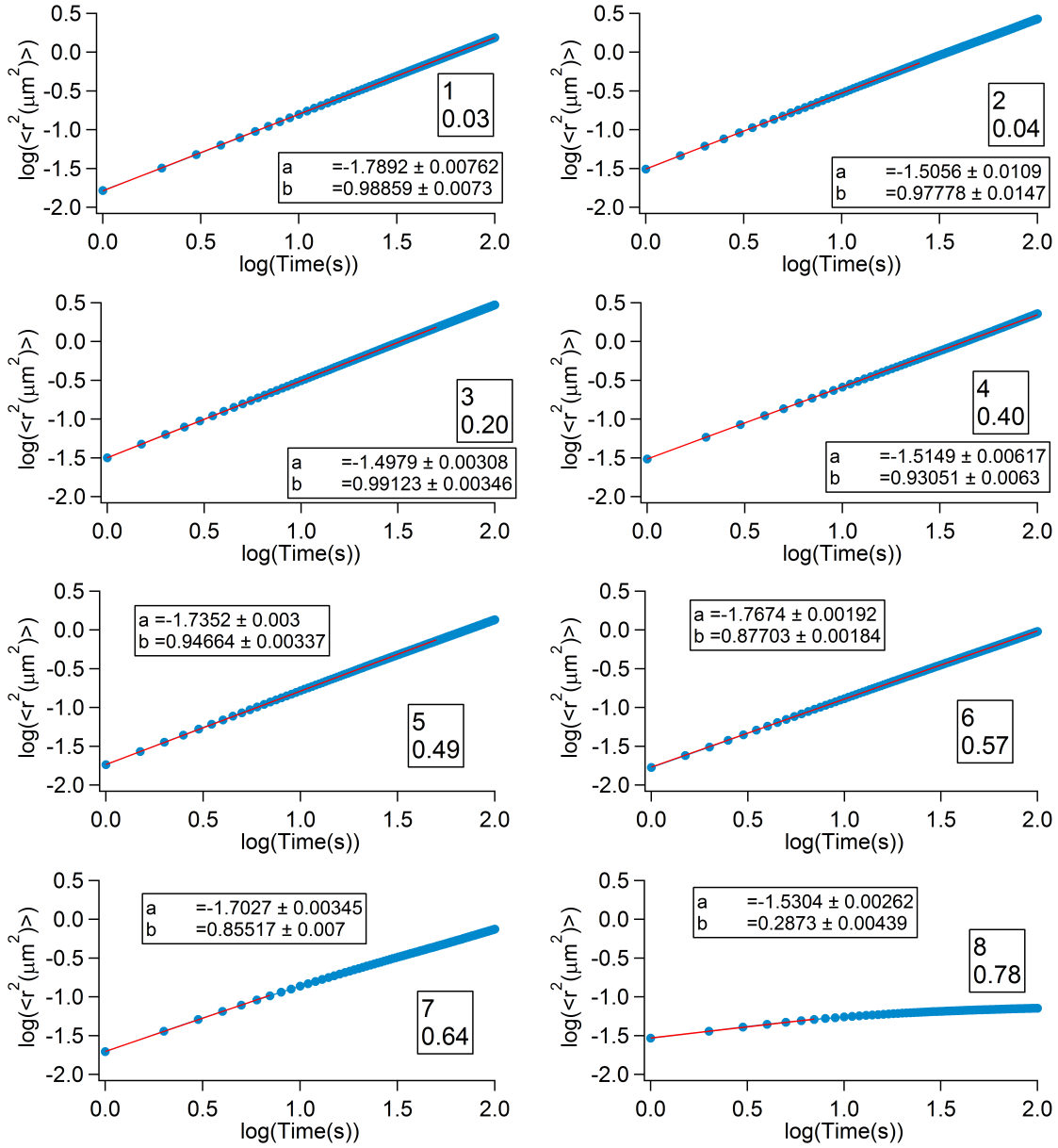


Figure 4.2:  $\log(W(t))$  vs.  $\log(t)$  for the samples shown in Fig. 4.1. the parameter  $a$  is the intercept for the linear fit, and  $b$  is the slope, which is called  $\gamma$  in this chapter.

Fig. 4.3(top) shows  $\gamma$  as a function of  $\phi$  to demonstrate how dynamics responds to the increase in packing fraction. In this plot the data points corresponding to the

8 samples that are studied in more detail are highlighted. Marcus et al. [93] provide similar data, which I have compared with my results in Fig. 4.3. In my case, I have provided considerably more number of points. Also Cui et al. [96] report  $W(t)$  for 2D packing fractions from dilute to dense, but do not report numerical values for the  $\gamma$  vs.  $\phi$ . Kasper et al. [111] report  $W(t)$  for a range of  $\phi$  for a 2D system, but do not report  $\gamma$  vs.  $\phi$  data. Marnette *et al.* [112] present an experimental method to produce 2D colloidal crystals at the interface between two liquids. They observe Brownian motion for the particles, and that the particles crystallize above the packing fraction of 0.7.

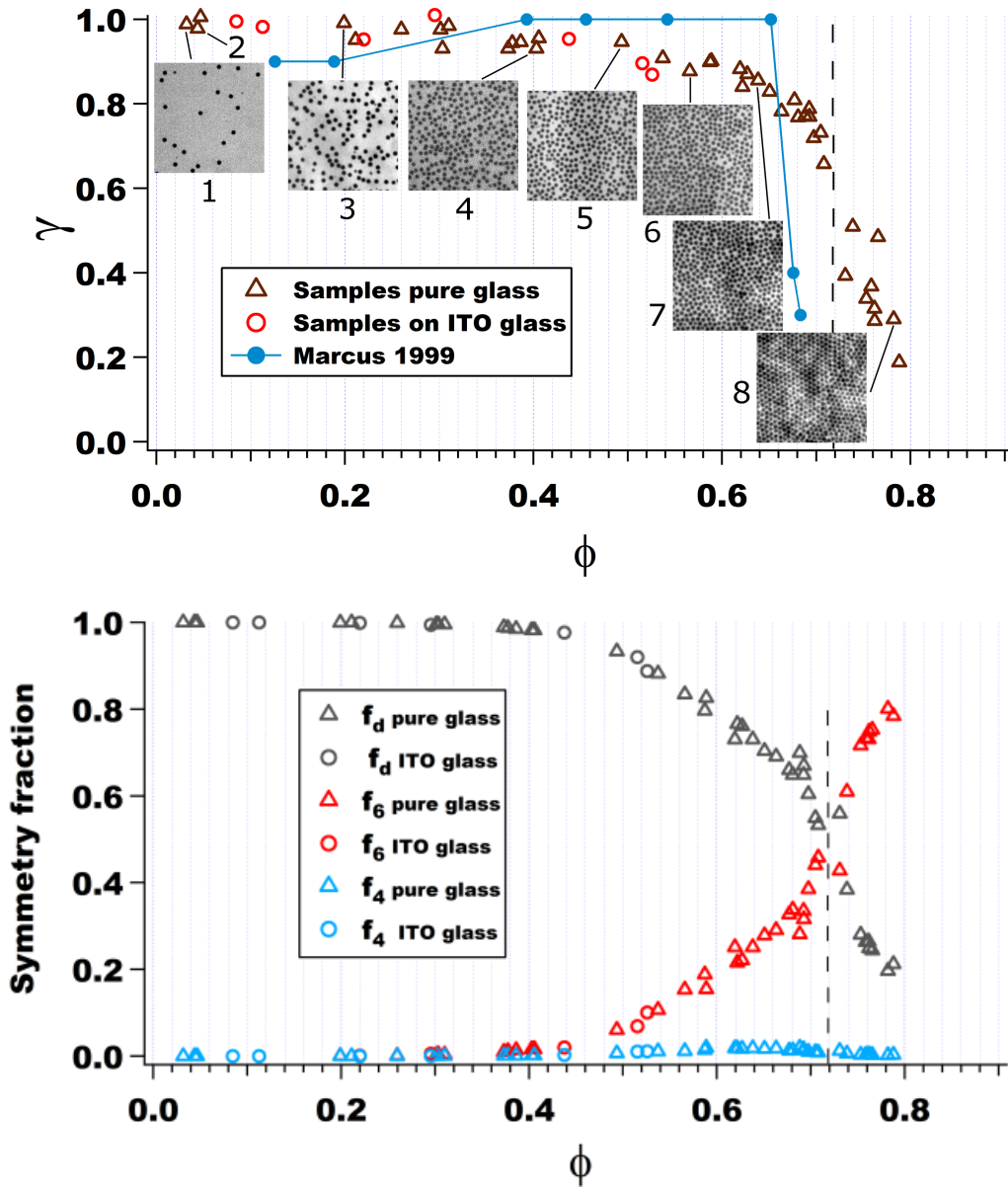


Figure 4.3: **Top:**  $\gamma$  vs.  $\phi$ . Different shapes for data points indicate different substrates in the experiments. The points marked with numbers are the ones for which further analysis is done in this chapter. The insets are snapshots of the colloidal systems associated with the chosen data points. The blue plot is data from Marcus et al. [93] **Bottom:** Symmetry fractions vs.  $\phi$ . The dashed line at  $\phi = 0.719$  indicates the area fraction above which hard disks crystallize [113].

As is seen in Fig. 4.3(top), as the packing (area) fraction  $\phi$  increases,  $\gamma$  decreases, but this trend is very slow up to a packing fraction of 0.6, after which  $\gamma$  goes down more quickly until  $\phi = 0.7$ , and then there is a dramatic drop after  $\phi = 0.7$ . The blue plot in Fig. 4.3(top) compares  $\gamma$  values extracted from [93] with my measurements. It is seen that there is an overall agreement and some differences. Specifically, the concentration at which  $\gamma$  starts to go down sharply is similar in both data sets. Also before this concentration,  $\gamma \approx 1$  in both data sets. However, in my results, initially there is a gradual downward trend as the concentration increases, while in Marcus *et al.* a roughly opposite trend is seen, and then the drop appears sharper.

Symmetry fraction calculations give us a way to see how dynamics and structure correlate with each other. Fig. 4.4 is an indication of such a correlation. It shows that the  $\gamma$  value increases as the fraction of disordered local structure increases, or in other words, the dynamics is more sub-diffusive when there is more order within the system. The curve running among the data points is only a guide to the eyes. At a closer look we observe the following details: there are roughly three regions, one below  $(f_d, \gamma) = (0.77, 0.84)$ , corresponding to  $\phi \gtrsim 0.6$ , a second above  $(f_d, \gamma) = (0.77, 0.84)$  but below  $(f_d, \gamma) = (0.98, 0.93)$ , corresponding to  $0.5 \lesssim \phi \lesssim 0.6$ . The last region ( $f_d > 0.98$ ), corresponding to  $\phi \lesssim 0.5$ , shows that there appears to be a small decrease in gamma even in very dilute suspensions where there is nothing apparent structurally. The change in the trend at  $(f_d, \gamma) = (0.77, 0.84)$  ( $\phi \sim 0.6$ ) is noticeable in the sense that this is the  $\phi$  value at which  $\gamma$  starts a sharper downtrend in  $\gamma$  vs.  $\phi$  plot (Fig. 4.3(top)).

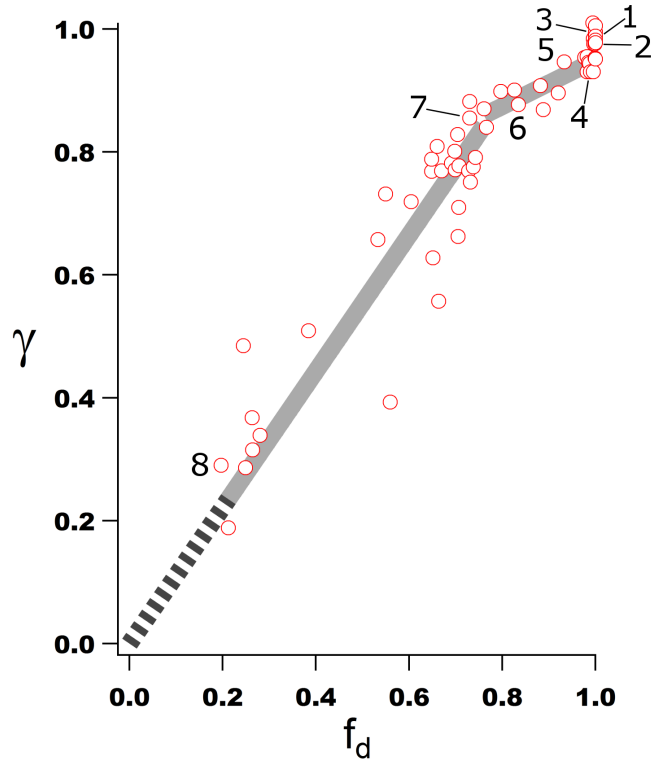


Figure 4.4:  $\gamma$  vs. Disordered fraction for all of the samples. The dynamics is more sub-diffusive when there is more order in the system.

Looking at other symmetry fractions yield more detailed information. In fact, comparison between how 6-fold symmetry on the one hand, and  $\gamma$  on the other hand, respond to the change in  $\phi$  (Fig. 4.3(top & bottom)) reveals that there are subtle differences between the response of the structure and that of the dynamics: from  $\phi \sim 0.4$  to  $0.6$  the rate of slowdown of dynamics (the slope of  $\gamma$  vs.  $\phi$ ) is moderate; between  $0.6$  and  $0.7$  the slowdown rate is considerably faster; and then after  $0.7$  the curve drops very sharply. However the 6-fold symmetry fraction's response is not exactly like that. Between  $\phi \sim 0.4$  to  $0.7$  it increases with more or less a steady rate, and after  $0.7$  the rate becomes faster, but overall after  $\phi \sim 0.4$  one can say that the rate of change of 6-fold symmetry is considerably steadier than the rate of

change of  $\gamma$ . As a further observation,  $\phi \sim 0.7$  is the crystallization packing fraction, since  $f_6$  crosses  $f_d$  at this packing fraction. In comparison, in the phase diagram for hard disks [113] one sees that the structure is liquid-like below  $\phi = 0.706$ , hexatic (long-range orientational order, short-range translational order) between  $\phi = 0.706$  and  $\phi = 0.719$  and solid-like (crystallized) above  $\phi = 0.719$ . These compare well with our observation of  $\phi \sim 0.7$  as a critical value.

A possible reason for the the difference in the response of  $\gamma$  and  $f_{hex}$  to the change in  $\phi$  could be as follows: to calculate  $f_6$  one looks at the neighborhood around each particle and if  $|\Psi_6|$  (the local bond order parameter) for that particle is higher than the threshold, it is counted as a hexagonal neighborhood/particle (See Section 3.2.1 for details). This is done for all of the particles to obtain the total number of particles with hexagonally symmetric neighborhoods. So in this process there is no averaging. Finally, this number is divided by the total number of particles to obtain  $f_6$ . Now, if there is a higher-than-average-density cluster somewhere with slow dynamics, somewhere else there would be a lower-than-average-density region with fast dynamics; but to obtain MSD we average over all of the particles, and if the existence of a cluster can reduce the gamma value, the existence of the low-density region will counter this effect, particularly because they both contribute to the final MSD. So, according to this argument, it seems that the existence of the cluster has pushed the  $f_6$  value up, but it is screened from having direct effect in the MSD by averaging over all of the particles. So, in short,  $f_6$  increases relatively quickly by the formation of local clusters, while increase in  $\gamma$  value is partly hampered by the averaging process. This for now is more of a conjecture than a justified observation. A justification for this is left as a future work.

To see what happens to the average local order as the packing fraction changes, average  $\Psi_6$  is plotted against  $\phi$ . The average is calculated in two ways: average over

the 6-fold regions ( $\langle\Psi_6\rangle$ ), and average over the entire image ( $\langle\Psi_6\rangle_{tot}$ ).  $\langle\Psi_6\rangle$  is not reported below  $\phi = 0.4$ , because there is no 6-fold order within the system below this  $\phi$  value (see Figure 4.3(Bottom)). We see that in both cases  $\phi \sim 0.7$  is where the average local bond order shows a significant rise. Particularly,  $\langle\Psi_6\rangle$  seems almost unchanged below  $\phi \sim 0.7$ .

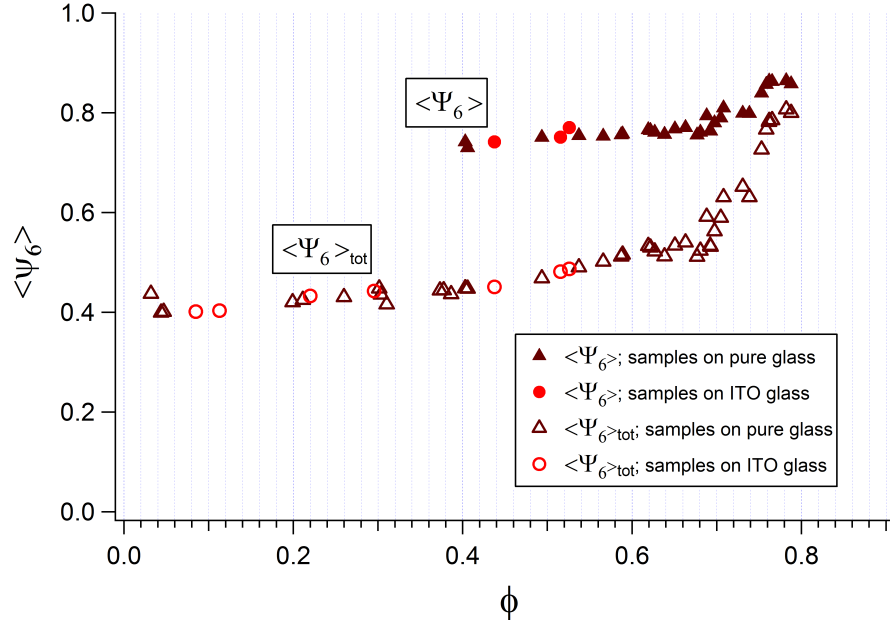


Figure 4.5:  $\Psi_6$  averaged over the 6-fold regions ( $\langle\Psi_6\rangle$ ), and averaged over the entire image ( $\langle\Psi_6\rangle_{tot}$ ), as a function of area fraction  $\phi$ .

#### 4.4.2 The van Hove function

The self part of the van Hove function has the following form for an isotropic, purely diffusive system in 2D [106]:

$$G_s(r, t) = \frac{1}{4\pi Dt} \exp\left(\frac{-r^2}{4Dt}\right), \quad (4.6)$$

where  $r$  is displacement,  $t$  is time, and  $D$  is the diffusion coefficient for the colloidal particles in the solvent. This equation is normalized, i.e.  $\int_0^\infty (2\pi r)G_s(r,t)dr = 1$ .

I examine the dependence of  $\ln(G_s(r,t))$  on time  $t$ , for dilute and concentrated suspensions. So a good fit for  $\ln(G_s(r,t))$  would be:

$$f(r,t) = \ln\left(\frac{1}{4\pi Dt}\right) - \left(\frac{r^2}{4Dt}\right), \quad (4.7)$$

which is a quadratic function. Both the coefficient of the quadratic term and the intercept yield the diffusion coefficient.

However, there are a couple of complications which make some changes to the above fitting function necessary. First is the possible presence of stuck particles, which causes a peak to show up at small  $r$  values in the  $G_s(r,t)$ . Second is the possible existence of an overall sample drift, which causes a non-zero peak position. Fig. 4.6(a) shows an example.

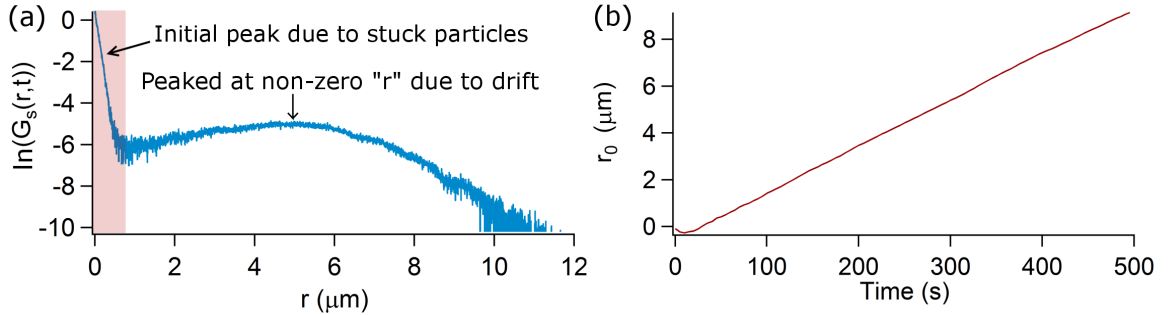


Figure 4.6: (a) The  $\ln(G_s(r,t))$  for  $\phi = 0.03$  at  $t = 250.5$  s. The initial peak is due to stuck particles. The shaded region is excluded from the curve fit. Also the curve is peaked at  $r \neq 0$ , due to the overall drift of the particles. (b) The position of the peak due to drift ( $r_0$ ) vs. time.

Obviously one does not want to include the peak due to stuck particles in the fitting. However, as was pointed out before, the normalization is valid for the specific functional form 4.6, in the range between 0 and  $\infty$ . In my  $G_s(r, t)$  calculations I have normalized the  $G_s(r, t)$  regardless of the existence of the initial peak, and so if I want to use the form 4.7 to fit the result, I need to include a parameter to correct for the existence of the peak due to the stuck particles. Also the non-zero peak position due to drift is taken care of by replacing  $r$  with  $r - r_0$  in the fitting function. Fig. 4.6(b) shows  $r_0$  as a linear function of time which indicates a steady drift. So the form that I have used for fitting is

$$f(r, t) = \ln\left(\frac{1}{4a\pi Dt}\right) - \left(\frac{(r - r_0)^2}{4Dt}\right), \quad (4.8)$$

which contains an “ $a$ ” parameter to include the stuck particles’ effect, and the  $r_0$  to include the drift.

Equation 4.9 can be expanded as:

$$f(r, t) = \ln\left(\frac{1}{a}\right) + \ln\left(\frac{1}{4\pi Dt}\right) - \left(\frac{(r - r_0)^2}{4Dt}\right). \quad (4.9)$$

Including the correction parameter  $a$  would mean an adjustment of  $\ln(\frac{1}{a})$  to the  $y$ -intercept of the fitting function.

In the following results presented here, there are cases where  $\ln(G_s(r, t))$  is not quadratic (equivalently  $G_s(r, t)$  is non-Gaussian). Non-Gaussian behavior for  $G_s(r, t)$  (particularly, the presence of an exponential tail) is believed to be a sign of heterogeneous dynamics [107, 109]. In [107], Chauduri *et al* studied different systems near glass transition, and showed that in all of them the self part of the van Hove function has an exponential tail as a universal indication of dynamical heterogeneity. Stariolo *et al.* in [109] studied the dynamics of a Lenard-Jones system *via* molecular dynamics

simulation. They identified length and time scales associated with transition from a dynamically heterogeneous regime (indicated by the exponential tail for the van Hove function) to Gaussian diffusion.

It should be noted that the initial peak at very small  $r$  in Figures 4.7(a) and 4.7(c) come from a small fraction (less than 10%) of stuck particles (see Appendix A, Section A.0.2, where we see that its contribution to  $\int_0^\infty (2\pi r)G_s(r, t)dr$  is small).

### 4.4.3 Gaussian vs. non-Gaussian dynamics

The van Hove function is used to study the dynamical behavior of the quasi-2D monodisperse colloidal systems, namely, whether the behavior is Gaussian (Brownian) or non-Gaussian. One can also extract diffusion coefficient as a function of time (wherever the behavior is Gaussian) for different packing fractions. In the following discussion, it should be noted that a Gaussian  $G_s(r, t)$  is equivalent to a quadratic  $\ln(G_s(r, t))$ , and a  $G_s(r, t)$  with an exponential tail is equivalent to a  $\ln(G_s(r, t))$  with a linear tail. In what follows  $\ln(G_s(r, t))$  will be presented, but I would talk about Gaussian vs. exponential instead.

Fig. 4.7 shows examples of the van Hove functions at  $\phi = 0.03, 0.40,$  and  $0.64$ . We see Gaussian behavior at all times for  $\phi = 0.03$  (Fig. 4.7(a)). For larger  $\phi$ ,  $G_s(r, t)$  has an exponential tail at the earliest times (see the inset of Fig. 4.7(b)), but is Gaussian at later times. For  $\phi = 0.64$  (Fig. 4.7(c)),  $G_s(r, t)$  exhibits non-Gaussian behavior at all times. (The detailed van Hove function plots for all of the 8 selected examples are presented in Appendix A.) This is summarized in Fig. 4.8. So, once again  $\phi \sim 0.6$  shows up as a transition point. In this case, the dynamical behavior is non-Gaussian at all times above this packing fraction (within our time resolution and time range limit). This observation suggests a correlation between the slowdown of dynamics (as manifested in a sharper downtrend in  $\gamma$  after  $\phi \sim 0.6$ ) and the type of dynamical

behavior, indicated by the van Hove function.

Structural and dynamical measures are presented in this chapter for a range of packing fractions and a range of times. I have also presented a more detailed analysis for a few selected examples. In the literature the relevant works that can be compared with the results here are as follows: Kasper *et al.* [111] report non-Gaussian parameter for packing fractions from 0.4 to 0.56 as a function of time. Generally, it has higher values at earlier times, and the highest value is seen for  $\phi = 0.56$  where the Gaussian parameter peaks early in the time range and then goes down. Marcus *et al.* [93] look at  $G_s(r, t)$  at different  $\phi$  values (from  $\sim 0.10$  to  $\sim 0.70$ ) at different times (33 ms, up to 1.3 s) and observe a non-Gaussian tail (in fact, a low peak in the tail) for lower packing fractions. As mentioned before, Marnette *et al.* observed  $\phi \sim 0.7$  as the packing fraction at which crystallization starts. In this chapter we saw that this is roughly the packing fraction at which  $f_6$  starts to supersede  $f_d$ , and also  $\gamma$  to plunge down sharply, although we observed that subdiffusion had started well before (at  $\phi \sim 0.4$ ). Also we saw that the dynamics is non-Gaussian at all times, starting from  $\phi \sim 0.6$ , which is not too far from the crystallization packing fraction reported by Marnette *et al.*

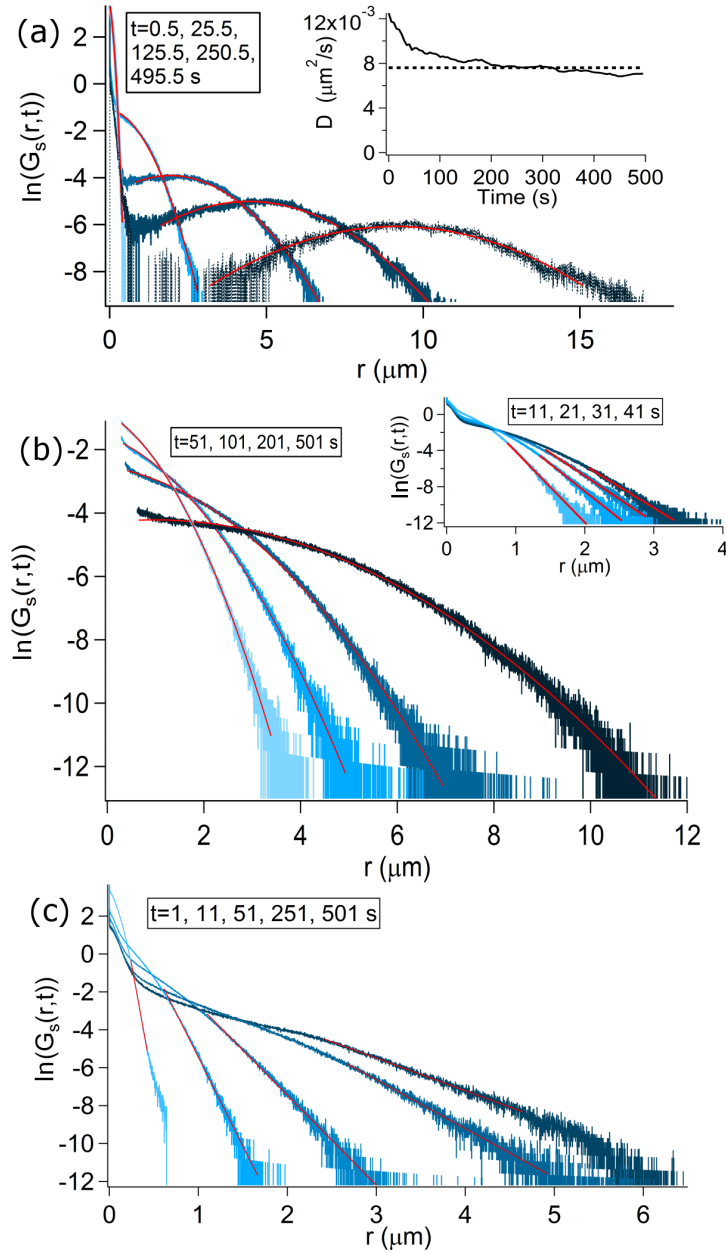


Figure 4.7:  $\ln(G_s(r,t))$  vs.  $r$  for 3 packing fractions,  $\phi = 0.03, 0.40,$  and  $0.64$ . (a)  $\phi = 0.03$  (Example 1 in Fig. 4.3(top)). The behavior is Gaussian in the whole time range. The inset is the diffusion coefficient ( $D$ ) vs. time, obtained from the fit to the  $\ln(G_s(r,t))$ . The dashed line in the inset is  $D$  obtained from  $W(t)$ . (b)  $\phi = 0.40$  (Example 4 in Fig. 4.3(top)).  $G_s(r,t)$  is non-Gaussian up to 41 s; it has an exponential tail between 11 s and 41 s. It is Gaussian for the rest of the time range. (c)  $\phi = 0.64$  (Example 7 in Fig. 4.3(top)).  $G_s(r,t)$  has an exponential tail for the whole time range. In each plot, the  $\ln(G_s(r,t))$  for a later time moment reaches to greater  $r$  values, and is represented in a darker color.

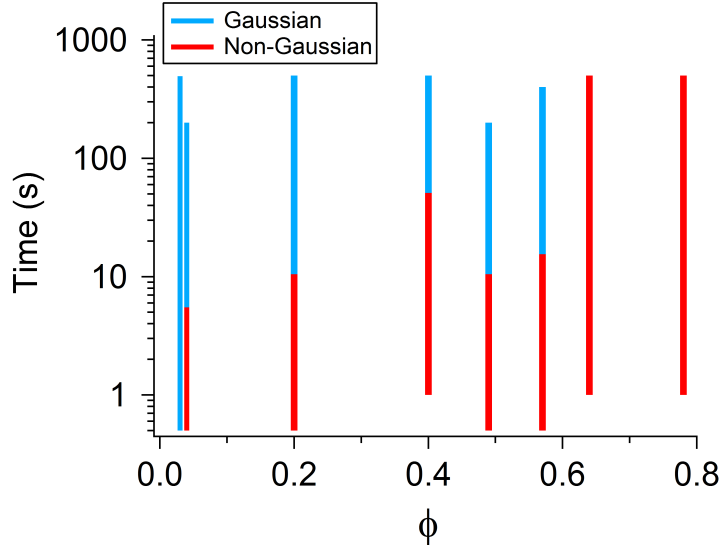


Figure 4.8: The time range for non-Gaussian and Gaussian behavior for the 8 examples with  $\phi = 0.03, 0.04, 0.20, 0.40, 0.49, 0.57, 0.64, 0.78$ .

For the samples and the times at which the  $G_s(r, t)$  is Gaussian, the diffusion coefficient is calculated. Also the diffusion coefficient is calculated from the slope of  $W(t)$ . The average  $D$  goes down as  $\phi$  increases. Fig. 4.9 shows that the two measures for the diffusion coefficient are close and follow similar trends, which is a good consistency check.

The existing literature gives an idea of the physical meaning of this set of behaviors. In the literature, an exponential tail of the  $G_s(r, t)$  has usually been associated with the concept of the lifetime of a “dynamical heterogeneity”, which is observed (or expected) to exist until some characteristic time and the Gaussian behavior to be recovered at longer times [107–109]. So the fact that we observe exponential behavior at earlier times seems consistent with the literature. One can conjecture the existence of local clusters, that is, regions with higher than average particle density, within which particles have slower than average dynamics, and consequently regions with lower than average density and faster than average dynamics. The crossover time

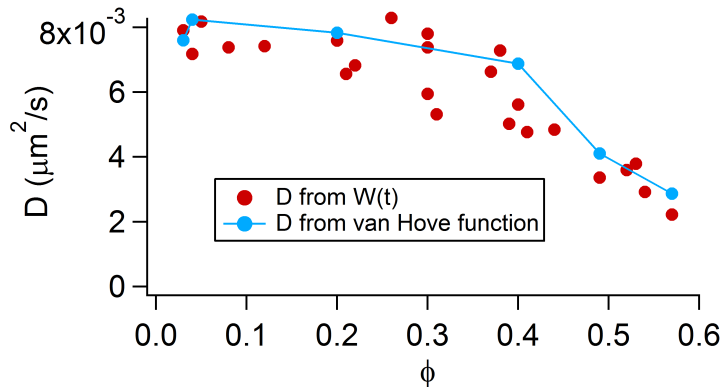


Figure 4.9: Average  $D$  obtained from quadratic fit to  $\log(G_s(r, t))$ , as a function of  $\phi$  (the blue plot), and the  $D$  obtained from  $W(t)$  as a function of  $\phi$  (the red data points).  $D$  goes down as  $\phi$  increases.

after which Gaussian behavior is recovered should be related to the average cluster size. At low packing fractions, clusters have limited average size and their effect would be averaged out when the average particle displacement becomes bigger than their average size. At a high enough packing fraction (above  $\phi = 0.6$ , according to Fig. 4.8) the clusters are so big that the associated time scale encompasses all of the time range that is looked at, i.e. up to  $t \sim 500$  s. In microscopy images one could find these regions simply by showing fast and slow particles in different colors. This will provide a good way to test the above conjecture.

## 4.5 Future work

In this chapter, there are a few points which require further work:

- Finding an experimentally robust way for producing wet colloidal films of controllable thickness and packing fraction. Since the addition of an extra droplet of the solvent to the wet film after the spin coating is considered as the main source of unpredictability, one should attempt to remove this step. Using a solvent less viscous than ethylene glycol can be helpful, since it may result in a

smoother wet layer after spin coating, which may eliminate the need to add the extra droplet to prevent bubble formation.

- Considering the arguments presented in the discussions, based on the assumption of the existence of local clusters, and the consequent dynamical heterogeneity, it is worthwhile to do further analysis to identify this feature (i.e. local clusters, in case they exist), and to establish the link between their existence and the dynamics of the system. In particular, to see how their existence would possibly account for the difference between the response of  $\gamma$  to the change in  $\phi$ , and the response of  $f_6$ . Also, how they would account for the crossover time from non-Gaussian to Gaussian behavior, at different packing fractions.
- To do the van Hove function calculation for all of the samples (data points presented in Fig. 4.3(top)), to obtain more detailed information about the dynamical behavior at different packing fractions.

## 4.6 Conclusion

This chapter presented an inter-relationship between structure and dynamics in quasi-2D colloidal suspensions, as the packing (area) fraction  $\phi$  changes. The type of the dynamical behavior at different packing fractions and times were also discussed. In particular, a detailed plot of the slope of  $\log(W(t)), \gamma$ , as a function of packing fraction  $\phi$  (Fig. 4.3(top)) was presented. According to this plot the packing fraction value above which a departure from pure diffusion becomes significant is  $\sim 0.4$ . From  $\phi = 0.4$  to  $\phi = 0.6$ ,  $\gamma$  decreases slowly, but from  $\phi = 0.6$  to  $\phi = 0.7$  there is a sharper drop, and then after  $\phi = 0.7$  it plummets abruptly. Together with the slow down of dynamics (decrease in  $\gamma$ ), 6-fold symmetry starts to show up in the system (Fig. 4.3(bottom)), i.e. after  $\phi = 0.4$ ,  $f_6$  starts to take off from around zero and goes

up more or less steadily as  $\phi$  increases. Another indication of correlation between dynamics and structure is the observation that as the disorder fraction goes up,  $\gamma$  tends toward 1 (Fig. 4.4). In this case,  $\phi \sim 0.6$  is again a packing fraction at which a change in the trend of  $\gamma$  vs.  $\phi$  is noticeable.

By examining the self part of the van Hove function,  $G_s(r, t)$ , I was able to determine the time range and  $\phi$  values for which the dynamical behavior is Gaussian, or non-Gaussian. Specifically, we see that below  $\phi \sim 0.6$  the dynamics is non-Gaussian for very small times, and at later times Gaussian behavior is recovered (Figs. 4.8 and 4.7). This could mean that at earlier times dynamical heterogeneity exists. Above  $\phi \sim 0.6$  dynamics is non-Gaussian for the whole time range.

The  $G_s(r, t)$  study allowed the calculation of the diffusion coefficient ( $D$ ) as a function of time. At the same time, I was able to extract  $D$  from  $W(t)$ . The average  $D$  values from  $G_s(r, t)$  agree with the ones obtained from  $W(t)$  (Fig. 4.9). It is seen that  $D$  goes down as  $\phi$  goes from 0.03 to 0.57, which is the range for which  $D$  was possible to obtain from both methods.

# Chapter 5

## Conclusion

This thesis presents the results of three projects: Thickness measurements of spin coated colloidal films with volatile solvents, quantitative characterization of crystalline structure of colloidal films, and a study of the dynamics of quasi-2D colloidal systems.

I started with producing spin coated colloidal film with the purpose of showing the reproducibility of the process and studying the way thickness depends on spin coating parameters, and also providing conditions for producing films of definite thickness. These spin coated colloidal films possess crystalline structure, because they are made of monodisperse spherical colloids. Therefore we aimed at a quantitative characterization of their crystalline structure in terms of local and overall parameters, with regard to positional and orientational order. The tools used in the structure characterization provided a chance to study the relationship between structure and dynamics in a colloidal system. Therefore, the final project was a study of the dynamics of colloids in quasi-2D colloidal suspensions.

## Evaporative spin coated colloidal crystals

In this project, the reproducibility of spin coating for producing colloidal films of definite thickness is demonstrated. Also it is shown that a proper washing procedure for the substrate improves the reproducibility. It has been known from previous studies that higher concentrations and lower speeds result in thicker films [2, 4]. However in this work these results were specifically confirmed with highly evaporative solvents of MEK and MPK. Also it is shown that the thickness is not dependent on the volume of the suspension used for spin coating. Also new to this work is a list of spin coating conditions for producing films of various thicknesses, especially a monolayer film. From there, conditions for obtaining sub-monolayer follows.

It was known by our group that during AFM imaging, the AFM tip scratches the surface of the spin coated colloidal films. As a side product of this project I found a way to stabilize the particles (to improve AFM imaging) by spin coating a PMMA layer on top of the colloidal film, without any significant change of its thickness.

## Quantitative metrics for assessing positional and orientational order in colloidal crystals

For 2D characterizations of crystallinity, both orientational and translational measures are useful. For very good crystals, translational measures are often adequate because good translational order implies good orientational order. For crystals with larger amounts of disorder that lead to polycrystallinity, however, orientational measures such as  $\Delta_s$  are a more sensitive indicator.

The positional correlation length is larger for samples with better orientational order, but it is a noisy correlation. Nevertheless, a useful finding is that the orientational

correlation function  $g_s(r)$  is a sensitive way to detect domain size in polycrystalline samples. This orientational domain size  $\Delta_s$  shows a consistent increase as the symmetry fraction  $f_s$  increases. It is also consistently larger than the positional correlation length. Furthermore, the average local orientational order  $\langle \Psi_s \rangle$  in real samples is consistently better than values from simulated samples. This trend is nonlinear as a function of symmetry fraction, which shows once again that  $\langle \Psi_s \rangle$  is a very sensitive order parameter for nearly single-domain samples ( $f_s = 0$  or  $1$ ), while the symmetry fraction  $f_s$  is more informative for mixed symmetry samples.

An interesting observation in our analysis of the images of colloidal crystals was that the  $g(r)$  could be fit with an exponentially decaying function which, as is well known in the literature of 2D structures, is indicative of short range order, while a power law decay means quasi-long-range order [52, 79–82]. However, since in many cases the thickness information was missing, drawing any particular conclusion from this observation should be done with care.

The overall value of this work lies in the fact that it offers a unified framework for quantitative assessment of 2D order in colloidal crystals that makes assessing the future advances in controlling order in colloidal crystals (and their comparison with the existing results ) straightforward.

## Dynamics of quasi-2D colloidal suspensions

The dynamics of quasi-two-dimensional colloidal suspensions was studied as a function of the area fraction  $\phi$ . Many area fractions were accessed by utilizing the variation in packing within samples - the timescales probed were short enough, that we do not think that long-time transients play an important role, but a detailed justification of this is left for future work

The dynamics study presents a detailed plot of the slope of  $\log(MSD)$  vs.  $\log(t)$  ( $\gamma$ ) as a function of packing fraction ( $\phi$ ). According to this plot, after  $\phi = 0.4$  the dynamics starts to slow down (i.e.  $\gamma$  goes down) and at the same time disorder decreases in the system and 6-fold symmetry starts to appear. This trend continues with increasing the packing fraction, although the details of the trend for the decrease in  $\gamma$  is different from the trend for the increase in  $f_{hex}$ . Particularly,  $\gamma$  goes down slowly as  $\phi$  goes toward 0.6, and at  $0.6 < \phi < 0.7$  this rate speeds up and then  $\gamma$  plummets down sharply after  $\phi \sim 0.7$ ; but the rate of increase of  $f_{hex}$  after  $\phi \sim 0.4$  is more or less steady.

Also, I was able to determine the time range and  $\phi$  values for which the dynamical behavior is Gaussian, or non-Gaussian, by examining the self part of the van Hove function,  $G_s(r, t)$ . Specifically, we see that before  $\phi \sim 0.6$  the dynamics is non-Gaussian for very early times, and at later times Gaussian behavior is recovered. This means that at earlier times dynamical heterogeneity exists. Above  $\phi \sim 0.6$  dynamics is non-Gaussian for the whole time range.

The  $G_s(r, t)$  calculation allowed the calculation of the diffusion coefficient ( $D$ ) as a function of time. We were also able to extract  $D$  from mean square displacement plots. The average  $D$  values from  $G_s(r, t)$  agree with the ones obtained from MSD.  $D$  goes down as  $\phi$  goes from 0.03 to 0.57.

This dynamics study reveals how the slow down of dynamics is correlated to the emergence of order in the quasi-2D colloidal system as the packing fraction increases. Also, it identifies the type of dynamical behavior at different packing fractions as a function of time.

# Appendix A

## van Hove function for selected examples

Eight examples are highlighted in Fig. A.1 (which is the reproduction of Fig. 4.3 for convenience of reference). Figs. A.11 to A.9 illustrate the results of  $G_s(r, t)$  calculations for these examples. The results of these calculations are summarized in Fig. 4.8. In short, the  $G_s(r, t)$  calculations show that at  $\phi$  values lower than 0.6, the  $G_s(r, t)$  is non-Gaussian at early times and Gaussian at later times. After  $\phi \sim 0.6$ , the  $G_s(r, t)$  is non-Gaussian at all times.

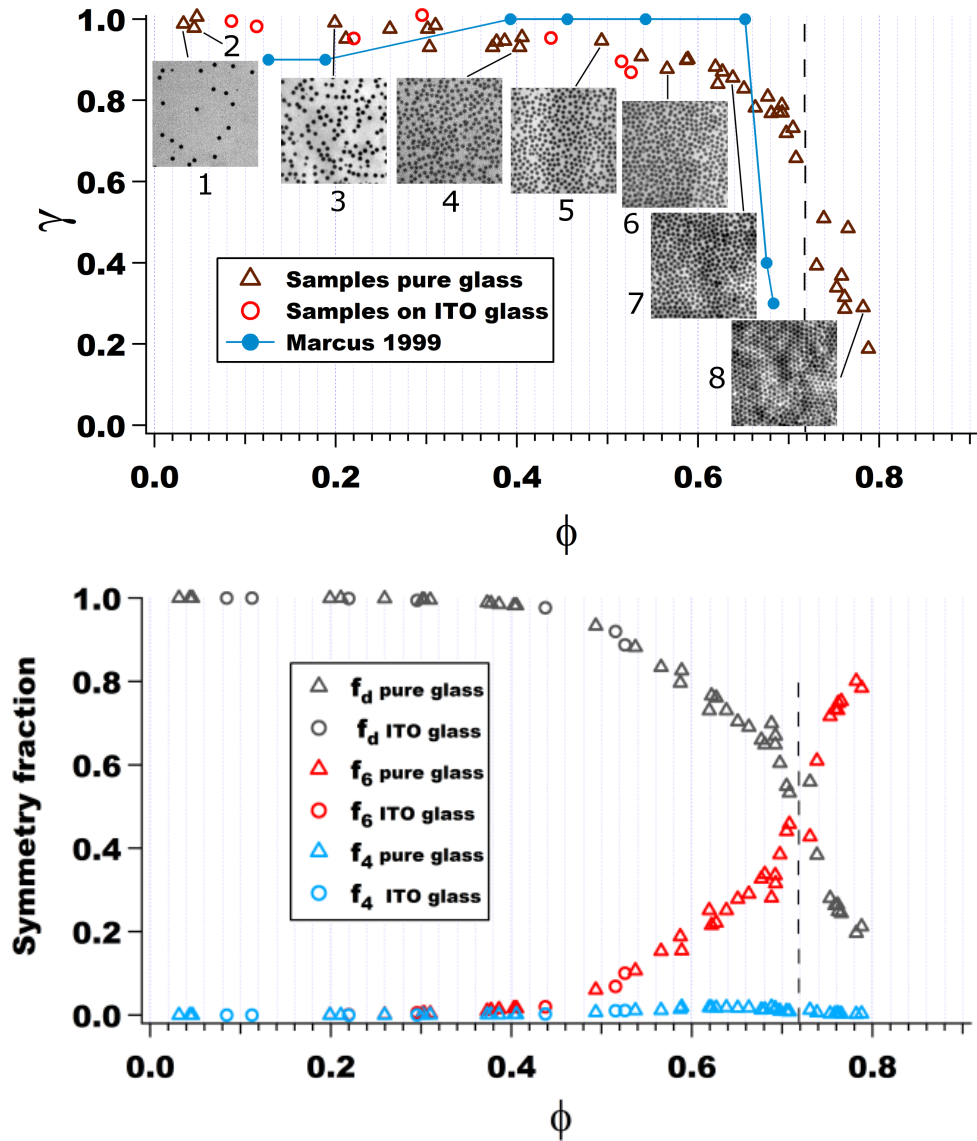


Figure A.1: Reproduction of Fig. 4.3. **Top:**  $\gamma$  vs.  $\phi$ . Different shapes for data points indicate different substrates for the experiments. The points marked with numbers are the ones for which further analysis is done in this chapter. The insets are snapshots of the colloidal systems associated with the chosen data points. The blue plot is data from Marcus et al. [93] **Bottom:** Symmetry fractions vs.  $\phi$ .

## A.0.1 The examples

Point 1 ( $\phi = 0.03$ )

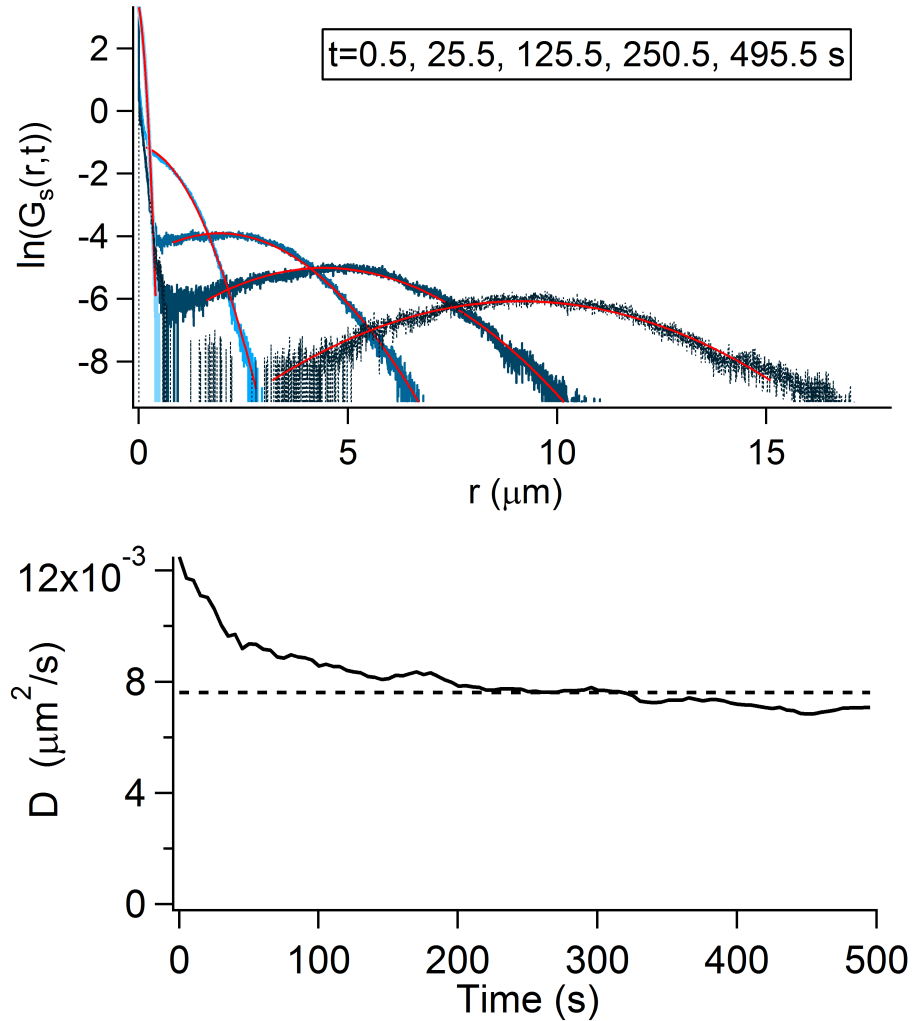


Figure A.2: **Top:** Examples of the quadratic fit to the  $\ln(G_s(r,t))$ . Quadratic fit seems to work from the beginning to the end, i.e.  $t = 0.5$  s to  $t = 495.5$  s. The initial peak in the  $\ln(G_s(r,t))$ , (particularly visible in the later times) is due to stuck particles, and therefore the low  $r$  values are excluded in the fit. This peak is removed in subsequent Figures when applicable. Also the  $\ln(G_s(r,t))$  is not peaked at zero due to the drift present in the system. The  $G_s(r,t)$  is Gaussian from  $t = 0.5$  s to  $t = 495.5$  s. **Bottom:** Diffusion coefficient values ( $D$ ) obtained from the quadratic fit to the  $\ln(G_s(r,t))$ , as a function of time. The dashed line is the  $D$  value obtained from MSD vs.  $t$ .

Point 2 ( $\phi = 0.04$ )

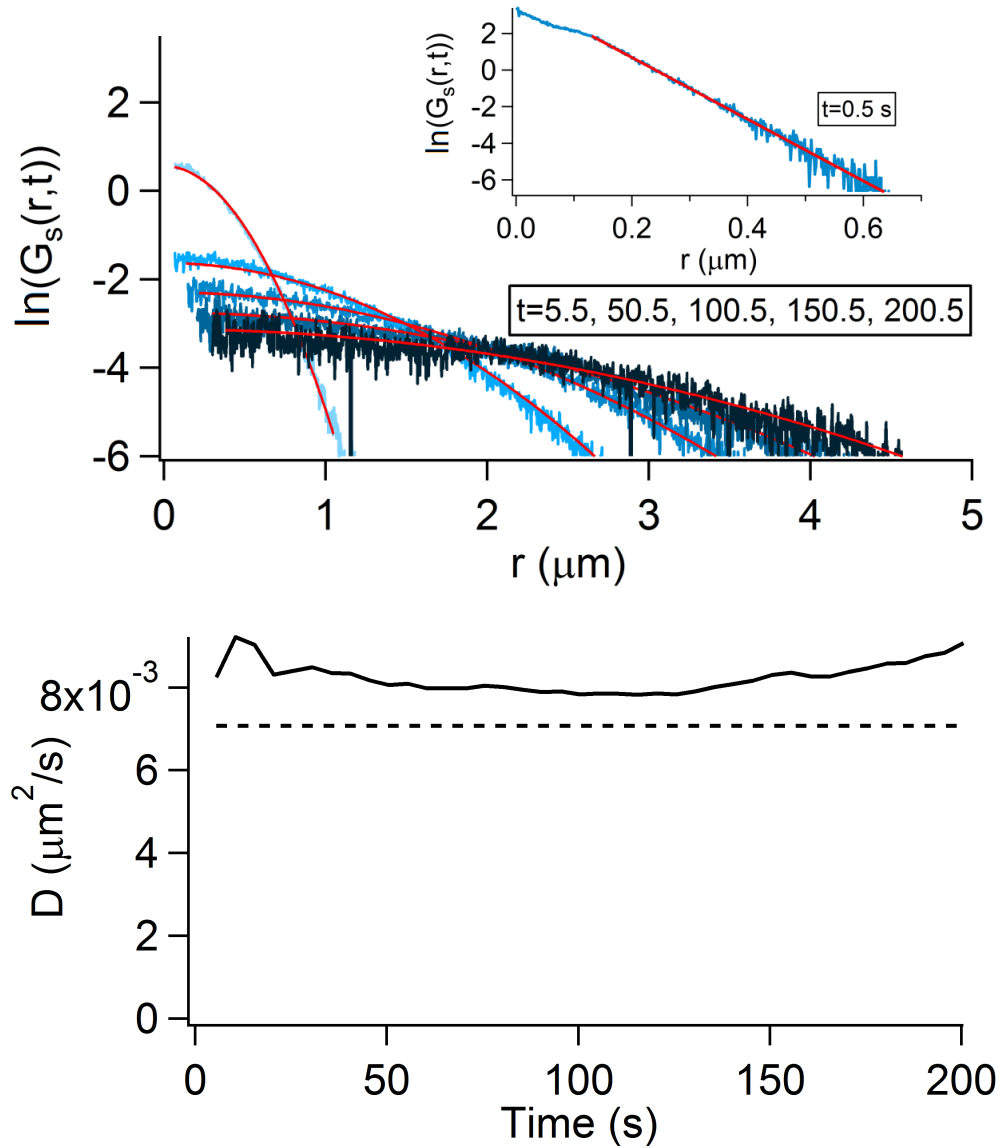


Figure A.3: **Top:** Examples of the fits to the  $\ln(G_s(r,t))$ .  $\ln(G_s(r,t))$  has a linear tail at  $t = 0.5$  s, which according to the literature is a sign of dynamical heterogeneity. Quadratic fit works for the rest, i.e.  $t = 5.5$  s to  $t = 200.5$  s. **Bottom:** Diffusion coefficient values ( $D$ ) obtained from the quadratic fit to the  $\ln(G_s(r,t))$ , as a function of time. The dashed line is the  $D$  value obtained from MSD vs.  $t$ .

Point 3 ( $\phi = 0.20$ )

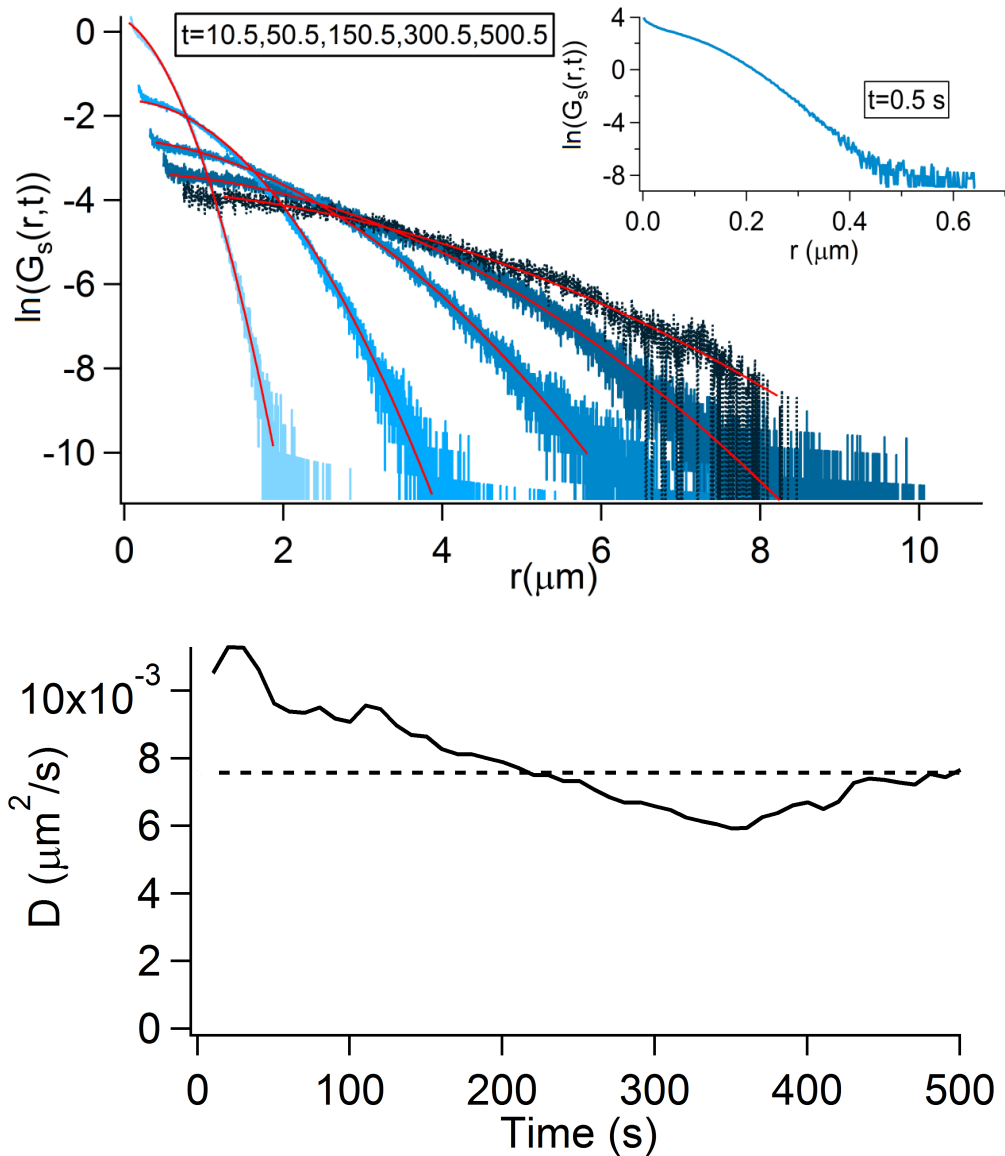


Figure A.4: **Top:** Examples of the quadratic fit to the  $\ln(G_s(r,t))$ . Quadratic fit works for  $t = 10.5$  s to  $t = 500.5$  s. The  $\ln(G_s(r,t))$  for  $t = 0.5$  s has a linear tail, which according to the literature is a sign of dynamical heterogeneity. **Bottom:** Diffusion coefficient values ( $D$ ) obtained from the quadratic fit to the  $\ln(G_s(r,t))$ , as a function of time. The dashed line is the  $D$  value obtained from MSD vs.  $t$ .

Point 4 ( $\phi = 0.40$ )

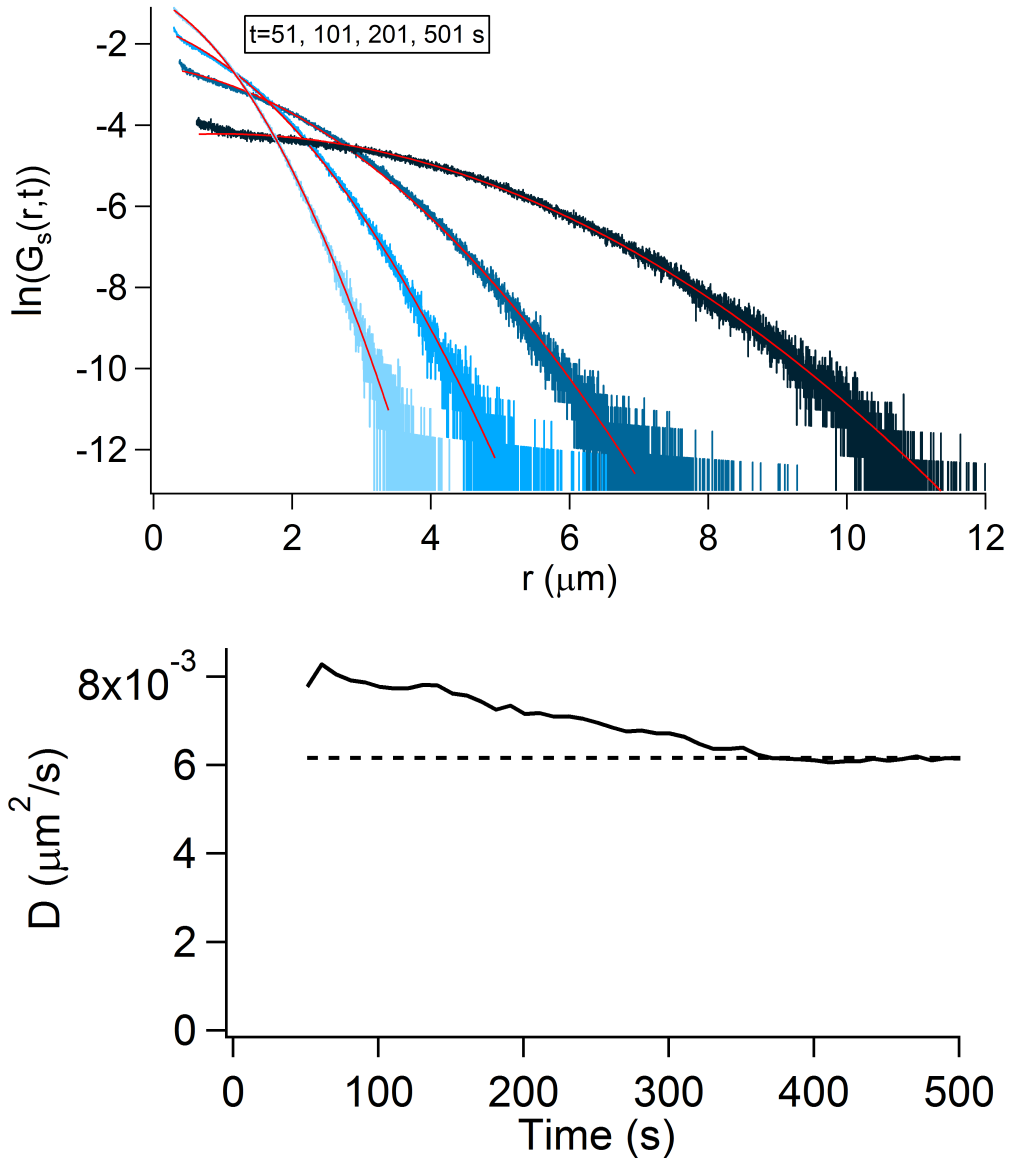


Figure A.5: **Top:** Examples of the quadratic fit to the  $\ln(G_s(r,t))$ . Quadratic fit works from  $t = 51$  s to  $t = 501$  s. At  $t = 1$  s the Behavior is ambiguous (neither Gaussian, nor exponential). Also, it has a linear tail from  $t = 11$  s to  $t = 41$  s.  $t = 51$  s seems to be the onset of quadratic behavior for  $\ln(G_s(r,t))$ . **Bottom:** Diffusion coefficient values ( $D$ ) obtained from the quadratic fit to the  $\ln(G_s(r,t))$ , as a function of time. The dashed line is the  $D$  value obtained from MSD vs.  $t$ .

Point 5 ( $\phi = 0.49$ )

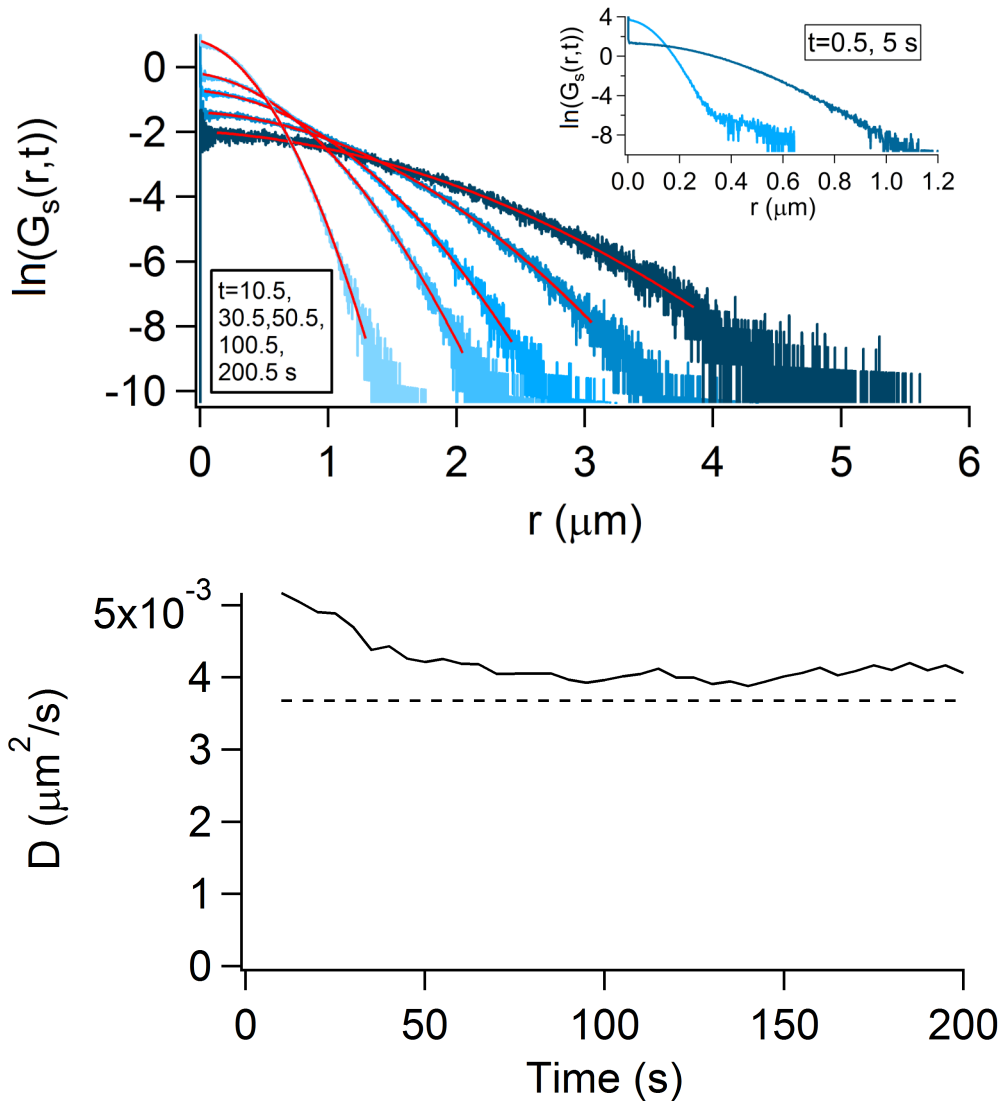


Figure A.6: **Top:**  $\ln(G_s(r,t))$  does not seem quadratic for  $t = 0.5$  s. The quadratic fit works well from  $t = 10$  s to  $t = 200$  s. **Bottom:** Diffusion coefficient values ( $D$ ) obtained from the quadratic fit to the  $\ln(G_s(r,t))$ , as a function of time. The dashed line is the  $D$  value obtained from MSD vs.  $t$ .

Point 6 ( $\phi = 0.57$ )

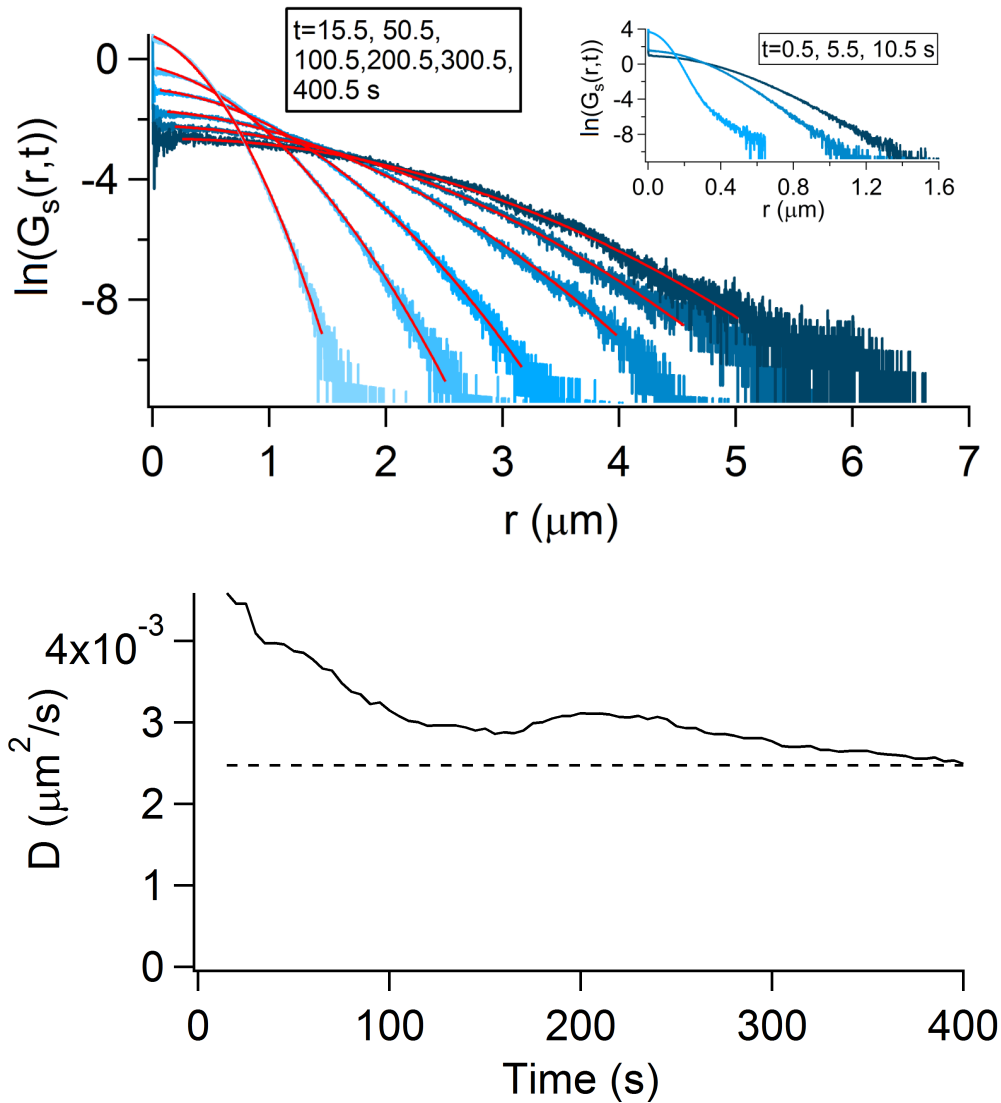


Figure A.7: **Top:**  $\ln(G_s(r,t))$  does not seem quadratic for  $t = 0.5$  s. The quadratic fit works well from  $t = 10$  s to  $t = 400$  s. **Bottom:** Diffusion coefficient values ( $D$ ) obtained from the quadratic fit to the  $\ln(G_s(r,t))$ , as a function of time. The dashed line is the  $D$  value obtained from MSD vs.  $t$ .

Point 7 ( $\phi = 0.64$ )

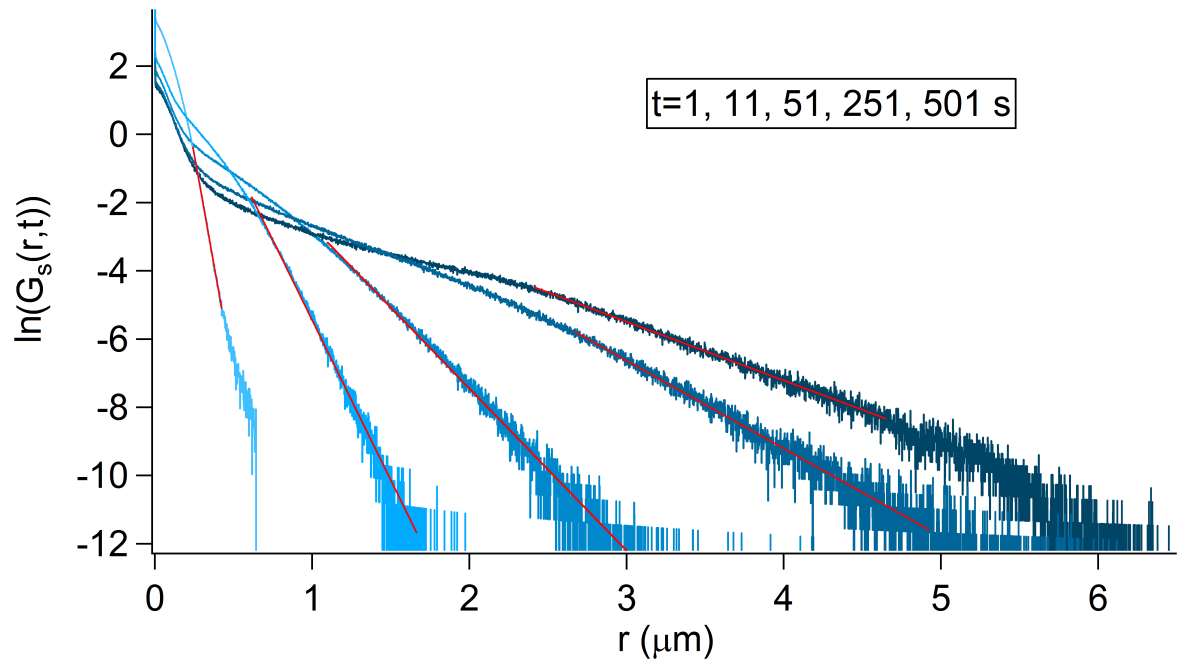


Figure A.8: The  $\ln(G_s(r,t))$  has a linear tail for  $t = 1$  s to  $t = 501$  s.

Point 8 ( $\phi = 0.78$ )

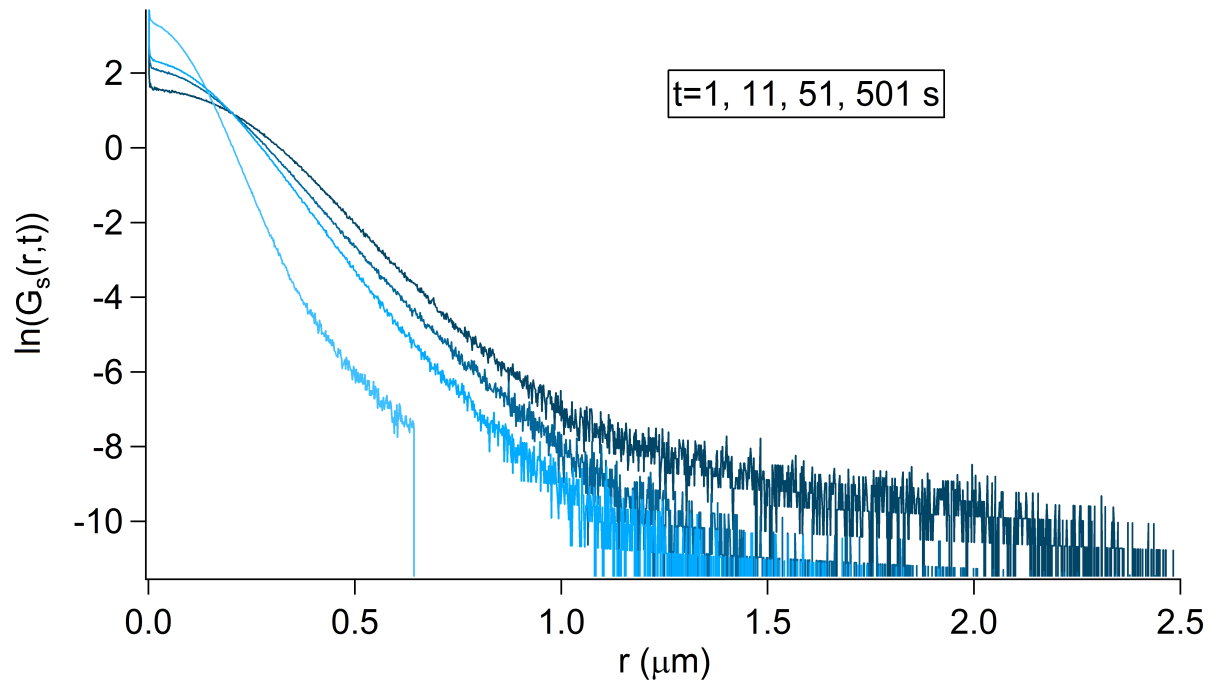


Figure A.9: The  $\ln(G_s(r,t))$  (for all times) show the exponential behavior at short distances, but deviate from it at longer distances.

## A.0.2 Discussion on the initial peak of the $G_s(r, t)$

Figures A.10 and A.11 are related to the **point 1** in the appendix.

As is seen in Figure A.10, less than 10% of the particles are stuck. In Figure A.11(Top) the initial peak (presumably due to stuck particles) is up to  $r \sim 0.5 \mu m$ . In Figure A.11(Bottom) the integral reaches to around 0.06 which is 6% of the total integral (i.e. 1). This means that the ratio integral under the initial peak to the whole integral is consistent with the fraction of stuck particles.

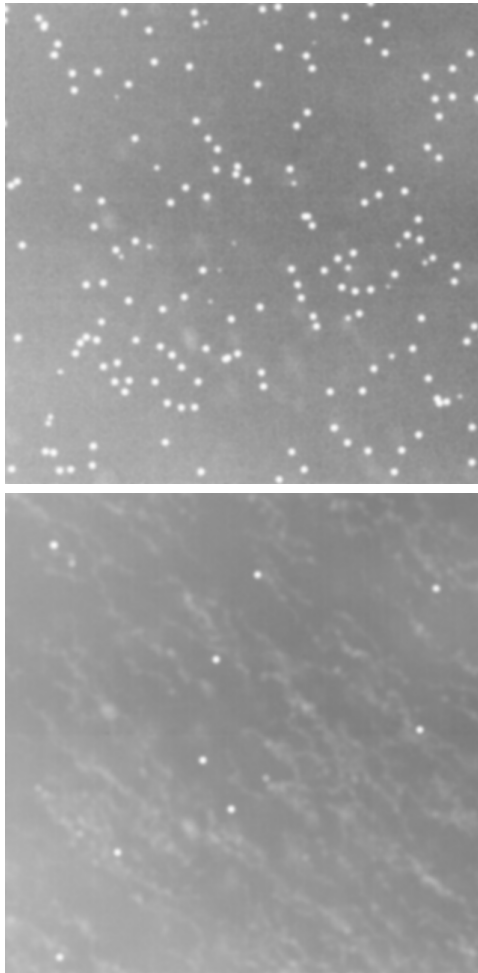


Figure A.10: A typical frame and the z-project of the movie. less than 10% of the particles are stuck.

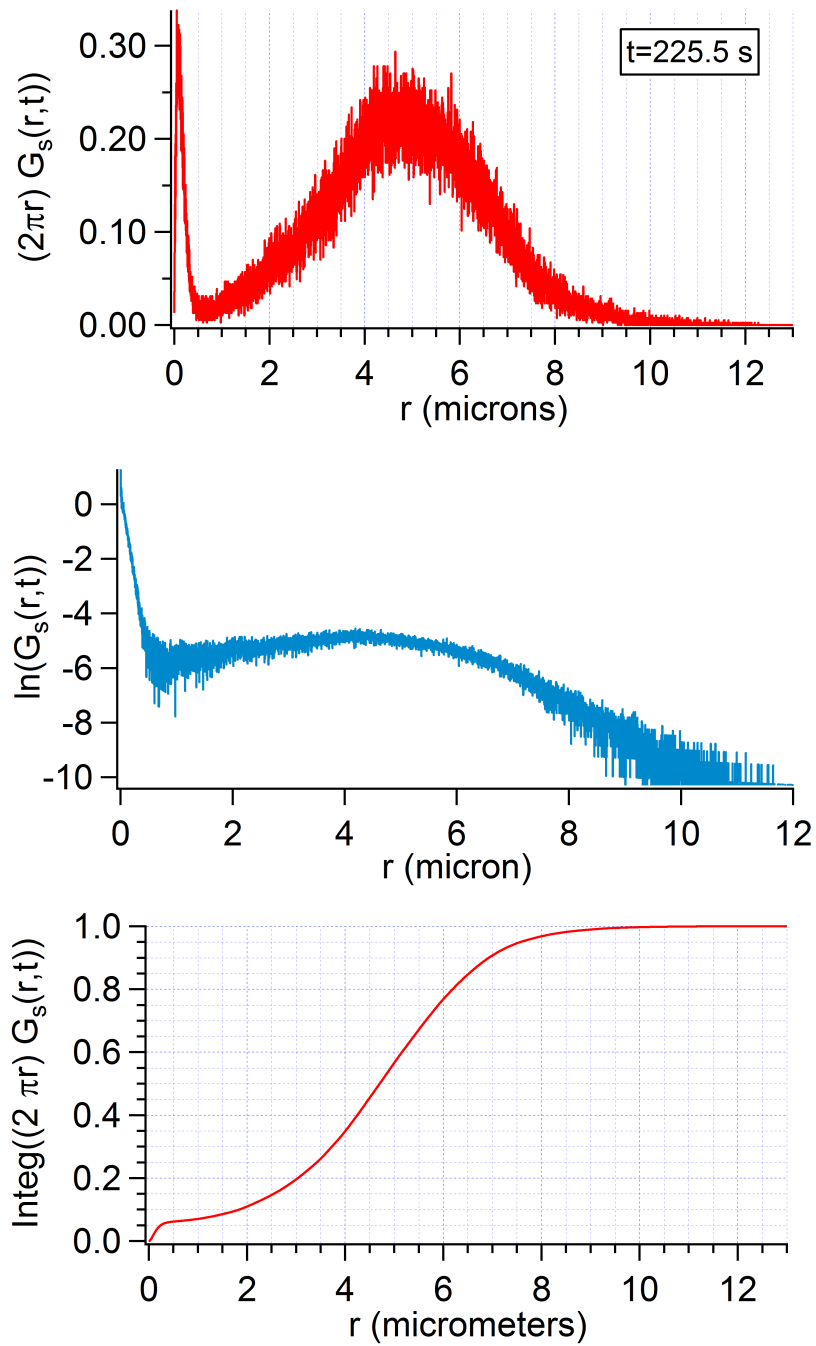


Figure A.11: (Top)  $(2\pi r)G_s(r, t)$  for  $t = 225.5$  s of point 1 in the appendix. (Middle) The  $\ln(G_s(r, t))$ . (Bottom) The area under the  $(2\pi r)G_s(r, t)$  as a function of  $r$ .

Figures A.12 and A.13 are related to the **point 3** in the appendix.

As is seen in Figure A.12, around 10% of the particles are stuck. In Figure A.13(Top) the initial peak is up to  $r \sim 0.6 \mu m$ . In Figure A.13(Bottom) the integral reaches to around 0.08 which is 8% of the total integral (i.e. 1). This means that the ratio integral under the initial peak to the whole integral is consistent with the fraction of stuck particles.

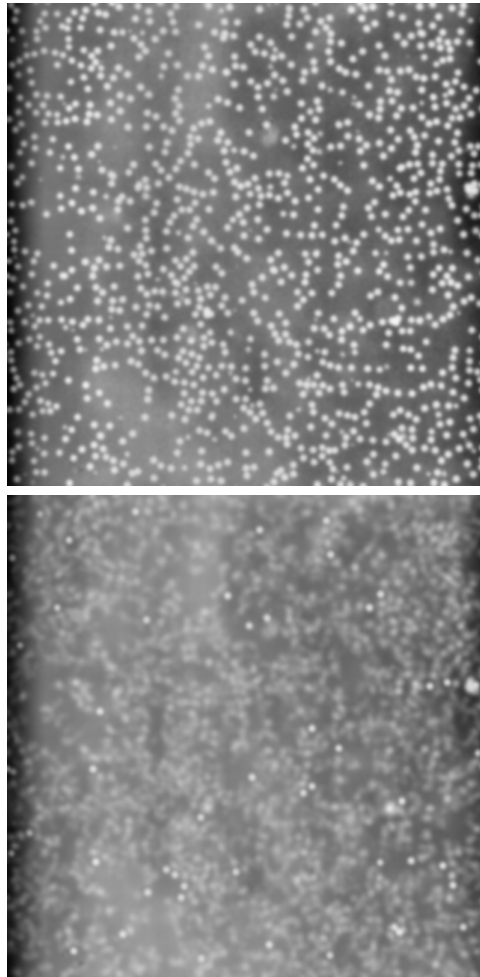


Figure A.12: A typical frame and the z-project of the movie. less than 10% of the particles are stuck.

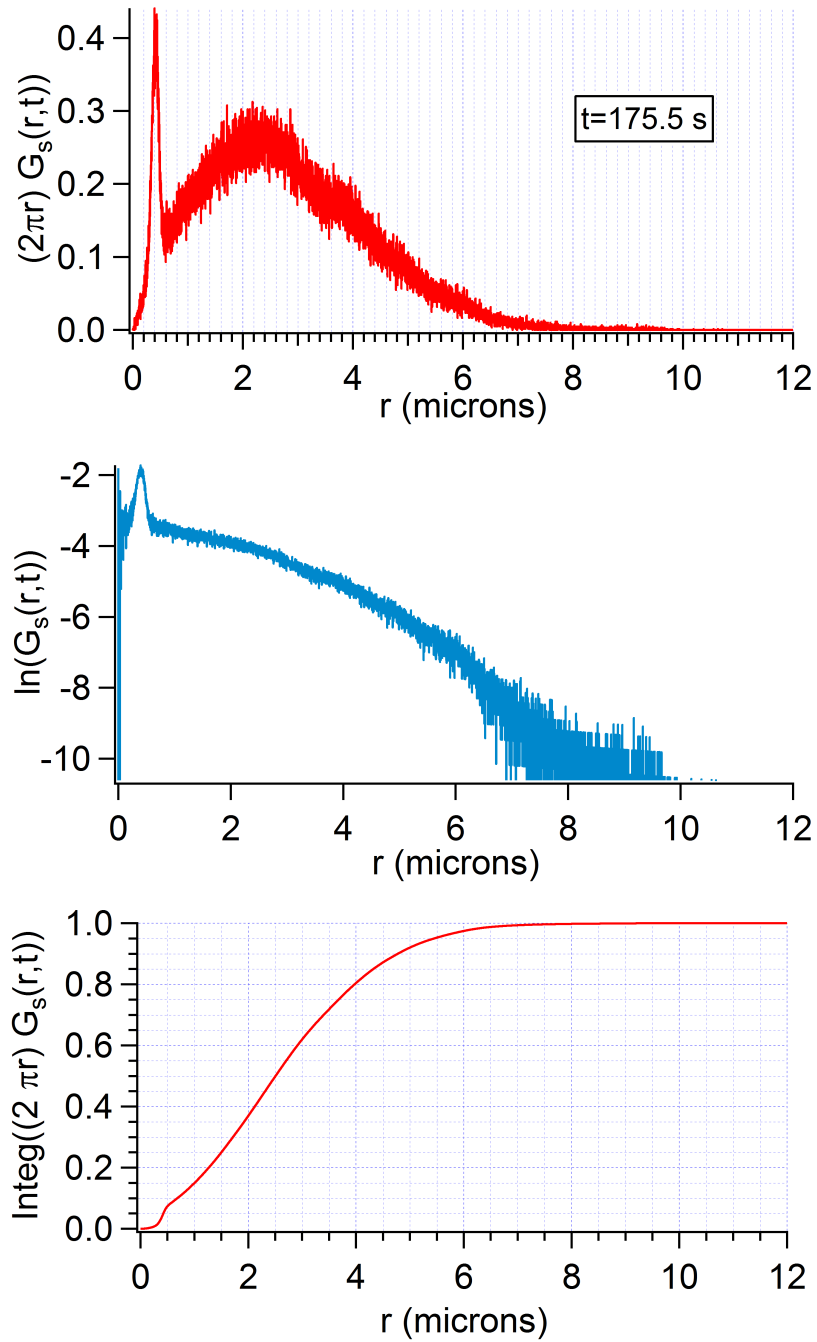


Figure A.13: (Top)  $(2\pi r)G_s(r, t)$  for  $t = 175.5$  s of point 3 in the appendix. (Middle) The  $\ln(G_s(r, t))$ . (Bottom) The area under the  $(2\pi r)G_s(r, t)$  as a function of  $r$ .

# Bibliography

- [1] J.W. Goodwin. *Colloids and Interfaces with Surfactants and Polymers*. John Wiley and Sons, 2004.
- [2] P. Jiang and M. J. McFarland. Large-scale fabrication of wafer-size colloidal crystals, macroporous polymers and nanocomposites by spin-coating. *J. Am. Chem. Soc.*, 126:13778–13786, 2004.
- [3] C. Arcos, K. Kumar, W. González-Viñas, R. Sirera, K. M. Poduska, and A. Yethiraj. Orientationally correlated colloidal polycrystals without long-range positional order. *Phys. Rev. E*, 77:050402(R), 2008.
- [4] A. Mihi, M. Ocaña, and H. Míguez. Oriented colloidal-crystal thin films by spin-coating microspheres dispersed in volatile media. *Adv. Mater.*, 18:2244–2249, 2006.
- [5] P. N. Pusey and W. van Megen. Phase behaviour of concentrated suspensions of nearly hard colloidal spheres. *Nature*, 320:340–342, 1986.
- [6] M. D. Haw. Colloidal suspensions, Brownian motion, molecular reality: A short history. *J. Phys. Cond. Mat.*, 14, 2002.
- [7] A. Yethiraj. Tunable colloids: Control of colloidal phase transitions with tunable interactions. *Soft Matter*, 3, 2007.

- [8] Q. Chen, S. C. Bae, and S. Granick. Directed self-assembly of a colloidal Kagome lattice. *Nature*, 469, 2011.
- [9] S. H. Kim, S. Y. Lee, S. M. Yang, and Gi-Ra Yi. Self-assembled colloidal structures for photonics. *NPG Asia Mater.*, 3, 2011.
- [10] G. A. Ozin and S. M. Yang. The race for the photonic chip: Colloidal crystal assembly in silicon wafers. *Adv. Funct. Mater.*, 11, 2, 2011.
- [11] Í. Í. Tarhan and G. H. Watson. Photonic band structure of fcc colloidal crystals. *Phys. Rev. Lett.*, 76, 2, 1996.
- [12] P. Bhattacharya. *Quantum Well and Quantum Dot Lasers: From Strained Layer and Self-Organized Epitaxy to High-Performance Devices*. Kluwer, 2000.
- [13] P. Bhattacharya, A. D. Stiff-Roberts, S. Krishna, and S. Kennerly. Quantum dot infrared detectors and sources. *Int. J. High Speed Elec. Syst.*, 12, 2002.
- [14] M. Harun-Ur-Rashid, A. Bin Imran, T. Seki, M. Ishii, H. Nakamura, and Y. Takeoka. Angle-independent structural color in colloidal amorphous arrays. *Chemphyschem*, 11, 2010.
- [15] Y. Takeoka, S. Yoshioka, A. Takano, S. Arai, N. Khanin, H. Nishihara, M. Teshima, Y. Ohtsuka, and T. Seki. Production of colored pigments with amorphous arrays of black and white colloidal particles. *Angew. Chem. Int. Edit.*, 52, 2013.
- [16] C. Paquet, M. Allard, G. Gledel, and E. Kumacheva. Guest-host colloid crystals: Experimental study and simulations. *J. Phys. Chem. B*, 110, 2006.
- [17] D. M. Kuncicky, B. G. Prevo, and O. D. Velev. Controlled assembly of SERS substrates templated by colloidal crystal films. *J. Mater. Chem.*, 16, 2006.

- [18] C. J. Lawrence. The mechanics of spin coating of polymer films. *Phys. Fluids*, 31:2786, 1988.
- [19] M. Pichumani, P. Bagheri, W. González-Viñas, K. M. Poduska, and A. Yethiraj. Dynamics, crystallization and structures in colloid spincoating. *Soft Matter*, 9:3220–3229, 2013.
- [20] A. G. Emslie, F. T. Bonner, and L. G. Peck. Flow of a viscous liquid on a rotating disk. *J. Appl. Phys.*, 29, 1958.
- [21] D. Meyerhofer. Characteristics of resist films produced by spinning. *J. Appl. Phys.*, 49:3993, 1978.
- [22] T. J. Rehg and B. G. Higgins. Spin coating of colloidal suspension. *AIChE J.*, 34, 4:489–501, 1992.
- [23] M. Giuliani, W. González-Viñas, K. M. Poduska, and A. Yethiraj. Dynamics of crystal structure formation in spin-coated colloidal films. *J Phys. Chem. Lett.*, 1, 2010.
- [24] J. Bergenholtz, J. F. Brady, and M. Vucic. The non-Newtonian rheology of dilute colloidal suspensions. *J Fluid Mech.*, 465, 2002.
- [25] A. J. Wang, S. L. Chen, P. Dong, C. T. Hu, and L. Sang. Fabrication of large-area and high-quality colloidal crystal films on nanocrystalline porous substrates by a room temperature floating self-assembly method. *Thin Solid Films*, 519:1798–1802, 2011.
- [26] Y.W. Chung, I.C. Leu, J.H. Lee, and M.H. Hon. Fabrication of high-quality colloidal crystals by a capillary-enhanced method. *Appl. Phys. A*, 79:2089–2092, 2004.

- [27] S. L. Kuai, X. F. Hu, A. Hachea, and V. V. Truong. High-quality colloidal photonic crystals obtained by optimizing growth parameters in a vertical deposition technique. *J. Cryst. Growth*, 267:317–324, 2004.
- [28] J. Zhang, H. Liu, Z. Wang, and N. Ming. Assembly of high-quality colloidal crystals under negative pressure. *J. Appl. Phys.*, 103:013517, 2008.
- [29] S. Portal-Marco, M. À. Vallvé, O. Arteaga, J. Ignés-Mullol, C. Corbella, and E. Bertra. Structure and physical properties of colloidal crystals made of silica particles. *Colloids Surf., A*, 401:38–47, 2012.
- [30] A. J. Krejci, C. G. W. Thomas, and J. H. Dickerson. Statistical assessment of order within systems of nanoparticles: Determining the efficacy of patterned substrates to facilitate ordering within nanoparticle monolayers fabricated through electrophoretic deposition. *Phys. Rev. E*, 87:042307, 2013.
- [31] P. Bagheri, A. M. Al mudallal, A. Yethiraj, and K. M. Poduska. Quantitative metrics for assessing positional and orientational order in colloidal crystals. *Langmuir*, 31(30):8251–8259, 2015.
- [32] J. M. Kosterlitz and D. J. Thouless. Ordering, metastability and phase transitions in two-dimensional systems. *J. Phys. C*, 6:1181–1203, 1973.
- [33] B. I. Halperin and D. R. Nelson. Theory of two-dimensional melting. *Phys. Rev. Lett.*, 41, 2:121–124, 1978.
- [34] F. F. Abraham. The phases of two-dimensional matter, their transitions, and solid-state stability: A perspective via computer simulation of simple atomic systems. *Phys. Rep.*, 80, 5:340–374, 1981.

- [35] A. H. Marcus and S. A. Rice. Phase transitions in a confined quasi-two-dimensional colloid suspension. *Phys. Rev. E*, 55:637–656, 1997.
- [36] C. H. Chang, L. Tian, W. R. Hesse, H. Gao, H. J. Choi, J.G. Kim, M. Siddiqui, and G. Barbastathis. From two-dimensional colloidal self-assembly to three-dimensional nanolithography. *Nano Lett.*, 11, 2011.
- [37] X. Ye and L. Qi. Two-dimensionally patterned nanostructures based on monolayer colloidal crystals: Controllable fabrication, assembly, and applications. *Nano Today*, 6:608–631, 2011.
- [38] Y. H. Ye, F. LeBlanc, A. Haché, and V. V. Truong. Self-assembling three-dimensional colloidal photonic crystal structure with high crystalline quality. *Appl. Phys. Lett.*, 78:52–53, 2001.
- [39] L. T. Shereda, R. G. Larson, and M. J. Solomon. Local stress control of spatiotemporal ordering of colloidal crystals in complex flows. *Phys. Rev. Lett.*, 101, 2008.
- [40] B. J. Ackerson and P. N. Pusey. Shear-induced order in suspensions of hard spheres. *Phys. Rev. Lett.*, 61, 8, 1988.
- [41] E. Vermolen. *Manipulation of colloidal crystallization*. Utrecht University, 2008.
- [42] S. Pronk and D. Frenkel. Large effect of polydispersity on defect concentrations in colloidal crystals. *J. Chem. Phys.*, 120, 2004.
- [43] R. Verberg, I. M. de Schepper, and E. G. D. Cohen. Viscosity of colloidal suspensions. *arXiv:chao-dyn/9606008*, 1996.
- [44] A. Acrivos, M. J. Shah, and E. E. Petersen. On the flow of a non-Newtonian liquid on a rotating disk. *J. Appl. Phys.*, 31, 6, 1960.

- [45] N. D. Denkov, O. D. Velev, P. A. Kralchevsky, I. B. Ivanov, H. Yoshimura, and K. Nagayama. Mechanism of formation of two-dimensional crystals from latex particles on substrates. *Langmuir*, 8, 1992.
- [46] P. Jiang, J. F. Bertone, K. S. Hwang, and V. L. Colvin. Single-crystal colloidal multilayers of controlled thickness. *Chem. Mater.*, 11:2132–2140, 1999.
- [47] S. Wong, V. Kitaev, and G. A. Ozin. Colloidal crystal films: Advances in universality and perfection. *J. Am. Chem. Soc.*, 125:15589–15598, 2003.
- [48] S. H. Park, D. Qin, and Y. Xia. Crystallization of mesoscale particles over large areas. *Adv. Mater.*, 10, No. 13:1028–1032, 1998.
- [49] J. D. Joannopoulos, S. G. Johnson, J. N. Winn, and R. D. Meade. *Photonic Crystals, Molding the Flow of Light*. Princeton University Press, 2008.
- [50] J. H. J. Thijssen, A. V. Petukhov, D. C. 't Hart, A. Imhof, C. H. M. van der Werf, R. E. I. Schropp, and A. van Blaaderen. Characterization of photonic colloidal single crystals by microradian X-ray diffraction. *Adv. Mater.*, 18:1662–1666, 2006.
- [51] P. Huber, O. Bunk, U. Pietsch, M. Textor, and T. Geue. Grazing incidence small angle X-ray scattering on colloidal crystals. *J. Phys. Chem.*, 114:12473–12479, 2010.
- [52] U. Gasser. Crystallization in three- and two-dimensional colloidal suspensions. *J. Phys. Cond. Mat.*, 21:203101–203124, 2009.
- [53] A. P. Bartlett, M. Pichumani, M. Giuliani, W. González-Viñas, and A. Yethiraj. Modified spin-coating technique to achieve directional colloidal crystallization. *Langmuir*, 28:3067–3070, 2012.

- [54] S. Nöjd, P. S. Mohanty, P. Bagheri, A. Yethiraj, and P. Schurtenberger. Electric field driven self-assembly of ionic microgels. *Soft Matter*, 9:9199–9207, 2013.
- [55] A. M. Almudallal, S. V. Buldyrev, and I. Saika-Voivod. Inverse melting in a two-dimensional off-lattice model. *J. Chem. Phys.*, 140:144505, 2014.
- [56] V. E. Ferry, M. A. Verschuuren, M. C. van Lare, R. E. I. Schropp, H. A. Atwater, and A. Polman. Optimized spatial correlations for broadband light trapping nanopatterns in high efficiency ultrathin film a-Si:H solar cells. *Nano Lett.*, 11:4239–4245, 2011.
- [57] H. Cong and W. Cao. Colloidal crystallization induced by capillary force. *Langmuir*, 19:8177–8181, 2003.
- [58] L. Wang and X. S. Zhao. Fabrication of crack-free colloidal crystals using a modified vertical deposition method. *J. Phys. Chem. C*, 111:8538–8542, 2007.
- [59] Z. Z. Gu, A. Fujishima, and O. Sato. Fabrication of high-quality opal films with controllable thickness. *Chem. Mater.*, 14:760–765, 2002.
- [60] L. K. Teh, N. K. Tan, C. C. Wong, and S. Li. Growth imperfections in three-dimensional colloidal self-assembly. *Appl. Phys. A*, 81, 2005.
- [61] M. H. Kim, S. H. Im, and O O. Park. Rapid fabrication of two- and three-dimensional colloidal crystal films via confined convective assembly. *Adv. Funct. Mater.*, 15:1329–1335, 2005.
- [62] C. Zhou, J. Han, and R. Guo. A facile strategy to colloidal crystals by drying condensed suspension droplets. *J. Colloid Interface Sci.*, 397:80–87, 2013.

- [63] N. V. Dziomkina, M. A. Hempenius, and G. J. Vancso. Towards true 3-dimensional bcc colloidal crystals with controlled lattice orientation. *Polymer*, 50:5713–5719, 2009.
- [64] W. M. Choi. Simple and rapid fabrication of large-area 2D colloidal crystals for nanopatterning of conducting polymers. *Microelectron. Eng.*, 110:1–5, 2013.
- [65] A. Coll, S. Bermejo, D. Hernández, and L. Castañer. Colloidal crystals by electro spraying polystyrene nanofluids. *Nanoscale Res. Lett.*, 8:26, 2013.
- [66] Z. Lu and M. Zhou. Fabrication of large scale two-dimensional colloidal crystal of polystyrene particles by an interfacial self-ordering process. *J. Colloid Interf. Sci.*, 361:429–435, 2011.
- [67] A. J. Wang, S. L. Chen, P. Dong, Q. Zhou, G. M. Yuan, and G. C. Su. Self-assembling of colloidal particles dispersed in mixture of ethanol and water at the air-liquid interface of colloidal suspension at room temperature. *Chin. Phys. Lett.*, 26, No. 8:086104, 2009.
- [68] X. Wang, S. M. Husson, X. Qian, and S. R. Wickramasinghe. Vertical cell assembly of colloidal crystal films with controllable thickness. *Mater. Lett.*, 63:1981–1983, 2009.
- [69] D. Nagao, R. Kameyama, H. Matsumoto, Y. Kobayashi, and M. Konno. Single- and multi-layered patterns of polystyrene and silica particles assembled with a simple dip-coating. *Colloids Surf., A*, 317:722–729, 2008.
- [70] Y. Fu, Z. Jin, Z. Liu, Y. Liu, and W. Li. Self-assembly of colloidal crystals from polystyrene emulsion at elevated temperature by dip-drawing method. *Mater. Lett.*, 62:4286–4289, 2008.

- [71] P. Jiang, T. Prasad, M. J. McFarland, and V. L. Colvin. Two-dimensional nonclose-packed colloidal crystals formed by spincoating. *Appl. Phys. Lett.*, 89:011908, 2006.
- [72] Q. Li, Y. Chen, and P. Dong. Improvement of the quality of silica colloidal crystals by controlling drying. *Mater. Lett.*, 59:3521–3524, 2005.
- [73] J. C. Crocker and D. G. Grier. Methods of digital video microscopy for colloidal studies. *J. Colloid Interf. Sci.*, 179:298–310, 1996.
- [74] F.A. Lindemann. The calculation of molecular vibration frequencies. *Phys. Z.*, 11:609–612, 1910.
- [75] F. D. Stacey and R. D. Irvine. Theory of melting: Thermodynamic basis of Lindemann’s law. *Aust. J. Phys.*, 30:631, 1977.
- [76] C. A. Murray. *Bond-Orientational Order in Condensed Matter Systems*. Springer, 1991.
- [77] A. Yethiraj, A. Wouterse, B. Groh, and A. van Blaaderen. Nature of an electric-field-induced colloidal martensitic transition. *Phys. Rev. Lett.*, 92(5):058301(4), 2004.
- [78] W. Mickel, S. C. Kapfer, G. E. Schröder-Turk, and K. Mecke. Shortcomings of the bond orientational order parameters for the analysis of disordered particulate matter. *J. Chem. Phys.*, 138:044501, 2013.
- [79] C. A. Murray and D. H. Van Winkle. Experimental observation of two-stage melting in a classical two-dimensional screened coulomb system. *Phys. Rev. Lett.*, 58(12):1200–1203, 1987.

- [80] K. J. Strandburg. Two-dimensional melting. *Rev. Mod. Phys.*, 60(1):161–207, 1988.
- [81] R. A. Quinn, C. Cui, J. Goree, and J. B. Pieper. Structural analysis of a coulomb lattice in a dusty plasma. *Phys. Rev. E*, 53, 3:R2049–R2052, 1996.
- [82] W. Qi, A. P. Gantapara, and M. Dijkstra. Two-stage melting induced by dislocations and grain boundaries in monolayers of hard spheres. *Soft Matter*, 10:5449–5457, 2014.
- [83] C. A. Knapek. *Phase Transitions in Two-Dimensional Complex Plasmas*. Springer, 2011.
- [84] Y. Cheng, P. G. Jönsson, and Z. Zhao. Controllable fabrication of large-area 2D colloidal crystal masks with large size defect-free domains based on statistical experimental design. *Appl. Surf. Sci.*, 313:144–151, 2014.
- [85] D. T. Lee and B. J. Schachter. Two algorithms for constructing a Delaunay triangulation. *International Journal of Computer & Information Science*, 9(3):219–242, 1980.
- [86] J. A. Weiss, D. W. Oxtoby, D. G. Grier, and C. A. Murray. Martensitic transition in a confined colloidal suspension. *J. Chem. Phys.*, 103:1180, 1995.
- [87] Q. Yan, Z. Zhou, and X. S. Zhao. Inward-growing self-assembly of colloidal crystal films on horizontal substrates. *Langmuir*, 21:3158, 2005.
- [88] A. Emoto and T. Fukuda. Tailored assembly of colloidal particles: Alternative fabrication of photonic crystal or photonic glass. *Appl. Phys. Lett.*, 100:131901, 2012.

- [89] A. Einstein. Über die von der molekularkinetischen theorie der wärme geforderte bewegung von in ruhenden flüssigkeiten suspendierten teilchen. *Ann. Phys.*, 322 (8):549–560, 1905.
- [90] J. Dhont. *An Introduction to Dynamics of Colloids*. Elsevier Science, 1996.
- [91] S. Herrera-Velarde and R. Castañeda-Priego. Diffusion in two-dimensional colloidal systems on periodic substrates. *Phys. Rev. E*, 79:041407, 2009.
- [92] K. J. Wilkinson and J. R. Lead, editors. *Environmental Colloids and Particles: Behaviour, Separation and Characterisation*. Wiley, 2007.
- [93] A. H. Marcus, J. Schofield, and S. A. Rice. Experimental observations of non-Gaussian behavior and stringlike cooperative dynamics in concentrated quasi-two-dimensional colloidal liquids. *Phys. Rev. E*, 60,5:5725–5736, 1999.
- [94] C. R. Berardi, K. Barros, J. F. Douglas, and W. Losert. Direct observation of stringlike collective motion in a two-dimensional driven granular fluid. *Phys. Rev. E*, 81:041301, 2010.
- [95] R. Zangi and S. A. Rice. Cooperative dynamics in two dimensions. *Phys. Rev. Lett.*, 92, 3:035502, 2004.
- [96] B. Cui, B. Lin, and S. A. Rice. Dynamical heterogeneity in a dense quasi-two-dimensional colloidal liquid. *J. Chem. Phys.*, 114:9142–9155, 2001.
- [97] J. Schofield, A. H. Marcus, and S. A. Rice. Dynamics of quasi two-dimensional colloidal systems. *J. Phys. Chem.*, 100:18950–18961, 1996.
- [98] A. H. Marcus, B. Lin, and S. A. Rice. Self-diffusion in dilute quasi-two-dimensional hard sphere suspensions: Evanescent wave light scattering and video microscopy studies. *Phys. Rev. E*, 53,2:1765–1776, 1996.

- [99] E. R. Weeks, J. C. Crocker, A. C. Levitt, A. Schofield, and D. A. Weitz. Three-dimensional direct imaging of structural relaxation near the colloidal glass transition. *Science*, 287:627–631, 2000.
- [100] H. König, R. Hund, K. Zahn, and G. Maret. Experimental realization of a model glass former in 2d. *Eur. Phys. J. E*, 18:287–293, 2005.
- [101] T. Narumi, S. V. Franklin, K. W. Desmond, M. Tokuyama, and E. R. Weeks. Spatial and temporal dynamical heterogeneities approaching the binary colloidal glass transition. *Soft Matter*, 7:1472–1482, 2011.
- [102] S. Gokhale, K. H. Nagamanasa, R. Ganapathy, and A. K. Sood. Growing dynamical facilitation on approaching the random pinning colloidal glass transition. *Nat. Commun.*, 5, 2014.
- [103] C. Bechinger, M. Brunner, and P. Leiderer. Phase behavior of two-dimensional colloidal systems in the presence of periodic light fields. *Phys. Rev. Lett.*, 86:930, 2001.
- [104] L. Zaidouny. *Phase Behavior of Colloidal Monolayers on One-Dimensional Periodic and Quasiperiodic Light Fields*. PhD thesis, Universität Stuttgart, 2015.
- [105] G. Nägele. *The Physics of Colloidal Soft Matter*. Institute of Fundamental Technological Research, 2004.
- [106] P. Hopkins, A. Fortini, A. J. Archer, and M. Schmidt. The van Hove distribution function for Brownian hard spheres: Dynamical test particle theory and computer simulations for bulk dynamics. *J. Chem. Phys.*, 133:224505, 2010.

- [107] P. Chaudhuri, L. Berthier, and W. Kob. Universal nature of particle displacements close to glass and jamming transitions. *Phys. Rev. Lett.*, 99:060604, 2007.
- [108] G. Szamel and E. Flenner. Time scale for the onset of Fickian diffusion in supercooled liquids. *Phys. Rev. E*, 73:011504, 2006.
- [109] D. A. Stariolo and G. Fabricius. Fickian crossover and length scales from two point functions in supercooled liquids. *J. Chem. Phys.*, 125:064505, 2006.
- [110] J. C. Crocker and E. R. Weeks. Particle tracking using idl. <http://www.physics.emory.edu/faculty/weeks//idl/tracking.html>, March 2015.
- [111] A. Kasper, E. Bartsch, and H. Sillescu. Self-diffusion in concentrated colloid suspensions studied by digital video microscopy of core-shell tracer particles. *Langmuir*, 14:5004–5010, 1998.
- [112] O. Marnette, E. Perez, F. Pincet, and G. Bryant. Two-dimensional crystallization of hard sphere particles at a liquid-liquid interface. *Colloids Surf., A*, 346:208–212, 2009.
- [113] K. Binder, S. Sengupta, and P. Nielaba. The liquid-solid transition of hard discs: First-order transition or Kosterlitz-Thouless-Halperin-Nelson-Young scenario? *J. Phys. Condens. Matter*, 14:2323–2333, 2002.